PHOTON STATISTICS IN SCINTILLATION CRYSTALS

by

Vaibhav Joga Singh Bora

A Dissertation Submitted to the Faculty of the

COLLEGE OF OPTICAL SCIENCES

In Partial Fulfillment of the Requirements
For the Degree of

DOCTOR OF PHILOSOPHY

In the Graduate College

THE UNIVERSITY OF ARIZONA

2015

THE UNIVERSITY OF ARIZONA
GRADUATE COLLEGE

As members of the Dissertation Committee, we certify that we have read the dissertation prepared by Vaibhav Joga Singh Bora entitled Photon Statistics in Scintillation Crystals and recommend that it be accepted as fulfilling the dissertation requirement for the Degree of Doctor of Philosophy.

Date: 15 May 2015

Harrison H. Barrett

Date: 15 May 2015

Lars Furenlid

Date: 15 May 2015

Eric Clarkson

Date: 15 May 2015

H. Bradford Barber

Final approval and acceptance of this dissertation is contingent upon the candidate's submission of the final copies of the dissertation to the Graduate College.
I hereby certify that I have read this dissertation prepared under my direction and recommend that it be accepted as fulfilling the dissertation requirement.

Date: 15 May 2015

Dissertation Director: Harrison H. Barrett

STATEMENT BY AUTHOR

SIGNED: Vaibhav Joga Singh Bora

ACKNOWLEDGEMENTS

I would like to thank Harry for all the guidance, patience and time he invested into me and my PhD. Lars Furenlid, Eric Clarkson and Brad Barber made themselves very approachable and always took out time to answer all my questions, and for discussions about all things under the sun. I would like to thank Tom Milster who advised and guided me on a couple of very rewarding optics projects during my PhD. Radiation monitoring Devices, Boston has manufactured, and shared with us the latest new scintillation materials. I am very thankful for their support for my dissertation.

David Fastje tremendously helped me with the experiments. He made some very nice measurements which are a part of this thesis. I would like to thank Helen, Esen, Cecile, Jin, Ronin, Joy, Ling, Xin, Nasrin, Maria, Chris, Kyle, George, Daniel, Luca, Abhinav, Heather, Brian, Steven and Jared for sharing their time, letting me pick their brain and helping me along with technical advise, life guidance, or kind words. My PhD experience would have been hollow without all of you.

I would also like to Thank Merry Warner, Christy and Liz Hague for helping me buying all the lab supplies and keep the lab running.

DEDICATION

I would like to dedicate my PhD thesis to my family. To my sweetheart Lakshmi, who moved twice so that I could enroll and complete my PhD, my daughter Kavya, who has brought so much joy to our lives, my parents Joga Singh and Chandra who have raised me to be the person I am today, my sisters, Anjana and Vaishali, who have always looked out for me and are just awesome and my in-laws Gopalakrishnan and Visalakshi who have encouraged and supported me throughout my Phd.

I would also like to give a big shout-out to Anirban, Anubhab and Niladri who opened their homes and hearts to me. Thanks for all the great dinners and discussions.

Lastly, my Toyota Matrix, who through our 200K miles journey has not failed me once.

TABLE OF CONTENTS

TABLE OF CONTENTS – *Continued*

TABLE OF CONTENTS – *Continued*

TABLE OF CONTENTS – *Continued*

LIST OF FIGURES

LIST OF FIGURES – *Continued*

LIST OF FIGURES – *Continued*

LIST OF FIGURES – *Continued*

LIST OF FIGURES – *Continued*

LIST OF TABLES

ABSTRACT

Scintillation based gamma-ray detectors are widely used in medical imaging, high-energy physics, astronomy and national security. Scintillation gamma-ray detectors are field-tested, relatively inexpensive, and have good detection efficiency. Semiconductor detectors are gaining popularity because of their superior capability to resolve gamma-ray energies. However, they are relatively hard to manufacture and therefore, at this time, not available in as large formats and much more expensive than scintillation gamma-ray detectors.

Scintillation gamma-ray detectors consist of: a scintillator, a material that emits optical (scintillation) photons when it interacts with ionization radiation, and an optical detector that detects the emitted scintillation photons and converts them into an electrical signal.

Compared to semiconductor gamma-ray detectors, scintillation gamma-ray detectors have relatively poor capability to resolve gamma-ray energies. This is in large part attributed to the "statistical limit" on the number of scintillation photons. The origin of this statistical limit is the assumption that scintillation photons are either Poisson distributed or super-Poisson distributed. This statistical limit is often defined by the Fano factor.

The Fano factor of an integer-valued random process is defined as the ratio of its variance to its mean. Therefore, a Poisson process has a Fano factor of one. The classical theory of light limits the Fano factor of the number of photons to a value greater than or equal to one (Poisson case). However, the quantum theory of light allows for Fano factors to be less than one.

We used two methods to look at the correlations between two detectors looking at same scintillation pulse to estimate the Fano factor of the scintillation photons. The relationship between the Fano factor and the correlation between the integral of

the two signals detected was analytically derived, and the Fano factor was estimated using the measurements for SrI_2:Eu, YAP:Ce and CsI:Na.

We also found an empirical relationship between the Fano factor and the covariance as a function of time between two detectors looking at the same scintillation pulse. This empirical model was used to estimate the Fano factor of $LaBr_3$:Ce and YAP:Ce using the experimentally measured timing-covariance. The estimates of the Fano factor from the time-covariance results were consistent with the estimates of the correlation between the integral signals.

We found scintillation light from some scintillators to be sub-Poisson. For the same mean number of total scintillation photons, sub-Poisson light has lower noise. We then conducted a simulation study to investigate whether this low-noise sub-Poisson light can be used to improve spatial resolution. We calculated the Cramér-Rao bound for different detector geometries, position of interactions and Fano factors. The Cramér-Rao calculations were verified by generating simulated data and estimating the variance of the maximum likelihood estimator. We found that the Fano factor has no impact on the spatial resolution in gamma-ray imaging systems.

CHAPTER 1

Introduction

Gamma-ray detectors are used in a number of different applications such as astronomy, medical imaging, high-energy physics and national security. Unlike optical imaging systems which detect the integral of signals from a large number of photons, gamma-ray imaging systems detect and count individual gamma-ray photons. Counting individual gamma-ray photons is possible because most applications have a small rate at which gamma-ray photons are incident on a gamma-ray detector (less than 100,000 gamma-ray interactions per second), and the high energy of the gamma-ray photons enables us to get a good signal-to-noise ratio.

In this chapter, we describe the various components of a Single Photon Emission Computed Tomography (SPECT) gamma-ray imaging system. We then describe one of components of the SPECT systems – the gamma-ray detector in more detail in Sec. 1.2. In Sec. 1.3, we introduce and define the Fano factor, and in Sec. 1.4 we describe the motivation for our study. We then discuss the types of gamma-ray interactions in matter and types of gamma-ray detectors. These topics provide us the background to understand the next sections. We conclude the introduction by showing a typical energy spectrum from a gamma-ray interaction, define energy resolution and explain why energy resolution is important for an imaging detector.

1.1 Single Photon Emission Computed Tomography

A ligand is a small molecule that attaches itself with a biomolecule to serve a biological function. A radioactive isotope which emits gamma rays is added to a ligand to make a radioligand. The SPECT technique involves injecting a radioligand into a patient and imaging it to make a 3D map of the concentration of the radioligand. A SPECT imaging system has three main components - an image forming element, an imaging detector and a reconstruction algorithm (Kupinski and Barrett, 2005).

At gamma-ray wavelengths, most materials have a refractive index close to one. Therefore, gamma-ray imaging systems do not have lenses or mirrors as image forming elements. The two most commonly used image forming elements are the parallel-hole collimator and the pinhole collimator.

The parallel hole collimator (see in Fig. 1.1) allows only a small range of angles of gamma-rays to interact with the gamma-ray imaging detector. The pinhole collimator in Fig. 1.2 attenuates most gamma-rays, allowing only gamma-rays passing through it to interact with the detector. More advanced image forming elements like coded apertures, multi-pinhole apertures (Barrett and Myers, 2004) and synthetic collimators (Clarkson et al., 1999) increase the sensitivity of the detector while minimizing the impact on resolution.

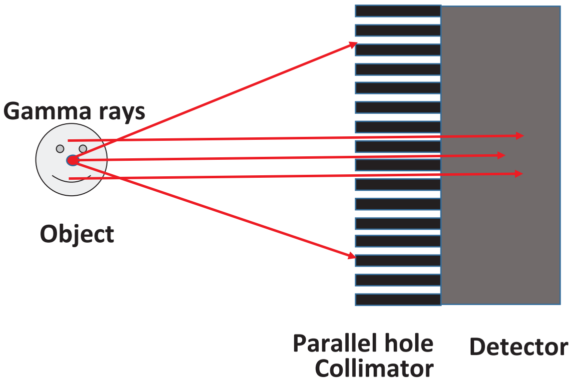

Figure 1.1: A parallel-hole collimator limits the angles of gamma-rays that interact with the collimator.

The gamma-ray imaging detector estimates the position of interaction and the energy deposited (x, y, z, E) in the gamma-ray interaction. The estimated position of interaction and the position of the pinhole or the angle of the collimator give us information about the line along which the gamma-ray was emitted. A reconstruction algorithm uses this information from multiple projections of the object (for example, by moving the image forming element and detector around the object) to make a 3D map of the gamma-ray emission from the object. The reason for estimating the energy will be explained in Sec. 1.7.1.

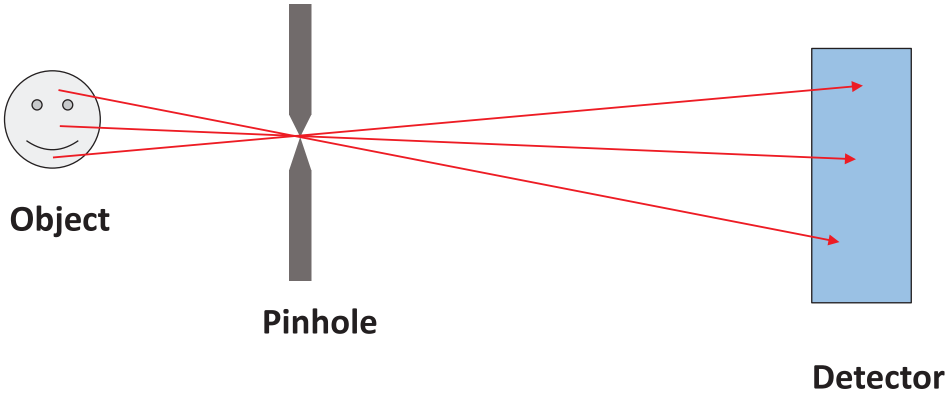

Figure 1.2: The object emits gamma-rays in all directions, but only a few gamma-rays pass through the pinhole to be detected by the gamma-ray detector. The detector estimates the position of interaction in x, y, z to enable us to draw a line though the pinhole to the source.

The spatial resolution of the gamma-ray imaging detector is defined in terms of the ability to resolve the position of interaction of the gamma-rays in the imaging detector, while the spatial resolution of a SPECT imaging system is defined in terms of the ability to resolve the position of the radioisotope in the object. In the parallel-hole and the pinhole collimator, errors in the estimation of the position of interaction of the gamma-ray in the gamma-ray imaging detector are propagated through the reconstruction algorithm into an error in the reconstructed object. In this dissertation, we use the term spatial resolution with respect to the imaging detector.

1.2 Gamma-ray spectrometers and gamma-ray imaging detectors

Gamma-ray detectors can be broadly classified into gamma-ray spectrometers and gamma-ray imaging detectors. A gamma-ray spectrometer is an instrument that is used to measure the distribution of the intensity of gamma-ray energies. It is widely used to detect and identify radiation sources. A gamma-ray imaging detector is a device that is used to image gamma-ray emitting isotopes. It measures the position of interaction and the energy of incident gamma-rays. To estimate the position of interaction, the gamma-ray imaging detector usually has multiple detector elements, or some other mechanism for creating position sensitive detector outputs.

Scintillation refers to emission of light in a material when it interacts with ionizing radiation. A scintillator is a material that exhibits scintillation. A gamma-ray scintillation detector consists of two main parts – a scintillator and an optical detector. The scintillator interacts with a gamma-ray photon and emits multiple optical photons. The optical photons emitted by the scintillator are detected by the optical detector, which generates an electrical signal.

A gamma-ray spectrometer is used to detect and identify radiation sources (see Fig. 1.3 for a scintillation gamma-ray spectrometer). The gamma-ray spectrometer estimates the energy deposited by every gamma-ray interaction, but has very little information on the position of interaction - limited to the fact that a gamma-ray interaction took place in its sensitive volume.

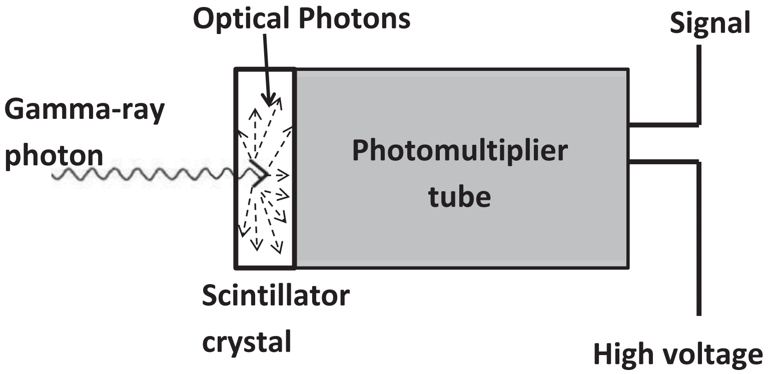

Figure 1.3: Schematic diagram of a gamma-ray spectrometer scintillation detector. Some photons emitted by the scintillator are detected by an optical detector and amplified to generate a signal.

A gamma-ray imaging detector is a device that is used to image gamma-ray emitting isotopes. It measures the position of interaction and energy of the incident gamma-rays. To estimate the position of interaction, a gamma-ray scintillation imaging detector usually has multiple optical detectors. If the scintillation light only produced a signal in the optical detector directly underneath it, we can only estimate that the gamma-ray interaction took place near that detector. However, if we spread the light to multiple optical detectors, we can compare the outputs from multiple detectors to improve the estimates of the position of interaction. This spreading of light to multiple detectors is achieved by using a light guide between the scintillator and the optical detectors. The Fig. 1.4 shows the schematic diagram of a gamma-ray imaging scintillation detector.

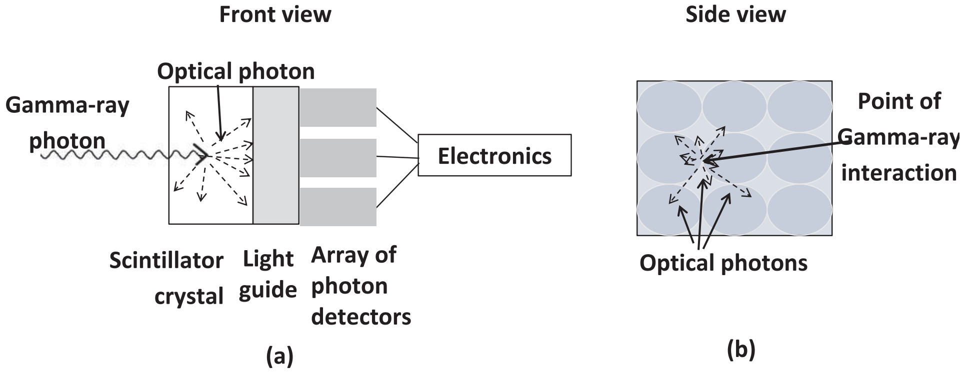

Figure 1.4: The gamma-ray scintillation detector consists of a scintillator crystal, a light guide and an array of optical detectors. When a gamma-ray photon interacts in the scintillator crystal, the scintillator crystal emits optical photons. The light guide ensures that the scintillation light is spread to multiple detectors. The optical detectors detect the scintillation photons and generate an electrical signal. This signal is used to estimate the position of interaction and energy of the gamma-ray. The sub-figure (b) shows the side view of the gamma-ray imaging detector. The array of optical detectors are more clearly visible in this view.

1.3 Statistics in gamma-ray imaging

The emission and detection of gamma-rays are probabilistic. There is randomness in the position of interaction in the detector, randomness in the type of interaction (Compton or photoelectric), randomness in the processes associated with generation of signals in the detector, including randomness from K x-ray or Auger electron and randomness in the de-excitation of the high energy electron.

Therefore, when a gamma-ray is detected, the signals generated by the detectors are also not deterministic, but have some associated variance. The variance in the number of information carriers (scintillation photons in scintillators, or charge carriers in semiconductor and gas detectors) is characterized by a factor known as the Fano factor.

1.3.1 Fano factor

The Fano factor (F_N) has been defined to quantify the departure of the observed fluctuations in an integer-valued random variable N from Poisson statistics (Fano, 1947):

$$F_N = \frac{\sigma_N^2}{\sigma_{Poisson}^2}. \tag{1.1}$$

Here, σ_N^2 is the variance of N, and $\sigma_{Poisson}^2$ is the variance of the Poisson-distributed random variable with mean $\overline{N}$. For a Poisson random variable, as $\sigma_{Poisson}^2 = \overline{N}$, we rewrite Eq. 1.1 as

$$F_N = \frac{\sigma_N^2}{\overline{N}}. \tag{1.2}$$

For a semiconductor or gaseous radiation detector, the Fano factor is defined using the number of charge carriers produced, while for a scintillation detector, the Fano factor is defined using the number of scintillation photons emitted.

Based on its Fano factor, the random variable N can be divided into three categories: sub-Poisson ($F_N < 1$), Poisson ($F_N = 1$) and super-Poisson ($F_N > 1$).

1.4 Motivation for measuring Fano factor

1.4.0.1 Improving the spatial resolution of gamma-ray imaging detectors

In a gamma-ray imaging detector, the various parameters that describe the interaction of the gamma-ray photon with the detector, such as the position of interaction and energy deposited by a detected gamma-ray photon, are estimated using the detector outputs. Since a reduction in the Fano factor results in a smaller variance in the number of emitted optical photons and consequently a smaller variance in the detector outputs, we would expect that this should also lead to reduction in variance of the parameters estimated from the low-variance detector outputs. Thus, a variation in Fano factor could potentially affect the energy and spatial resolution of a gamma-ray imaging system.

Reconstruction techniques like maximum likelihood estimation use a statistical model for estimating the position of interaction and energy deposited in a detector. An accurate estimate of the Fano factor will help us build a better statistical model and could improve the spatial resolution.

1.4.0.2 Challenging widely accepted assumptions

It was widely accepted that the Fano factors of all scintillators have values equal to or greater than one. The plot in Fig. 1.5, a compilation of data from many publications illustrates this belief (Moses, 2002). The energy resolution measurements shown in the plot are affected by a number of factors such as randomness in the position of interaction, gain variance of detectors, K escape and other loss mechanisms which increase the variance of the signals.

Efforts to quantify the factors contributing to the energy resolutions in scintillators have often assumed the Fano factor of scintillators to be one (Payne et al., 2011; Fiorini et al., 2005; Alekhin et al., 2013; Seifert et al., 2012).

1.4.0.3 Non-classical light

Classical wave theory restricts the Fano factor of light to values greater than one (Saleh, 1977). Quantum theory of light does not preclude values of Fano factor less than one. Therefore light with Fano factors less than one is also referred to as non-classical light. Generation and measurement of non-classical light is an active area of research and measurement of Fano factors less than one in scintillation crystals is of significant interest to the quantum optics community.

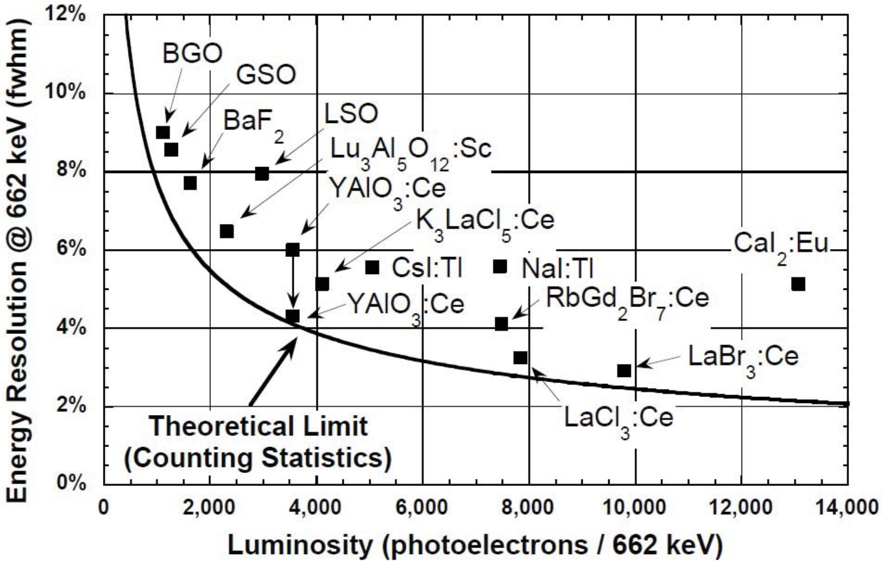

Figure 1.5: The plot shows the published energy resolutions as a function of the total number of photoelectrons detected for a number of scintillators. The solid line is the energy resolution of a Poisson process for a given number of photoelectrons. The energy resolution of all the scintillators shown in the figure are larger than the Poison limit. Reprinted from Nuclear Instruments and Methods in Physics Research A , Vol 487, W. Moses, Current trends in scintillator detectors and materials, 123-128, Copyright (2002), with permission from Elsevier.

1.5 Gamma-ray interactions in matter

The attenuation of a pencil beam of monochromatic gamma rays along its path is given by Beer's law

$$I(x) = I_o e^{-\mu x}. \tag{1.3}$$

Here, x is the depth inside the material with units of meters, μ is the linear coefficient of absorption with units of inverse meters, I_o is the average number of gamma rays per unit area at $x = 0$, $I(x)$ is the average number of gamma rays traveling along the incident beam x meters inside the material. We can calculate μ as

$$\mu = n_e \sigma_e. \tag{1.4}$$

Here, n_e is the electron density in m^{-3}, and σ_e is the collision cross-section in m^2. The three types of interactions of gamma-rays in matter that are important for radiation measurements are photoelectric absorption, Compton scattering and pair production. Rayleigh scattering is the dominant elastic scattering of electromagnetic waves when the wavelength is much bigger than the particle sizes. It is not significant at gamma-ray wavelengths, hence, we neglect the Rayleigh scattering cross section in this discussion. The total cross-section σ_e can be divided into the photoelectric cross-section (σ_{pe}), the Compton cross-section (σ_C) and the pair-production cross-section (σ_{pp}).

$$\sigma_e = \sigma_{pe} + \sigma_C + \sigma_{pp}. \tag{1.5}$$

1.5.1 Photoelectric interaction

A photoelectric interaction is an interaction between a photon and an electron in which all the energy of the photon is transferred to the electron (see Fig. 1.6). Each atom has a number of energy shells which may be occupied by electrons. The electrons occupying the different shells are bound to the nucleus by different amounts of binding energies. Therefore, in a photoelectric interaction between a gamma-ray photon of energy E_γ and an electron bound by a binding energy E_B, the kinetic energy E_e of the electron after the interaction is equal to the difference between the gamma-ray photon energy and the binding energy of the electron.

$$E_e = E_\gamma - E_B. \tag{1.6}$$

The momentum of the photoelectric interaction is conserved by transferring the gamma-ray photon momentum to the ejected electron and the nucleus of the atom.

When the electron is ejected from an atom, it leaves behind a vacancy in its shell. This vacancy in the shell has the binding energy (E_b), which is either lost to

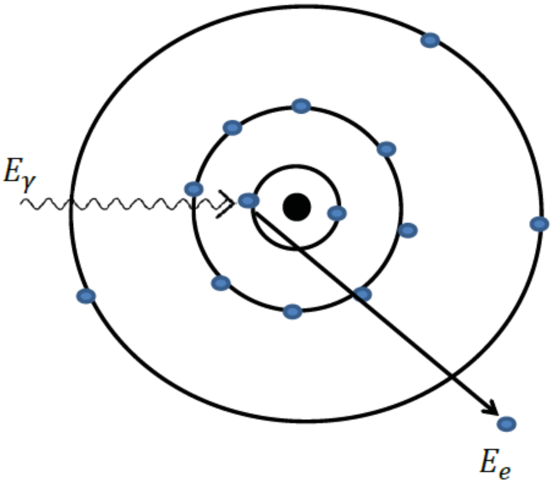

Figure 1.6: In a photoelectric interaction, all of the gamma-ray energy is transferred to an electron, creating a free electron with energy E_e and a vacancy in the corresponding shell with energy equal to the binding energy of the electron. The momentum of the gamma-ray is transferred to the interaction electron and the nucleus of the atom.

an X-ray photon or to an Auger electron (see Fig. 1.7). This X-ray photon can be absorbed in the material or escape, while the energy of the Auger electron is usually dissipated in the material.

If the gamma-ray energy of the photon is greater than the binding energy of the electron, the empirically estimated photoelectric cross-section is given by

$$\sigma_{pe} \approx k \frac{Z^m}{(E_\gamma)^n} \frac{\rho}{A}. \tag{1.7}$$

Here, k is a constant that depends on the shell involved, Z is the atomic number, A is the atomic mass, and ρ is the density of the material. The constants m varies between 4 and 5, while n varies between 3.5 to 1, for different values of Z and E_γ. The discontinuities in the photoelectric cross-section correspond to the shell energies. As E_γ increases beyond a shell energy gap, an additional transition contributes to the photoelectric cross-section resulting in a sharp jump in σ_{pe}.

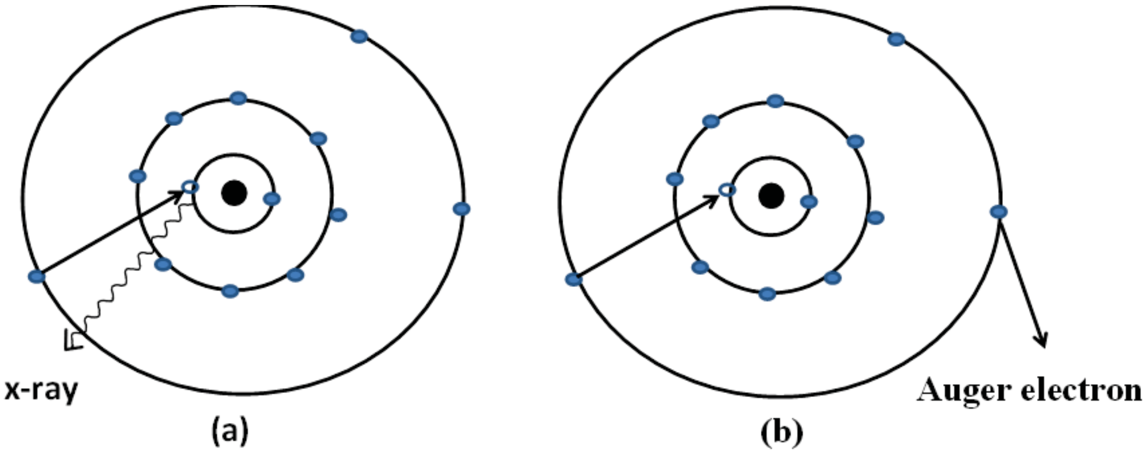

Figure 1.7: The photoelectric effect creates a vacancy in an electron shell. This vacancy in an inner shell is filled by an electron from an outer shell and energy differnt between the two shells is released either (a) through an x-ray photon emission or (b) through an Auger electron.

1.5.2 Compton interaction

In a Compton interaction, the gamma-ray photon interacts with an electron and transfers a part of its energy to the electron. The scattered gamma-ray photon has energy E'_γ, while the electron has energy $E_\gamma - E'_\gamma$ (see Fig. 1.8). If θ is the angle between the original gamma-ray photon and the scattered gamma-ray photon, the following equation can be derived from the laws of conservation of momentum and conservation of energy

$$E'_\gamma = \frac{E_\gamma}{1 + \frac{E_\gamma}{m_e c^2}(1 - \cos\theta_C)}. \tag{1.8}$$

Here, m_e is the mass of an electron, and c is the speed of light.

The angular distribution of the scattered gamma rays is predicted by the Klein-Nishina formula (Barrett and Swindell, 1981),

$$\frac{d\sigma_c}{d\Omega} = Z r_0^2 \left(\frac{1}{1 + \kappa(1 - \cos\theta)} \right)^2 \left(\frac{1 + \cos^2\theta}{2} \right) \left(1 + \frac{\kappa^2 (1 - \cos\theta)^2}{(1 + \cos^2\theta)(1 + \kappa(1 - \cos\theta))} \right). \tag{1.9}$$

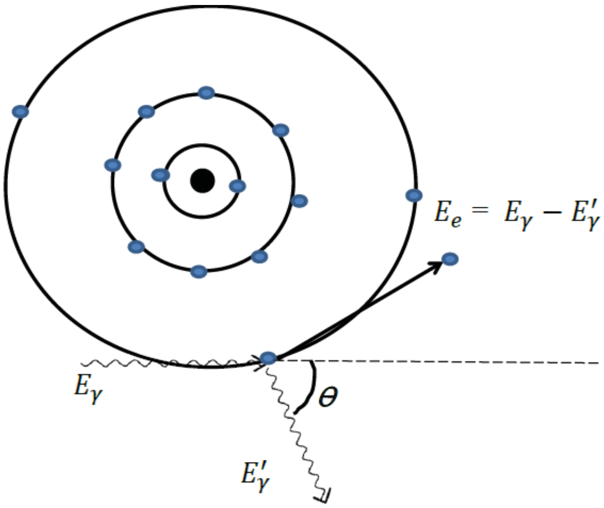

Figure 1.8: In a Compton scattering event, the gamma-ray scatters and loses some of its energy to an electron.

Here, Ω is the solid angle, $\frac{d\sigma}{d\Omega}$ is the differential scattering cross section, $\kappa = \frac{E'_\gamma}{m_e C^2}$, and r_0 is the classical electron radius.

1.5.3 Pair production

Pair production is the creation of an elementary particle and its antiparticle, usually from the interaction of a photon with the nucleus. In the electric field of a nucleus or an electron, the high-energy gamma ray can produce an electron and a positron. Pair production is The energy required to produce an electron and positron is given by $2\times E_e = 2\times m_e c^2 = 1022$ keV. The excess gamma-ray photon energy is converted into kinetic energy shared by the electron and the positron produced in the interaction. The pair production cross section increases with the incident gamma-ray energy; thus, it is the predominant interaction mechanism at high energies.

$$\sigma_{pp} \propto Z^2 ln(2E_\gamma), \forall E_\gamma > 1.02MeV. \tag{1.10}$$

The photoelectric, Compton, pair production and total cross-sections of tungsten as a function of energy were generated from the NIST website and plotted in Fig.

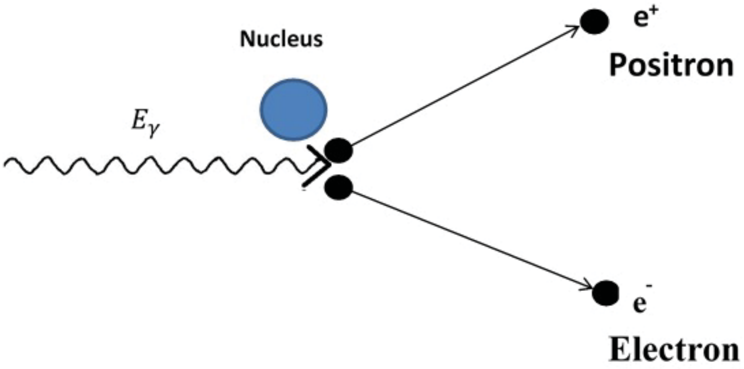

Figure 1.9: Pair production occurs in the electric field of the nucleus or an electron. The gamma-ray interaction produces an electron and a positron. The gamma-ray energy left after producing the electron and positron ($E_\gamma - 1022$ KeV), is imparted as kinetic energy to the electron and the position.

1.10 (Berger et al., 2014).

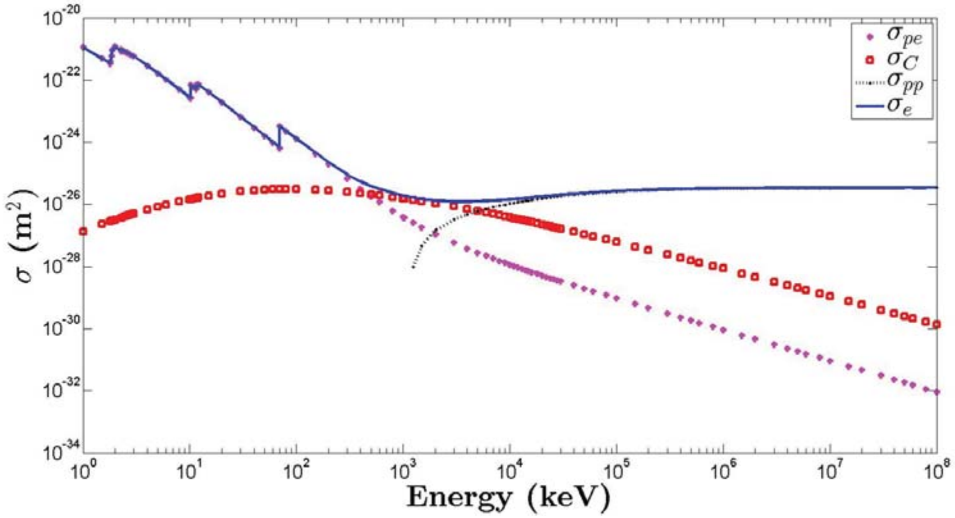

Figure 1.10: Photoelectric, Compton and Pair production cross sections in tungsten as a function of incident gamma-ray energy. As the gamma-ray energy increases, the photoelectric and Compton cross-sections decrease. Pair production is dominant in the higher gamma-ray energies for $E_\gamma > 1.022$ MeV. The data in this graph is reproduced from (Berger et al., 2014).

1.6 Types of gamma-ray detectors

Gamma rays interact strongly with matter to produce ionization. As shown above, the interaction usually produces a high-energy electron which interacts with other electrons to free them. This charge is either directly collected (in semiconductor detectors or gas detectors), or converted to light (in scintillation detectors) to detect the presence of gamma-rays or estimate the energy of the gamma-ray. Here we briefly discuss the different types of gamma-ray detectors.

1.6.1 Gas detectors

Gas detectors consist of a gas between two electrodes. A gamma-ray interaction ionizes the gas and produces free electrons and ions. As shown in Fig. 1.11, a high voltage is applied between the two electrodes to separate the electrons and ions, resulting in a current signal. There are three main types of gas detectors – the ionization chamber, the proportional counter, and the Gieger-Mueller counter.

An ionization chamber has a relatively low voltage between its two electrodes. Therefore, the electric field separates, and collects the charge produced by the direct ionization, but does not amplify it.

Proportional counters operate at a higher voltage than an ionization chamber. Like an ionization chamber, the proportional counter uses its electric field to separate the charge produced by the gamma-ray interaction. The most common proportional counter uses a thin wire ($\sim$ 50 micron diameter) as the anode to collect the electrons. Due to the geometry the electric field varies inversely with the distance from the anode. Thus, when an electron is within a fraction of a cm of the anode, it can be sufficiently accelerated to ionize another atom and liberate an electron. The liberated electron is also accelerated, and the ensuing cascade typically yields a gain of 10^4 to 10^5. The output current of a proportional counter has a linear relationship with the energy deposited in a gamma-ray interaction.

A Geiger-Mueller (GM) counter is a gas detector which has an even higher voltage between the electrodes than the proportional counter. Just as in the proportional counter, the electrons near the anode are sufficiently accelerated to produce an avalanche. Because of the higher accelerations, the avalanche of electrons also emit ultraviolet (UV) photons. These UV photons can ionize other gas atoms, create multiple avalanches spread along the anode wire and ionize the adjacent volume. The avalanche is stopped by an external quenching circuit which detects the output signal and then reduces the voltage across the electrodes. Thus a single ion pair will result in the same output as a larger number of ion pairs. Therefore, the GM counter is very sensitive to the presence of gamma rays, but has no information about the energy of the gamma rays.

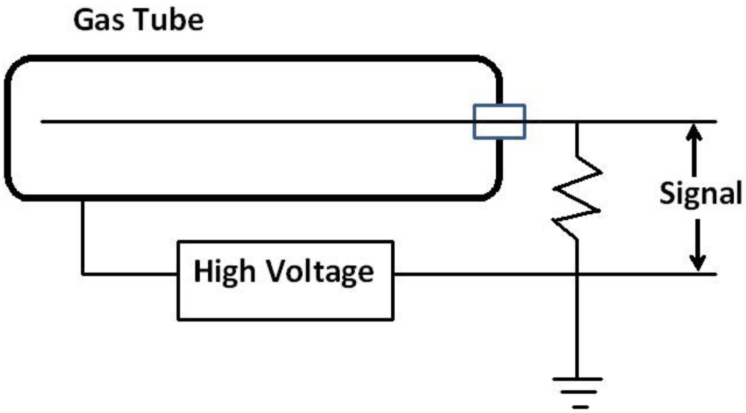

Figure 1.11: A gas detector consists of sensitive volume (gas) between two electrodes. In this figure, the metal container serves as one of electrodes, and a thin wire in the center of the tube is the other electrode.

1.6.2 Semiconductor detectors

Most semiconductor detectors are PN, PIN or Schottky junctions operated in reverse bias. A gamma-ray interaction in the depletion region creates electrons and holes which are then separated by the electric field in the depletion region. This movement of free charges results in a current flow in the material which is then detected at the electrodes. There are also photo-conductive semiconductor detectors as shown in Fig. 1.12.

Silicon, high-purity germanium, cadmium telluride and cadmium zinc telluride are examples of materials used to make semiconductor gamma-ray detectors.

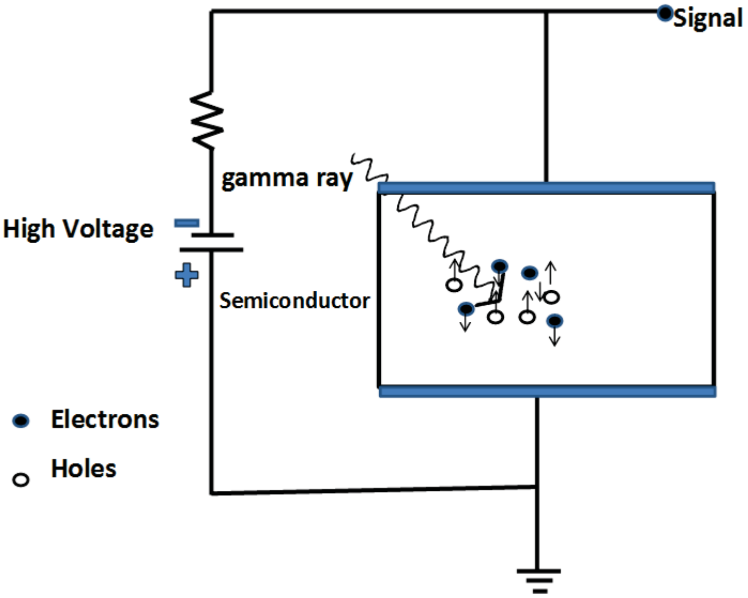

Figure 1.12: Schematic diagram of a photo-conductive semiconductor detector. The electric field applied across the detector separates the electrons and hole generated by the ionizing radiation and generates a current.

1.6.3 Scintillation detectors

Scintillation detectors emit optical photons when excited by ionizing radiation (see Fig. 1.3). When a gamma-ray photon interacts in a scintillation material, it produces a high-energy electron and a vacancy in an inner shell. The high-energy electron undergoes a complicated cascade process and loses its energy by ionizing the surrounding region to produce many free electrons and holes. Unlike a semiconductor or a gas detector where an electric field is used to separated and collect the electrons and holes, in a scintillation detector, a fraction of the electrons and holes form excitons. A fraction of these excitons decay radiatively.

The optical photons generated by the gamma-ray interaction are then detected by an optical detector with a large gain to generate an electrical signal. The physical processes in scintillation crystals will be discusses in more detail in the next chapter.

1.7 Energy resolution

The energy spectrum produced by 662 KeV gamma ray interactions in a $LaBr_3$:Ce scintillation gamma-ray detector is shown in Fig. 1.13. As the energy of the gamma-ray was below the energy to create an electron-hole pair, only photoelectric and Compton interactions take place in the crystal. The gamma-ray events which result in the deposition of all the energy into the detector are labeled as photopeak events. After a photoelectric interaction, energy in the form of x-rays can leave the detector. The most prominent of these x-ray losses are due to the K x-rays. The gamma-ray events corresponding to a photoelectric interaction followed by an escape of a K x-ray from the crystal are labeled as “K-escape” in Fig. 1.13. The Compton interaction deposits a fraction of the initial gamma-ray energy in the detector, losing the rest of the energy to a secondary gamma-ray. This results in the continuous Compton region in the energy spectrum. The amount of energy deposited in the detector is a function of the angle between the incident gamma ray and the scattered gamma ray. The maximum gamma-ray energy is deposited in the detector when the scattered gamma-ray, scatters at an angle of 180° from the incident gamma-ray. This energy, known as the Compton edge, marks the high energy bound of the Compton region in the energy spectrum, separating it from the photopeak region. A secondary gamma-ray from a Compton interaction can undergo a photoelectric interaction and deposit its energy into the scintillation crystal. This interaction will also have energy in the photopeak region of the energy spectrum.

The energy resolution of a detector is defined as the ratio of the Full Width at Half Maximum (FWHM) of the photopeak and the mean value of the photopeak.

$$\mathrm{ER} = \frac{\mathrm{FWHM}}{\text{mean photopeak}}. \tag{1.11}$$

The energy resolution is an important property of a gamma-ray detector. A smaller

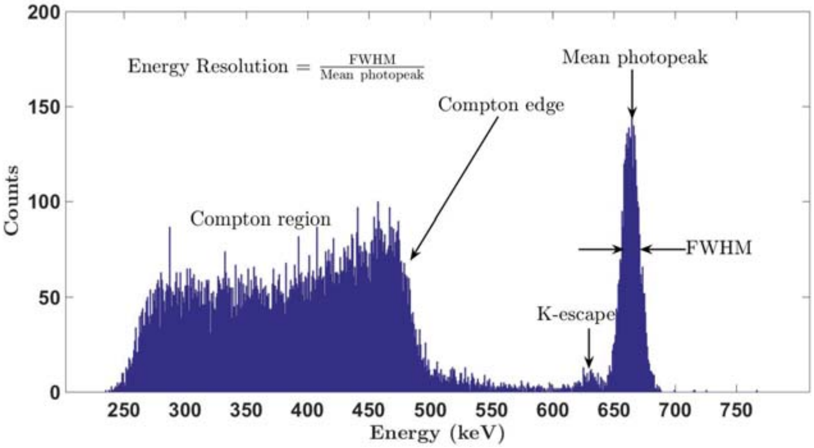

Figure 1.13: The energy spectrum of a gamma-ray detector is shown above. The scintillation crystal used in this measurement was $LaBr_3$:Ce. The photopeak, K-escape and the Compton region are labeled in the graph.

energy resolution would imply a narrower photopeak which will enable a gamma-ray detector to distinguish between closer gamma-ray energies (Knoll, 2010).

1.7.1 Why we need to estimate energy in a gamma-ray imaging detector

In the preceding sections, we have discussed Compton interaction and how a scattered gamma-ray photon travels in a direction that is different from the original gamma-ray photon. A gamma-ray photon can undergo Compton scattering in the detector, or in the object. The scattered gamma-ray has lost most of the information about the position where it was emitted. Tracing the line from the position of interaction of a Compton scattered gamma-ray photon in the detector through the pinhole does not lead to the position at which the gamma-ray was emitted (see Fig. 1.14). As most gamma-ray imaging detectors cannot distinguish between a Compton-scattering event in the object followed by a photoelectric event in the detector, and a Compton-scattering event in the detector, to preserve the quality of the measurement, all Compton scattered events are usually discarded. We use the fact that the Compton scattered photons have an energy lower than the unscattered photons to threshold the gamma-ray interactions above the Compton edge. This

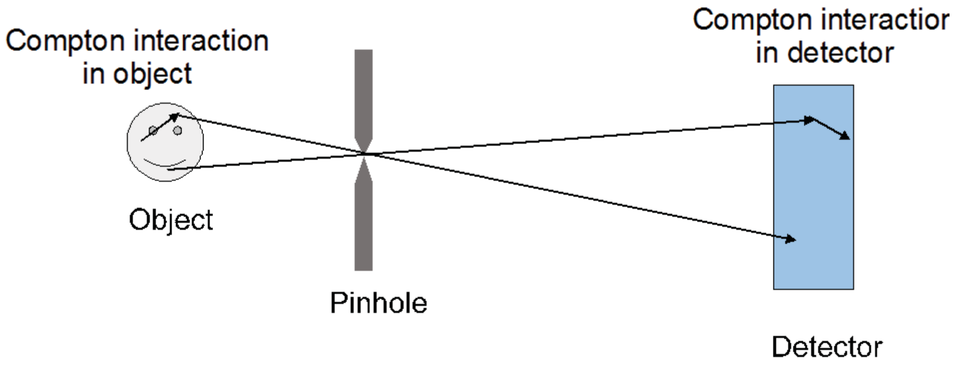

Figure 1.14: Gamma-rays that have undergone Compton interactions in the object lose most of the information about the object.

energy thresholding also results in discarding good data from gamma-ray photons which had a Compton interaction in the gamma-ray detector followed by the escape of the scattered gamma-ray photon.

Windowing the energy spectrum does not eliminate all the Compton-scattered gamma-ray photons in the object. A low-angle Compton scattered gamma-ray photon which undergoes photoelectric interaction in the detector will appear to be in the photopeak region, and will reduce our system's spatial resolution. Therefore, a good energy resolution is important for an imaging detector. The low-angle Compton interaction along with loss mechanisms in the scintillator crystal results in the non-zero heights in Fig. 1.13 between the Compton edge and the photopeak.

CHAPTER 2

Inorganic Scintillation Detectors

Inorganic scintillation detectors are widely used for gamma-ray imaging as well as gamma-ray spectroscopy because they are relatively inexpensive, have high density and are a mature technology.

Based on the physical processes that result in luminescence, scintillation detectors can be classified as either activated scintillators (NaI:Tl, CsI:Na, SrI_2:Eu, etc.) self-activated scintillators (CsI, NaI, $CdWO_4$, etc.), or core-valence scintillators (BaF_2, CsF, $RdCaF_3$, etc.) (Derenzo and Weber, 1999). The activated scintillators have high light output and, therefore, are the most widely used. Hence, in this chapter, we focus on activated scintillators.

2.1 Physics of scintillation crystals

When a gamma ray interacts with a scintillator crystal, it undergoes a complicated cascade process to produce a scintillation photons (Rodnyi, 1997; Payne et al., 2009; Williams et al., 2011; Moses et al., 2012). The scintillation process can be divided into a general sequence of five stages (Rodnyi, 1997)

1. Gamma-ray interaction in matter: The gamma-ray interaction in the scintillator produces the primary high-energy electron and an inner shell vacancy.
2. Ionization: The high-energy electrons lose their energy by creating a number of secondary electrons, holes, phonons and photons.
3. Carrier thermalisation: The electrons and holes lose their energy primarily to phonons to form excitons.
4. Capture at dopant site: Energy transfer from the electron-hole pairs to the dopant sites.

5. Radiative emission: Emission of optical photons at the dopant sites.

Scintillation emissions do not necessarily follow all of the above steps. For example, the electrons and the holes can travel independently to the dopant site and form an exciton at the dopant site. Another possibility is the production of a geminate exciton – instead of producing free electrons and holes during the ionization process, an electron-hole pair is directly produced. Each step will now be discussed in more detail.

2.1.1 Gamma-ray interaction in matter

A gamma ray undergoing a photoelectric or Compton interaction in a scintillator produces a vacancy and a free electron. In a photoelectric interaction, the momentum from the gamma ray is transferred to the electron and the nucleus. Therefore, an inner-shell electron, which is more tightly coupled with the nucleus has a higher probability of a photoelectric interaction than an electron in the outer shell. The Compton interaction is more likely to occur with the outer-shell electrons than with the inner-shell electrons,.

The vacancy in the electron shell created in the interaction either relaxes non-radiatively by transferring energy to an Auger electron or radiatively by emitting an x-ray photon. The production of an x-ray photon or the Auger relaxation, can be a single transition from the inner shell to the outermost shell or a series of transitions involving intermediate shells, producing more x-rays or Auger electrons before finally reaching the ground state. The x-ray photon can be reabsorbed in the scintillator, resulting in another photoelectric or Compton interaction, or it can escape the scintillator.

2.1.2 Ionization

The free electron created from the primary gamma-ray interaction loses its energy to other electrons to create secondary free electrons. These secondary free electrons relax by ionizing the material and creating more secondary free electrons. The cascade process continues until all the electrons involved are unable to create more ionization. During the ionization process, significant energy is also lost to phonons. The ionization step is fast and is usually completed in 1-100 femtoseconds (Rodnyi, 1997).

2.1.3 Carrier thermalisation

When the electrons cannot lose any more energy to other bound electrons, they can only lose their excess energy to phonons. This electron-phonon interaction results in the electrons and the holes assuming a Fermi-Dirac distribution. The resulting electron-hole pairs have energy close to the band gap. The carrier thermalisation time is much longer than the ionization time and is of the order of 1-10 picoseconds (Rodnyi, 1997).

2.1.4 Capture at dopant site

A dopant introduced in a scintillation crystal has energy levels within the band gap of the crystal. Therefore, the free electrons in the conduction band, or the holes in the valence band, or excitons can lose energy and get trapped in a dopant site. The electrons and the holes can come to the dopant sites independently to make an exciton there, or they may come together as an exciton. The dopant concentration in the scintillator is an important parameter. A small dopant concentration might result in the charge carriers de-exciting before finding a dopant site. While a large dopant concentration will increase the probability that the electrons and holes are trapped in different dopant sites and de-excite non-radiatively (Derenzo and Weber, 1999).

2.1.5 Radiative emission

When an exciton is trapped in a dopant site, it has a high probability of recombining with the emission of a scintillation photon. Because the scintillation photon has energy less than the band gap (see Fig. 2.1), it has a low probability of absorption

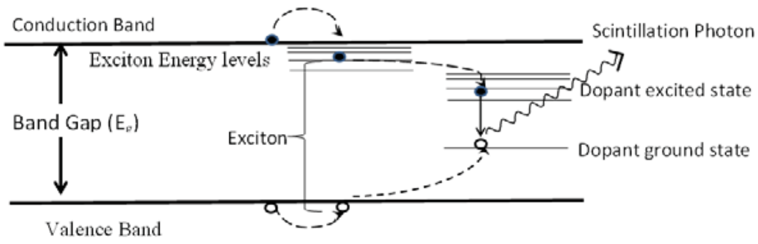

Figure 2.1: Band structure of an activated scintillator.

in the scintillator.

2.2 Properties of scintillation gamma-ray detectors

In this section, we discuss the different properties of scintillator crystals and how they affect measurement of gamma rays. Because no scintillator has all of the desirable properties, a scintillator is usually chosen based on trade-offs and constraints.

2.2.1 Light yield

The light yield (L_R) is defined as the number of optical photons emitted by unit gamma-ray energy.

$$L_R = \frac{\overline{N}_{ph}}{E_\gamma}. \tag{2.1}$$

Here, $\overline{N}_{ph}$ is the average number of optical photons emitted when E_γ energy is deposited in the crystal by a gamma-ray interaction. Let us use the knowledge of the different stages of the scintillation process discussed in the previous section to relate the light yield to the scintillator material.

Consider a scintillator material with a band gap E_g and average energy required to create an electron-hole pair E_{eh}. We can relate the E_{eh} and E_g by a material-dependent constant B.

$$E_{eh} = B \cdot E_g. \tag{2.2}$$

The value of B typically ranges from 1.5-2.0 for ionic crystals. Assuming that every electron-hole pair produces on average A optical photons $\big(A = \frac{\overline{N}_{ph}}{\overline{N}_{eh}} \leq 1\big)$, we can rewrite Eq. 2.1 as

$$L_R = \frac{A \cdot \overline{N}_{eh}}{E_\gamma} = \frac{A}{E_{eh}} = \frac{A}{B \cdot E_g}. \tag{2.3}$$

If all the electron-hole pairs were converted to scintillation photons, then we would have $A = 1$. The value of $B = \frac{E_{eh}}{E_g}$ has to be greater than or equal to one.

$$L_{Max} \approx \frac{1}{B \cdot E_g} \times 10^6 \text{photons/MeV} \tag{2.4}$$

For example, the band gap of SrI_2 is 5.5 eV (Li et al., 2013), if we assume $B = 1.5$, then $L_{Max} \approx 120,000$photons/MeV. The experimentally measured value of light yield of SrI_2:Eu is 100,000 photons /MeV.

2.2.2 Duration of scintillation pulse

A short scintillation pulse reduces the probability of overlap of two gamma-ray pulses and, therefore, increases the maximum number of individual gamma rays a scintillation detector can detect in unit time. A scintillation pulse can be modeled as a pulse with a rise time (τ_r), a fast decay time (τ_1), and a slow decay time (τ_2).

$$J(t) = J_1\big(-e^{-t/\tau_r} + e^{-t/\tau_1}\big) + J_2\big(-e^{-t/\tau_r} + e^{-t/\tau_2}\big), \quad t > 0. \tag{2.5}$$

Here, J_1 and J_2 are the contributions to the final light output from the fast and slow decay, respectively and have units of photons per second. Most scintillators have a fast rise time, which is much smaller than the decay time ($\tau_r \ll \tau_1$), and therefore, studies often assume the rise time to be zero.

2.2.3 Density

A good scintillator has high density. High density materials usually have atoms with higher atomic number (Z). A larger atomic number significantly increases the probability of photoelectric interactions. A higher density could also be a result of packing atoms closer together. This would mean that, for a given volume, a gamma-ray has to pass through more atoms in a material with higher density as compared to a material with which has the same type of atoms at a lower density. Therefore, a high density material has a greater probability of interacting and detecting an incident gamma-ray.

2.2.4 Optical properties

The two important optical properties for a scintillation crystal are the refractive index and absorption at the scintillation wavelengths. It is desirable for the scintillation crystal to transmit 100% of the scintillation light. The scintillation photons can be absorbed either by the dopant or by the crystal itself (self-absorption). To maximize transmission of scintillation light, it is also desirable to match the refractive indexes of the scintillator and the detector. Index-matching fluids or optical gels minimize light loss due to reflections.

2.2.5 Emission spectra

The scintillation light from different materials have different wavelength spectrum's (see Figs.2.2-2.4). Optical detectors usually are most sensitive to a certain band of wavelengths. To maximize the signal, it is desirable to maximize the overlap of the emission spectrum of the scintillator and the detector's optical sensitivity.

2.2.6 Other important properties

There are numerous other important properties such as the cost of the scintillator, the mechanical properties, radiation hardness and chemical properties like hygroscopicity.

2.3 Non-proportionality and the Fano factor

For gamma-ray interactions involving different gamma-ray energies, a proportional (or linear) scintillator emits the same mean number of photons per unit gamma-

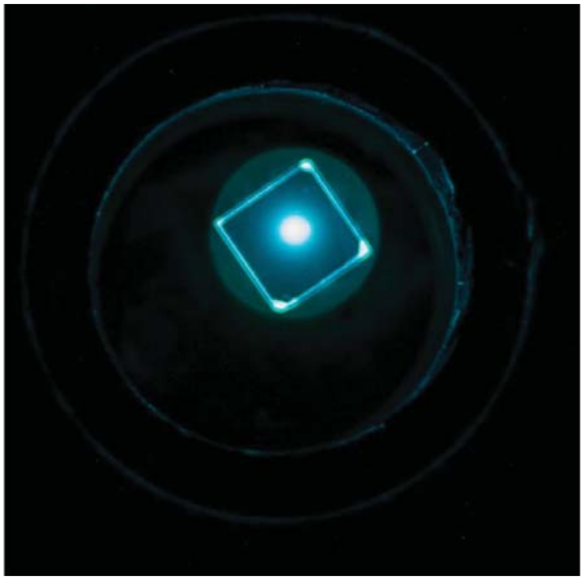

Figure 2.2: Scintillation light from $CdWO_4$. The scintillator was excited by a Co-57 source. This image was captured using a DSLR camera with a two-minute exposure. Photo courtesy of Joseph Ortiz.

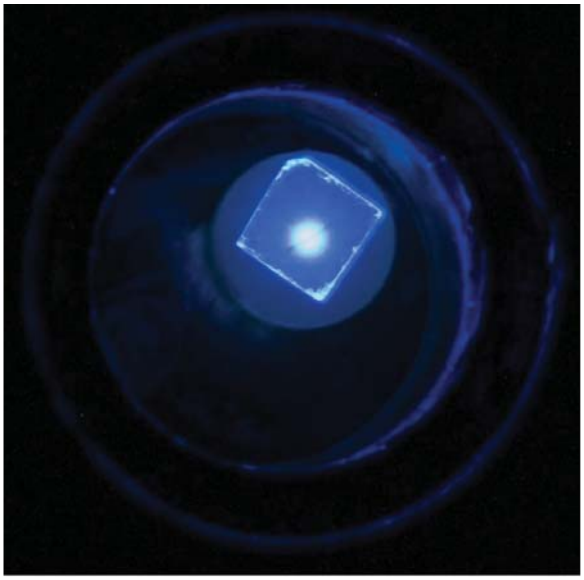

Figure 2.3: Scintillation light from CsI:Na. The scintillator was excited by a Co-57 source. This image was captured using a DSLR camera with a two-minute exposure. Photo courtesy of Joseph Ortiz.

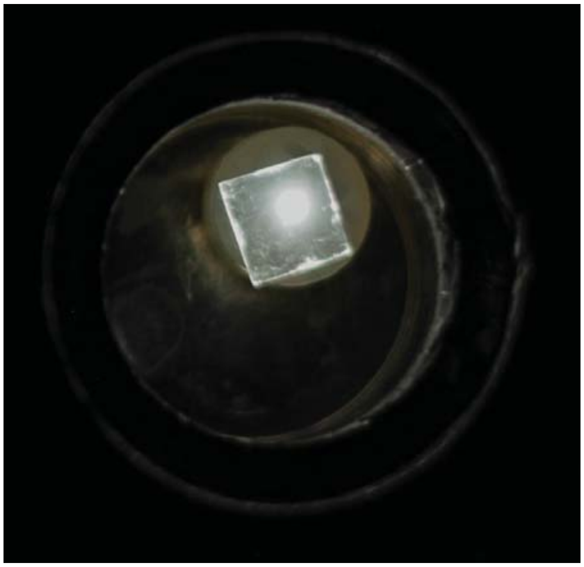

Figure 2.4: Scintillation light from CsI:Tl. The scintillator was excited by a Co-57 source. This image was captured using a DSLR camera with a two-minute exposure. Photo courtesy of Joseph Ortiz.

ray energy deposited. Therefore, in a proportional scintillator, the mean number of photons per unit gamma-ray energy varies linearly with deposited gamma-ray energy. The non-proportionality curves are a graph of the number of scintillation photons emitted per unit gamma-ray energy deposited vs the gamma-ray energy deposited in the crystal.

As the high-energy electron produced from the gamma-ray interaction loses its energy, it moves along the non-proportionality curve of the scintillator from right to left towards lower energies. Hence, the complete non-proportionality curve below the gamma-ray energy plays a significant role in the light output.

As the electron loses its energy in discrete steps, it effectively samples the non-proportionality curve. The process of de-excitation of the high-energy electron is a complicated cascade process. A delta ray is a high-energy electron created by secondary ionization. The high-energy electron can lose its energy to relatively low-energy electrons, to a high-energy delta ray, or a combination of both. Depending on the manner of the de-excitation of the high-energy electron, some regions of the

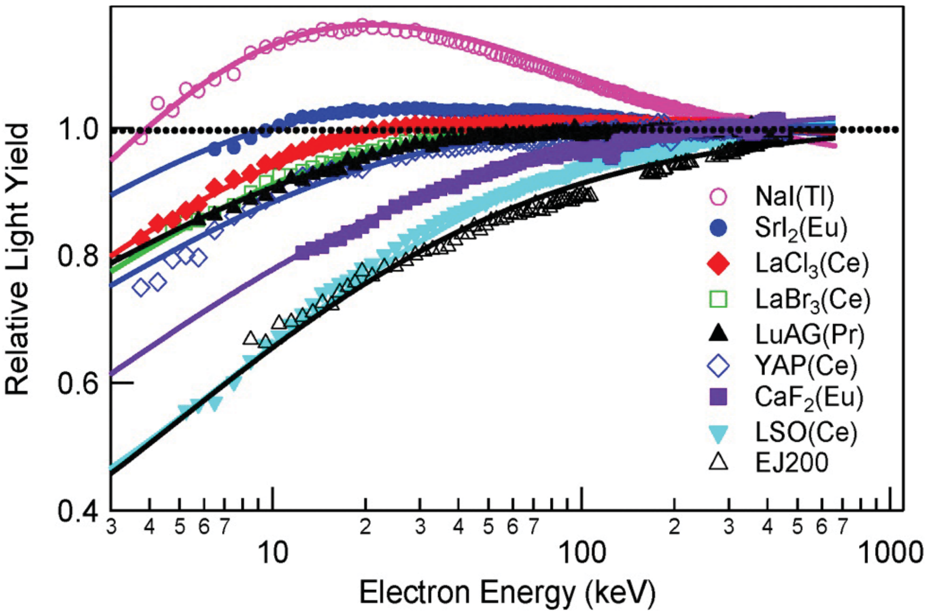

Figure 2.5: A proportional scintillator will have a value of 1 for all energies. The non-proportionality curves are normalized at 500 keV. The graph is reproduced from (Payne et al., 2011) ©2011, IEEE

non-proportionality curves are skipped while other regions of the non-proportionality curves are sampled multiple times.

If the non-proportionality curve is flat, then for a given gamma-ray energy deposited, the number of scintillation photons will be independent of the cascade path taken by the high-energy electron to lose energy. Thus, there would be no cascade-path dependent variance in the number of scintillation photons emitted, resulting in a lower scintillator Fano factor as compared to a scintillator with a non-flat non-proportionality curve.

The process of scintillation light production is a complicated cascade process. The gamma-ray interaction in a material ionizes the material and creates thousands of electron-hole pairs. In a semiconductor detector, these electron-hole pairs are directly detected and measured. Because the ionization mechanisms in the scintillation and semiconductor detectors are similar, it is a reasonable conclusion that the Fano factor of the electron-hole pairs produced in both these types of detectors should be in a similar range of 0.1-0.2. Therefore, the origin of the relatively higher Fano factor of the scintillation detectors is a result of processes after ionization.

After ionization, the scintillation process involves a few more steps, including carrier thermalisation, sequential capture by dopant sites and radiative relaxation. These steps depend on other factors, such as carrier diffusion length, the ratio of electron and hole diffusion lengths, carrier concentration and lifetimes (Williams et al., 2011). If the electrons have a much higher diffusion length than the holes, then the electrons are more likely to travel further from their ionization site and de-excite without coming in contact with the less mobile holes. Thus, similar electron and hole diffusion lengths result in better proportionality (Li et al., 2011). If the charge carrier density is very high, then the carriers have more competition for the same dopant sites. The probability of interactions such as exciton-exciton annihilation also increases.

CHAPTER 3

Estimation of Fano Factor in Inorganic Scintillators

This chapter is adapted from (Bora et al., 2011) and it extends the work of (Bousselham et al., 2010).

3.1 Introduction

The Fano factor of an integer-valued random variable is defined as the ratio of its variance to its mean (Fano, 1947). A Poisson random variable has a Fano factor of one, a sub-Poisson random variable has a Fano factor less than one and a super-Poisson random variable has a Fano factor greater than one. For a given energy deposited in a scintillator crystal by a gamma-ray photon, the Fano factor (F_N) for the number of scintillation photons is defined as

$$F_N = \frac{\sigma_N^2}{\overline{N}}. \tag{3.1}$$

When a gamma-ray photon of energy E undergoes photoelectric interaction with an electron having binding energy B in a semiconductor or a scintillation detector, it produces a high-energy photoelectron with energy equal to the difference between the energy of the gamma-ray photon and the binding energy ($E - B$). The binding energy of the electron is released either as an x-ray photon (which can escape or be reabsorbed in the scintillator) or as an Auger electron. The high-energy photoelectron loses its energy in a complicated random cascade process, producing thousands of secondary electrons and holes (Knoll, 2010; Kupinski and Barrett, 2005).

In semiconductor detectors like Si and Ge, the free electrons and holes produced by the gamma-ray interactions are separated using an applied electric field. Electron Fano factors in the range of 0.05-0.10 have been reported for semiconductors (Devanathan et al., 2006).

In a scintillator, the process of producing optical photons is more complicated; a free electron or a free hole can be captured at a dopant site followed by its oppositely charged particle to form an exciton at the dopant site. Another way to create an exciton at a dopant site is for an electron and a hole to form an exciton and then travel together to the dopant site. An exciton at the dopant site has a high probability of de-exciting radiatively. There are also many competing non-radiative decay modes.

Consider a photopeak event in which a gamma-ray photon of energy E undergoes a photoelectric interaction in the scintillation crystal and there is no escape of fluorescent x-rays or other excitations from the crystal. Then the gamma-ray photon deposits its entire energy E in the crystal and produces a random number N of optical photons.

Most scintillators have a nonlinear relationship between the deposited energy and the mean number optical photons emitted (Moses et al., 2012) given by the non-proportionality curves which are graphs of average light yield per unit energy vs. deposited energy. As the initial high-energy electron created from the gamma-ray interaction loses energy, it cascades down this non-proportionality curve. Thus the complete non-proportionality curve below the deposited energy affects the total number of emitted scintillation photons.

The Fano factor of scintillation photons is strongly affected by three competing effects – the statistics of the free electrons and holes created by the cascade of the high-energy electron, the efficiency of converting these free electrons and holes into optical photons, and scintillator non-proportionality.

The cascade of the high-energy electron which yields many free electrons and holes is essentially the same in semiconductors and scintillators. Therefore, as with a semiconductor, the Fano factor of the total number of secondary electrons and holes produced by the high-energy electron cascade in a scintillator should also be sub-Poisson (Moses et al., 2012).

If the efficiency of converting these free electrons and holes into optical photons is very low, then by the law of rare events, the optical photons are emitted independently of each other yielding a Poisson distribution (Falk et al., 2010).

If the non-proportionality curve is flat, then the different cascade paths the high-energy electron takes along the non-proportionality curve will yield the same mean number of scintillation photons. However if the non-proportionality curve varies as a function of electron energy, different cascade paths along the non-proportionality curve yield different mean numbers of scintillation photons. This increases the variance in the number of scintillation photons, increasing the Fano factor.

If the statistics of the electrons and holes produced from the gamma-ray interaction dominate the scintillation photon statistics, the Fano factor of the scintillation photons will be less than one (sub-Poisson).

If the efficiency of conversion from electron and holes to scintillation photons is very low, it will dominate the statistics of the scintillation photons and the Fano factor of the scintillation photons will approach one (Poisson).

If non-proportionality of the scintillator dominates the statistics of the scintillation photons then the Fano factor of the scintillator will be greater than one (super-Poisson).

If the same scintillation pulse is viewed with multiple optical detectors, the Poisson-distributed photons will result in uncorrelated detector outputs, while sub-Poisson distributed photons will result in negatively correlated and super-Poisson distributed photons in positively correlated detector outputs (Barrett and Swindell, 1981; Barrett and Myers, 2004). Using the correlation between two photomultiplier tubes (PMT) Bousselham et. al. (Bousselham et al., 2010) have shown that $LaBr_3$:Ce has a Fano factor less than one. We used the same technique to measure the Fano factors of SrI_2:Eu, CsI:Na and YAP:Ce.

3.2 Theory

3.2.1 Fano factor of optical photons and photoelectrons

Measurement of the Fano factor of scintillation photons is non-trivial because optical photons cannot be directly detected. An optical detector, on average, converts a fraction (η) of the optical photons to photoelectrons. If a random number of optical photons (N) are are produced, then a fraction of optical photons will produce a random number of photoelectrons in an optical detector (n). If we assume that the photoelectrons are produced independently, then the photon-to-photoelectron conversion process can be modeled as a binomial distribution with a probability of success η.

We can define two Fano factors in scintillation detectors – Fano factor of the optical photons F_N and Fano factor of photoelectrons F_n. The relationship between the photon Fano factor and the photoelectron Fano factor is derived below. The mean number of photoelectrons is given by

$$\overline{n} = \sum_{N=0}^{\infty} \sum_{n=0}^{N} n Pr(n|N) Pr(N|\overline{N}). \tag{3.2}$$

For a binomial distribution the inner sum is ηN, so

$$\overline{n} = \sum_{N=0}^{\infty} \eta N Pr(N|\overline{N}) \equiv \eta \overline{N}. \tag{3.3}$$

The variance of the number of photoelectrons is given by

$$\sigma_n^2 = \sum_{N=0}^{\infty} \sum_{n=0}^{N} n^2 Pr(n|N) Pr(N|\overline{N}) - \overline{n}^2. \tag{3.4}$$

The inner sum is the second moment of the binomial distribution, and using Eq. 3.3, we get

$$\sigma_n^2 = \sum_{N=0}^{\infty} (\eta N - \eta^2 N + \eta^2 N^2) Pr(N|\overline{N}) - \eta^2 \overline{N}^2. \tag{3.5}$$

We use $\langle N^2 \rangle = F_N \overline{N} + \overline{N}^2$, to get

$$\sigma_n^2 = \eta \overline{N} - \eta^2 \overline{N} + \eta^2 F_N \overline{N} + \eta^2 \overline{N}^2 - \eta^2 \overline{N}^2. \tag{3.6}$$

$$\sigma_n^2 = \overline{N}\big(\eta + \eta^2 (F_N - 1)\big). \tag{3.7}$$

Dividing both sides by $\overline{n} = \eta\overline{N}$, we get the Fano factor of the photoelectrons as

$$F_n = 1 + \eta(F_N - 1). \tag{3.8}$$

From Eq. 3.8, we see that as $\eta \to 0$, regardless of the value of F_N, $F_n \to 1$. Therefore, if we have low quantum or geometrical efficiency then the photoelectrons Fano factor will tend to 1.

3.2.2 Modeling a two-detector experiment

We use the experimental setup in Fig. 3.1 to estimate the correlation between the signals from two PMTs viewing the same scintillation event. The correlation between the two PMTs is used to estimate the Fano factor of the photoelectrons and the scintillation photons (Bousselham et al., 2010; Barrett and Swindell, 1981; Bora et al., 2011)..

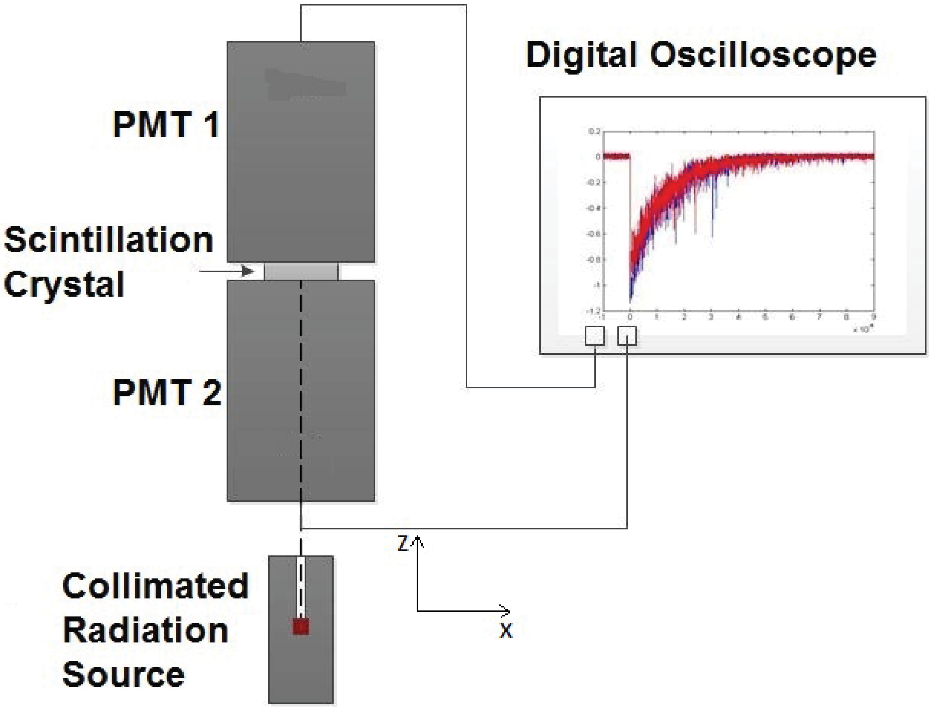

Figure 3.1: Experimental setup to measure the Fano factor from the correlation of signals from two PMTs.

The experiment can be modeled as a trinomial distribution with η_1 the probability of producing a photoelectron in detector 1, η_2 the probability of producing a photoelectron in detector 2, and $(1-\eta_1-\eta_2)$ the probability that the optical photon does not produce a photoelectron in either of the two detectors .

The variance in the number of photoelectrons at the two detectors is given by Eq. 3.7. The covariance in the number of photoelectrons at the two detectors is given by

$$K_{12}^{(n)} = \sum_{N=0}^{\infty}\sum_{n_1=0}^{N}\sum_{n_2=0}^{N}(n_1 - \overline{\overline{n}}_1)(n_2 - \overline{\overline{n}}_2)Pr(n_1, n_2|N)Pr(N|\overline{N}). \quad (3.9)$$

Here $\overline{\overline{n}}_1$, $\overline{\overline{n}}_2$ are the mean number of photoelectrons in detector 1 and detector 2 respectively averaged over both the trinomial probability $Pr(n_1, n_2|N)$ and the probability of N, $Pr(N|\overline{N})$. The mean and variance of the i^{th} outcome of a trinomial distribution are $\eta_i\overline{N}$ and $\eta_i(1-\eta_i)\overline{N}$ respectively. The covariance between the i^{th} and j^{th} outcomes of a trimonial distribution is $-\eta_i\eta_j\overline{N}$. Using these results to simplify Eq. 3.9 we get

$$K_{12}^{(n)} = \sum_{N=0}^{\infty}(\eta_1\eta_2N^2 - \eta_1\eta_2N)Pr(N|\overline{N}) - \eta_1\eta_2\overline{N}^2. \quad (3.10)$$

Simplifying further gives us

$$K_{12}^{(n)} = \eta_1\eta_2\overline{N}(F_N - 1). \quad (3.11)$$

The complete covariance matrix of the number of photoelectrons at the two detectors is given by

$$K^{(n)} = \overline{N}\begin{bmatrix} \eta_1 + \eta_1^2(F_N - 1) & \eta_1\eta_2(F_N - 1) \\ \eta_1\eta_2(F_N - 1) & \eta_2 + \eta_2^2(F_N - 1) \end{bmatrix}. \quad (3.12)$$

To visualize the relationship between Fano factor and the correlation between the two detectors, consider the experimental setup in Fig. 3.1. The detectors are assumed to be identical and noiseless. The output of the experiment is represented as a scatter plot; each point on the plot corresponds to one scintillation event. For each point on the scatter plot, the x coordinate is the proportional to the number of photoelectrons detected by detector 1 and the y coordinate is proportional to the number of photoelectrons detected by detector 2 for the same scintillation event.

If the optical Fano factor is one ($F_N = 1$), then from Eq. 3.11, the two detector outputs have will have zero covariance. As shown in Fig. 3.3, the scatter plot of the photopeak in the Poisson case will be uncorrelated.

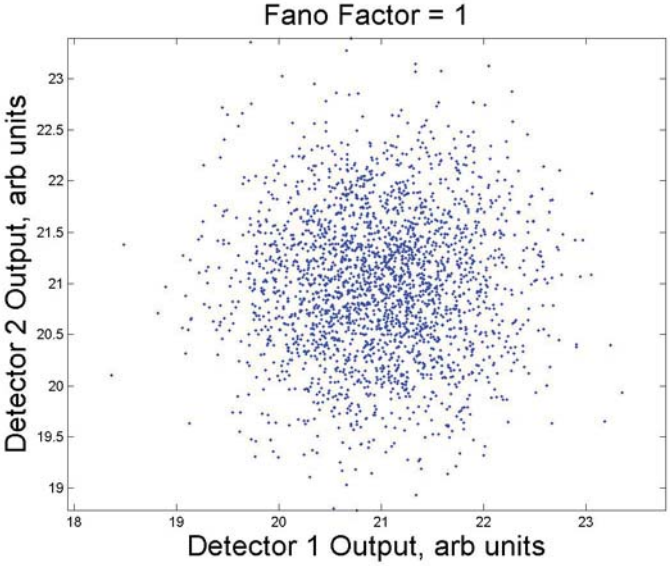

Figure 3.2: Simulated scatter plots of photopeak events for Poisson light ($F_N = 1$). The outputs of the two detectors are uncorrelated.

If the optical Fano factor is less than one ($F_N < 1$), then from Eq. 3.11, the two detector outputs have will have negative covariance. As shown in Fig. 3.2, the scatter plot of the photopeak in the sub-Poisson case will be negatively correlated. If the optical Fano factor is more than one ($F_N > 1$), then from Eq. 3.11, the two detector outputs have will have positive covariance. As shown in Fig. 3.4, the scatter plot of the photopeak in the Poisson case will be positively correlated.

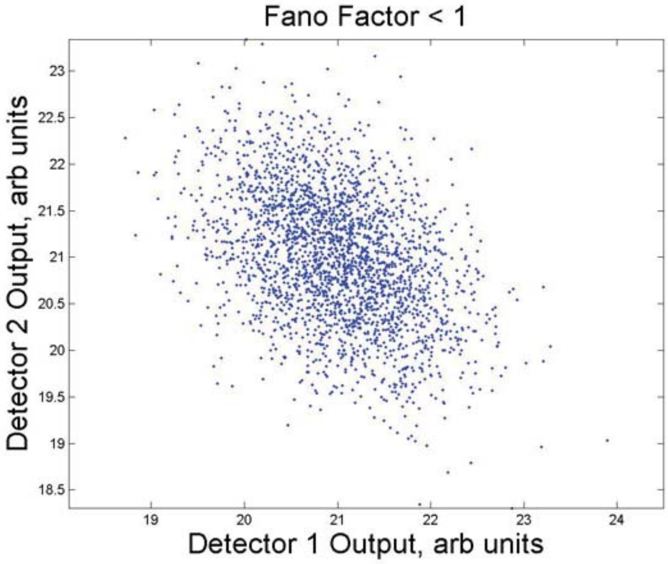

Figure 3.3: Simulated scatter plots of photopeak events for sub-Poisson light ($F_N < 1$). The outputs of the two detectors are negatively correlated.

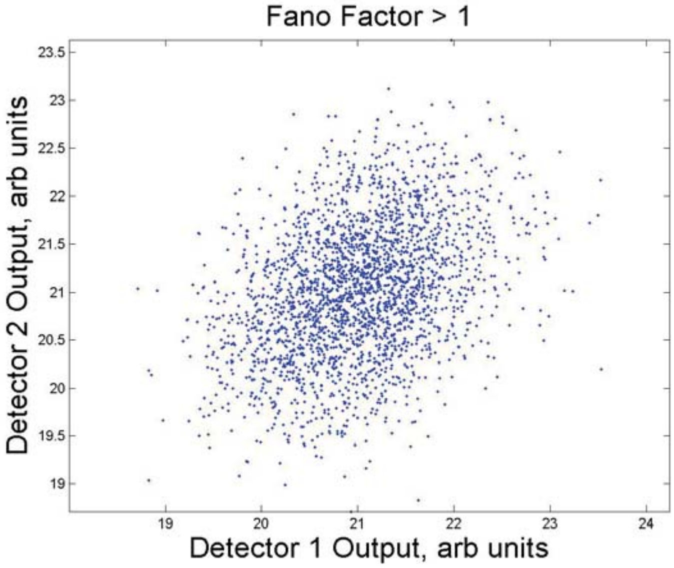

Figure 3.4: Simulated scatter plots of photopeak events for super-Poisson light ($F_N > 1$). The outputs of the two detectors are positively correlated.

3.2.3 Signal processing and PMT gain variance

A photoelectron produced in the photocathode of a PMT is amplified through a number of dynodes before being collected at the anode. Due to this random gain process, a photoelectron at the photocathode produces a random number of electrons at the anode. A scintillation event produces many optical photons, some of which interact at the photocathode of a PMT to produce photoelectrons. The PMT output signal from a scintillation event is the sum of the individual single photoelectron responses.

In our experiment, the PMT output is directly read into a digital oscilloscope which has an input impedance R (usually 50 ohms). The electrons from the anode of the PMT flow through the input impedance of the oscilloscope which records the voltage waveform across it. The total charge on the anode of the PMT can be estimated by dividing this voltage waveform by the input impedance to get the current through the resistor, and then integrating the current. An estimate of the number of photoelectrons, denoted by $\widehat{n}_j$, produced on the j^{th} detector is given by dividing the total charge at the anode by the charge of an electron (e) and the mean gain ($\overline{G}$):

$$\widehat{n}_j = \frac{1}{\overline{G}eR}\int_0^T v_j(t)dt. \tag{3.13}$$

Here v_j is the voltage from the j^{th} PMT, and T is time duration for which we record a scintillation pulse. As the tail of the exponential decay of the scintillation pulse go to zero at infinity, ideally T should be equal to infinity. In practice, we set T to a value greater than or equal to 4 times the decay time constant of the scintillation pulse (τ) to capture more than 98% of the pulse.

As $\overline{G}, R, e$ are constant during an experiment,

$$\widehat{n}_j \propto \int_0^T v_j(t)dt. \tag{3.14}$$

We define the signal from the j^{th} PMT as

$$s_j = \int_0^T v_j(t)dt. \tag{3.15}$$

The gain G_j was converted into the same units of the signals – volts-seconds by multiplying by the charge of an electron and the resistance of the oscilloscope $M_j = G_j eT.$. Therefore, the mean signal is given by $\overline{s}_j = \overline{n}_j \overline{M}_j$, here $(\overline{M}_j = \overline{G}_j eR)$ and the variance of the signal is given by the Burgess variance theorem (Burgess, 1959)

$$Var(s_j) = \overline{n}_j Var(M_j) + \overline{M}_j^2 Var(n_j). \tag{3.16}$$

We define the gain variance coefficient as $\beta = \frac{Var(M_j)}{\overline{M}_j^2}$, and use Eq. 3.8, to get

$$Var(s_j) = \frac{\overline{s}_j^2}{\eta_j \overline{N}}\big(1 + \beta_j + \eta_j(F_N - 1)\big). \tag{3.17}$$

Since the amplification processes for the two detectors are independent, from Eq. 3.11, the covariance between the two detectors is given by

$$Cov(s_1, s_2) = \frac{\overline{s}_1 \overline{s}_2}{\overline{N}}(F_N - 1). \tag{3.18}$$

The covariance matrix of the signals from the two detectors is given by

$$K^{(s)} \quad = \quad \frac{1}{\overline{N}} \begin{bmatrix} \frac{\overline{s}_1^2}{\eta_1}\big(1 + \beta_1 + \eta_1(F_N - 1)\big) & \overline{s}_1 \overline{s}_2 (F_N - 1) \\ \overline{s}_1 \overline{s}_2 (F_N - 1) & \frac{\overline{s}_2^2}{\eta_2}\big(1 + \beta_2 + \eta_2(F_N - 1)\big) \end{bmatrix}. \tag{3.19}$$

$$K^{(s)} = \begin{bmatrix} \overline{G}_1^2 \overline{N} \eta_1 \big(1 + \beta_1 + \eta_1(F_N - 1)\big) & \overline{G}_1 \overline{G}_2 \overline{N} \eta_1 \eta_2 (F_N - 1) \\ \overline{G}_1 \overline{G}_2 \overline{N} \eta_1 \eta_2 (F_N - 1) & \overline{G}_2^2 \overline{N} \eta_2 \big(1 + \beta_2 + \eta_2(F_N - 1)\big) \end{bmatrix}. \tag{3.20}$$

If $\beta_1 = \beta_2$, and $\eta_1 = \eta_2$ the correlation coefficient is given by

$$r_{12} = \frac{k_{12}}{\sqrt{k_{11} k_{22}}} = \frac{\eta(F_N - 1)}{1 + \beta + \eta(F_N - 1)}. \tag{3.21}$$

3.3 Experimental setup

A thin crystal about 10 mm × 10 mm × 1 mm was sandwiched between two Hamamatsu R3998-100-02 PMTs as shown in Fig. 3.1.

The scintillator crystal was coupled to the PMTs by optical grease and mineral oil, or just mineral oil. Hygroscopic crystals were polished with 1500 grit emery paper and, to prevent moisture damage, completely immersed in mineral oil for the duration of the experiment. The assembly was wrapped tightly with black electrical tape to keep out ambient light and placed in a rigid sleeve to prevent the PMTs and the scintillator from shifting during the measurement.

Scintillator crystal and PMT non-uniformities as well as variation in geometrical efficiency for different interaction points make the measurement sensitive to the position of interaction. The uncertainty in the position of interaction increases variance, and results in higher estimates of Fano factors. As shown in Fig. 3.1, by using a collimated Cs-137 (662 KeV) source of 1.3 mm diameter incident at the center of the scintillator we localized the position of interaction in the x-y plane (plane parallel to the detector faces). A thin scintillation crystal was used to minimize variation along the z-axis.

Detecting a high fraction of optical photons is important for the experiment. Equation 3.8 tells us that as η decreases, the photoelectron Fano factor tends to a value of one and becomes less dependent on the photon Fano factor. We define η as the product of geometrical efficiency and quantum efficiency. For a gamma-ray interaction at a given location in the scintillator, the geometrical efficiency of a detector is defined as the fraction of emitted optical photons that are incident on the detector. The quantum efficiency of a detector is the fraction of incident photons that create a photoelectron.

The geometrical efficiency is maximized by using a thin crystal centered and sandwiched between PMT windows bigger than the crystal faces. The centered and collimated source localizes the point of interaction in the scintillation crystal to a small area at the center of the crystal in the x-y plane. At these points of interactions, the two PMTs subtend a solid angle of nearly 2π steradians each. If we assume that the scintillation photons are emitted isotropically, the geometrical efficiencies of the PMTs are very close to 50%. We chose high quantum efficiency super bialkali PMTs which have a maximum quantum efficiency of 35%.

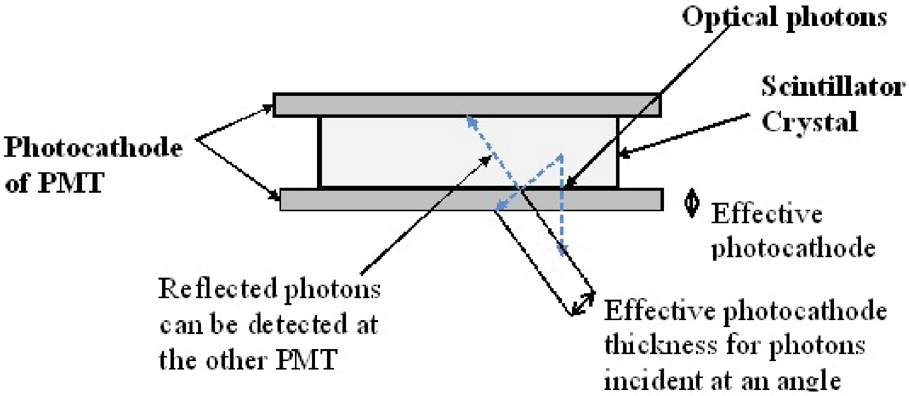

Figure 3.5: Optical photons at higher angles have a larger effective photocathode thickness, and any optical photons reflected at one detector can be absorbed at the second detector.

The quantum-efficiency measurements by the manufacturer are usually made with the incident light normal to the PMT. As shown in Fig. 3.5, optical photons at higher angles of incidence have a larger effective photocathode thickness, increasing their detection probability (Barrett and Swindell, 1981; Tickner and Roach, 2007). However, optical photons at higher angles of incidence also suffer higher reflection losses. These two opposing effects dictate changes in quantum efficiency at different angles of incidence. In our geometry, a photon reflected off one PMT has a high probability of absorption in the other PMT. Hence, in our experiment, η – the light collection efficiency of the PMTs is expected to be higher than the product of the published quantum efficiency and the geometrical efficiency. We assume the value of η to be 0.28. The impact of an error in the estimate of η is discussed later in Sec. 3.5.4.

The gain variance was accounted for in Eq. 3.20 by the gain variance coefficient (β). This parameter was measured by using a pulsed light-emitting diode operating at a low voltage so that the PMT had a high probability of detecting only one photoelectron during each pulse. Signal processing techniques were used to identify the pulses with only one photoelectron, and a histogram of the area under these pulses was plotted to give us the single-photoelectron response. The gain variance coefficient for the PMT was estimated using the width and the mean value of the single-photoelectron response. To simplify calculations, the two PMTs were assumed to be identical with the same quantum efficiency and gain variance coefficient.

3.4 Data analysis and estimation of Fano factor

3.4.1 Data analysis

Twenty to fifty thousand scintillation pulses were recorded and processed as per Sec. 3.2.3 to get signals s_1 and s_2 for each scintillation event. A scatter plot with coordinates (s_1, s_2) was plotted. As shown in Eq. 3.14 and 3.15, s_1 and s_2 are proportional to the estimate for the number of photoelectrons n_1 and n_2 detected on the PMTs respectively. The photopeak events were separated from the Compton events by thresholding just above the Compton edge. The photopeak scatter plot was windowed – along and perpendicular to the $s_1 = s_2$ axis. We used a least-squares approach to fit a similarly windowed 2D Gaussian to the scatter plot (See Fig. 3.6). The Gaussian fit was used to estimate the covariance matrix of the signals.

The experimental measurement is very sensitive to the contact between the scintillator and the detectors and to imperfections in the crystal. To reject experimental artifacts and avoid bias, only measurements with a narrow and symmetric scatter plot of the Compton region (see Fig. 3.8, 3.10 and 3.12) and an energy resolution within a percentage point of the published values were used.

3.4.2 Estimation of Fano factor

We used Eq. 3.8 and 3.21 to get the expression for the estimate of the Fano factor of the photoelectrons as

$$\widehat{F}_n = \left(\frac{1 + \beta\, \widehat{r}_{12}}{1 - \widehat{r}_{12}} \right). \tag{3.22}$$

Equation 3.21 can be rewritten to get an expression for the estimate of the Fano factor of the scintillation photons ($\widehat{F}_N$) in terms of the estimate of the correlation coefficient ($\widehat{r}_{12}$)

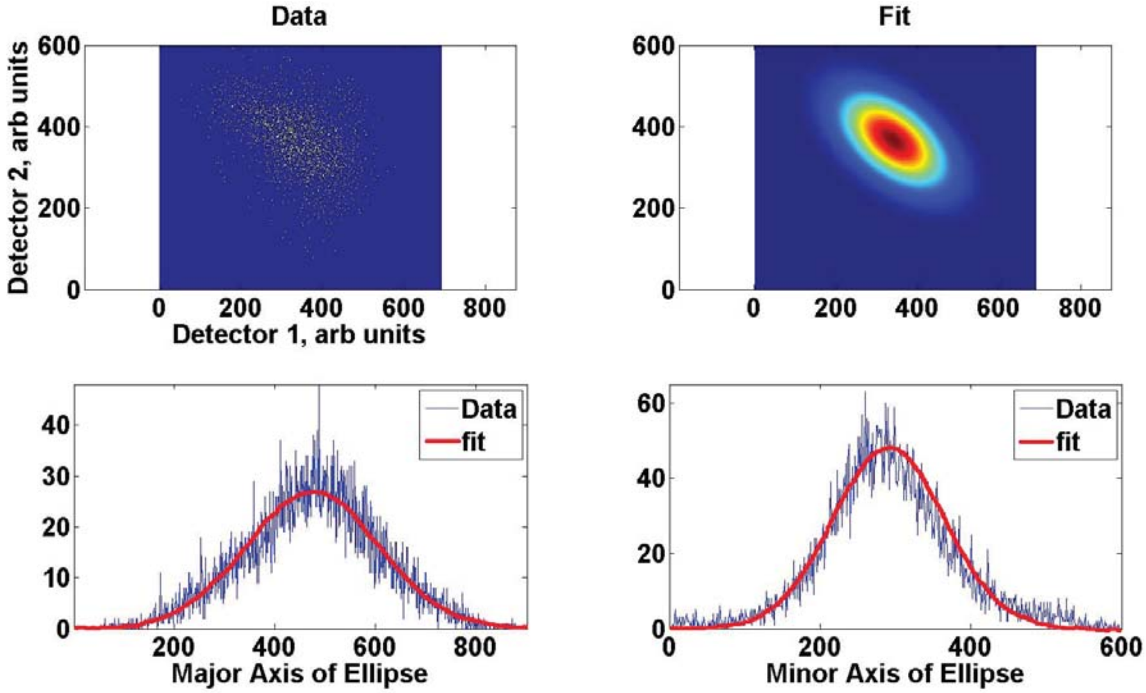

Figure 3.6: The windowed photopeak data from a dataset is on the top left. The windowed Gaussian fit to the data is on the top right. The bottom graphs are sums of sections perpendicular (major axis) and parallel (minor axis) to the $s_1 = s_2$ line.

$$\widehat{F}_N = 1 + \left(\frac{\widehat{r}_{12}}{1-\widehat{r}_{12}}\right)\left(\frac{1+\beta}{\eta}\right). \tag{3.23}$$

3.5 Results

3.5.1 SrI$_2$:Eu

SrI$_2$:Eu has high light output (≈100,000 photons / MeV) and excellent published energy resolution of 3% (van Loef et al., June 2009) at 662 KeV. The energy resolutions in our measurements varied from 3.3%-3.5%. See Fig. 3.7.

In Fig. 3.7, the smooth falloff at low energies in the Compton region of the energy spectrum is because the events were triggered on the pulse amplitude, but the histogram is of the integral of the pulse.

We made twelve measurements on two samples of SrI$_2$:Eu that met the accep-

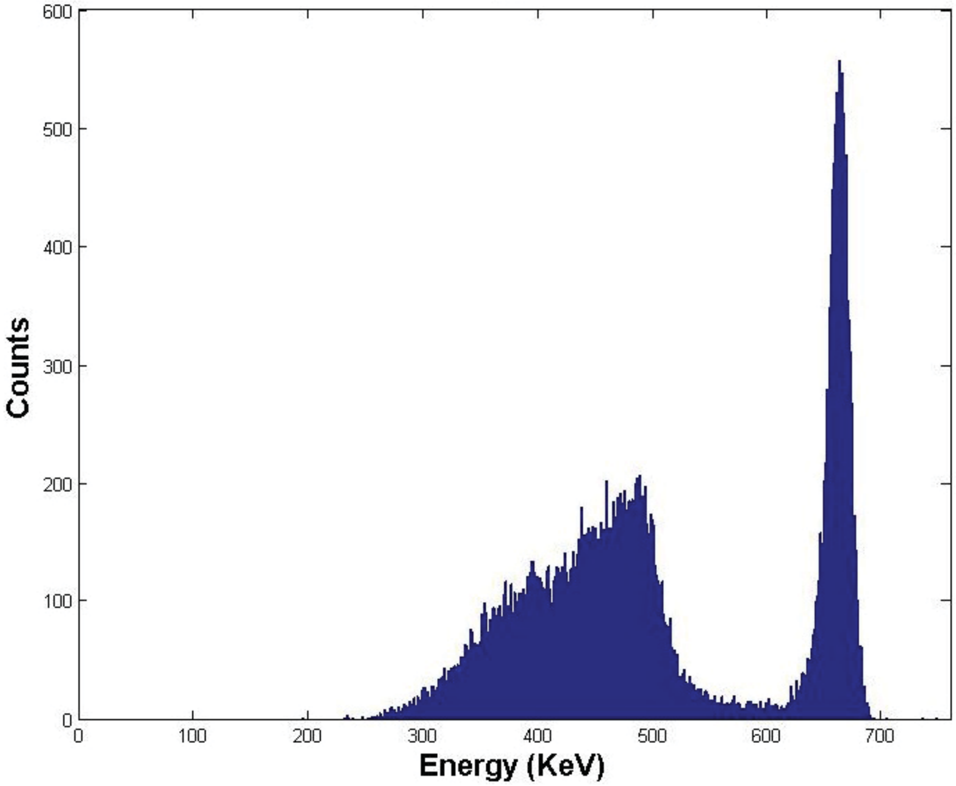

Figure 3.7: Energy spectrum of SrI_2:Eu. The plot is made by summing the outputs of both the PMTs. The narrow photopeak indicates good energy resolution.

tance criteria described in Sec. 3.4.1 and were used for estimating Fano factors. We found the integral of the detector outputs to be negatively correlated, and therefore, concluded that SrI_2:Eu has sub-Poisson scintillation light at 662 KeV gamma-ray interactions.

3.5.2 YAP:Ce

The chemical formula for YAP is $YAlO_3$. YAP:Ce has a low light output (18,000 photons/MeV), but has good published energy resolution of 4.4% (Kapusta et al., 1999) at 662 KeV. Our measured energy resolutions (see Fig. 3.9) varied from 3.47% to 4.42%.

We had only one sample of YAP:Ce, and we made eight measurements that met the acceptance criteria described in Sec. 3.4.1 for estimating Fano factor. We found

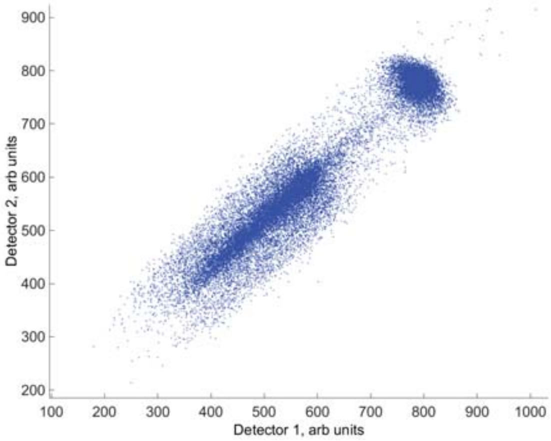

Figure 3.8: Scatter plot for SrI_2:Eu. The negative correlation between the two PMTs can be seen in the photopeak region.

the integral of the detector outputs to be slightly positively correlated, and therefore, concluded that YAP:Ce's scintillation light at 662 KeV gamma-ray interactions is either super-Poisson or close to Poisson.

3.5.3 CsI:Na

CsI:Na has good light output (43,000 photons/MeV) but relatively poor published energy resolution of 7.07% at 662 KeV (Sakai, 1987). Another study has reported an energy resolution of 5.8% with longer than usual shaping time of 12 μs (Syntfeld-Kazuch et al., 2009). We had two samples of CsI:Na and we made ten measurements that met the acceptance criteria described in Sec. 3.4.1 for estimating Fano factor. Eight of our measurements captured pulses for 4 μs while two measurements integrated for 10 μs. The energy resolutions in our measurements varied between 4.6%-6.7%.

We found positive correlation between the integrals of the signals from the two PMTs and found the scintillation light from CsI:Na at 662 KeV gamma-ray energy to be super-Poisson. The high positive correlation in CsI:Na is a result of varying energy distribution between the primary radiatively decay processes and the mil-

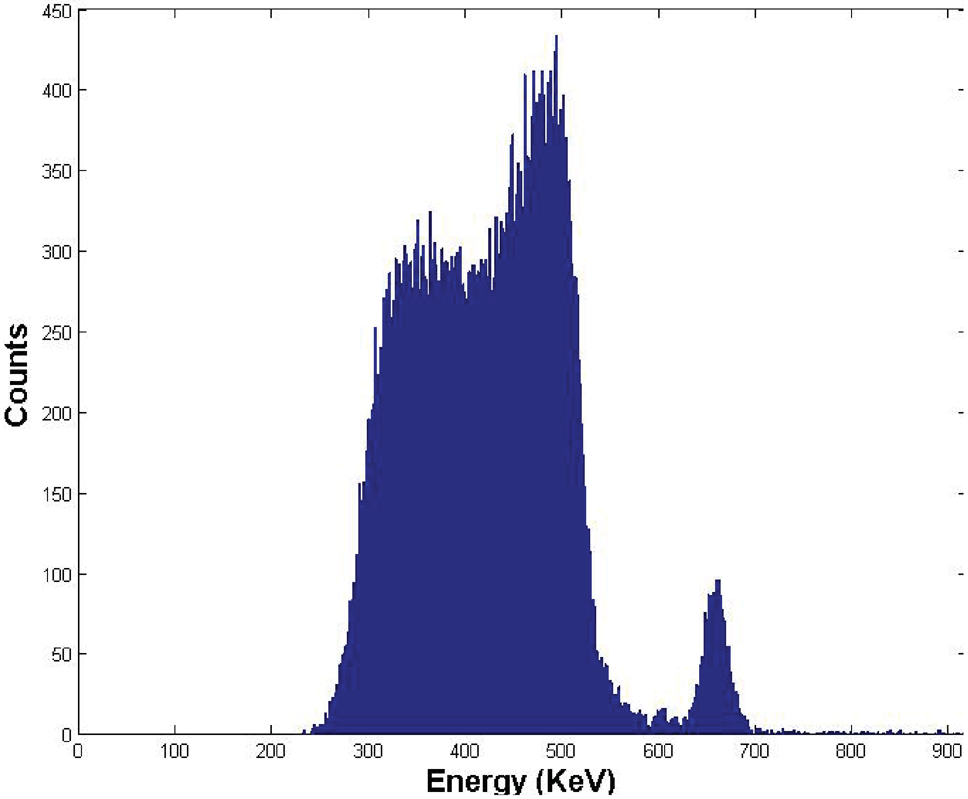

Figure 3.9: Energy spectrum of YAP:Ce. The plot is made by summing the outputs of both the PMTs. The energy resolution of the YAP:Ce is not as good as the energy resolution of SrI_2:Eu.

lisecond afterglow process. Integrating the CsI:Na signals for longer durations to capture all the afterglow could result in smaller estimates of Fano factor.

3.5.4 Fano factor estimates

Using the experiment and the estimation process described above, we estimated the correlation coefficient between the two detector outputs. We then used estimates of the correlation coefficient, and equations 3.22 and 3.23 to estimate the Fano factor of the photoelectrons and the scintillation photons.

Table 3.1 shows the estimates of the photoelectron and scintillation photons Fano factor for $\beta = 0.07$ and $\eta = 0.28$. The uncertainty in estimation of correlation coefficient was propagated to estimate the uncertainty in the estimates of F_n and

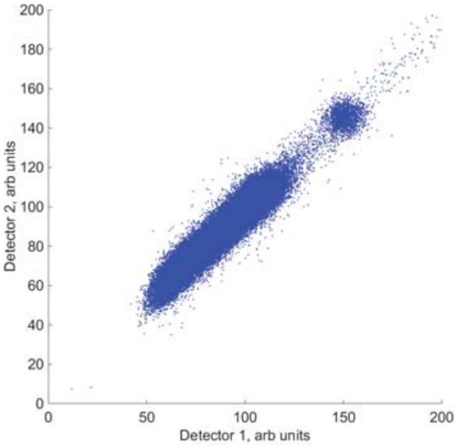

Figure 3.10: Scatter plot for YAP:Ce. The photopeak of the scatter plot has little or no correlation.

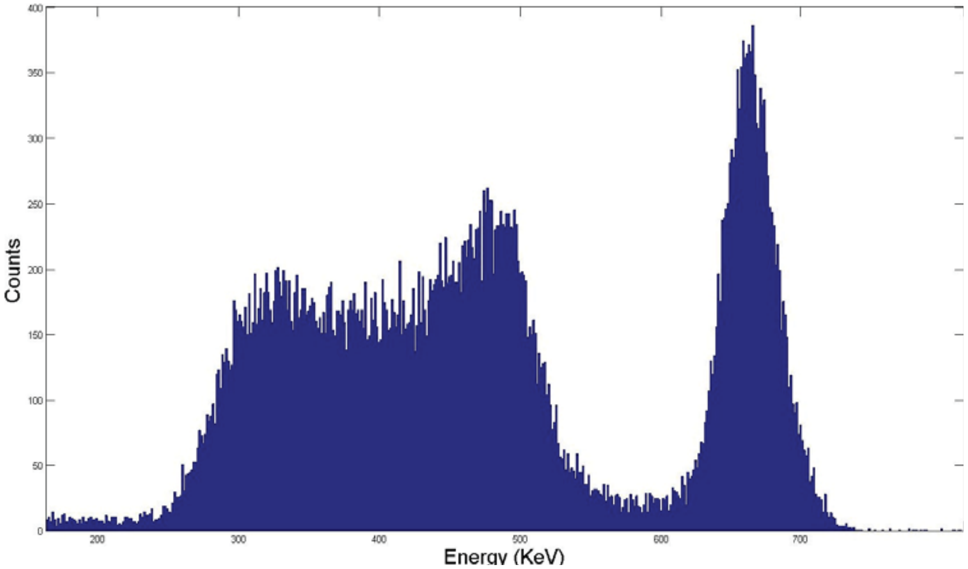

Figure 3.11: Energy spectrum of CsI:Na.The plot is made by summing the outputs of both the PMTs. The energy resolution of the photopeak is broader than YAP:Ce or SrI_2:Eu

F_N. Both η and β are parameters of the PMT that do not change in a measurement. Hence they do not add to uncertainty, but introduce bias in the Fano factor estimates. The estimates of correlation coefficient of $LaBr_3$:Ce are reproduced here

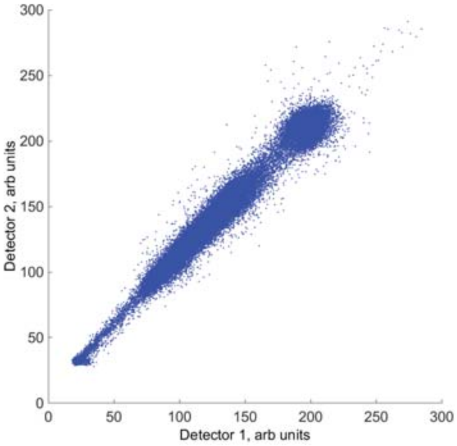

Figure 3.12: Scatter plot for CsI:Na, the photopeak is positively correlated.

from (Bousselham et al., 2010).

Table 3.1: Photoelectron and Photon Fano factor Estimates $\beta = 0.07$ and $\eta = 0.28$. The results for $LaBr_3$:Ce are reproduced from (Bousselham et al., 2010).

	Correlation Coefficient (r_{12})	Photoelectron Fano factor (F_n)	Photon Fano factor (F_N)
SrI_2:Eu	-0.3134 ±0.039	0.7526 ±0.024	0.1165 ±0.11
YAP:Ce	0.1036 ±0.024	1.13 ±0.033	1.464 ±0.13
CsI:Na	0.4192 ±0.066	1.949 ±0.18	4.391 ±0.68
$LaBr_3$:Ce	-0.32 ± 0.17	0.7333 ± 0.11	0.01235 ± 0.40

To test the impact of an error in our estimate of β on the Fano factor estimates, we calculated the mean and standard deviation of the estimates of photoelectron and photon Fano factor for different values of β at $\eta = 0.28$. From Table 3.2, we conclude that the gain variance coefficient (β) does not have a large impact on the estimates of the photoelectron or the photon Fano factor.

The value of the photoelectron Fano factor is independent of the estimate of η (See Eq. 3.22). To test the impact of an error in our estimate of η on the photon Fano factor estimates, the photon Fano factor for different values of η at $\beta = 0.07$ are shown in Table 3.3. An error in the estimate of η has a significant impact on the estimates of the photon Fano factors. A small value of η biases the Fano factor estimates away from one – the estimates of the Fano factor of sub-Poisson scintillators become more sub-Poisson and the estimates of the Fano factor of super-Poisson scintillators become more super-Poisson. A smaller value of η also increases the uncertainty in the measurement for all the scintillators. The values of η below 0.24 result in unphysical negative estimates of photon Fano factor for SrI_2:Eu.

Table 3.2: Photoelectron and photon Fano factor estimates for different values of β with $\eta = 0.28$

	Photoelectron Fano factor (F_n)			Photon Fano factor (F_N)		
Gain Noise Factor (β)	SrI_2:Eu	YAP	CsI:Na	SrI_2:Eu	YAP	CsI:Na
0.05	0.7572 ±0.024	1.128 ±0.033	1.932 ±0.18	0.133 ±0.11	1.456 ±0.12	4.327 ±0.67
0.06	0.7549 ±0.024	1.129 ±0.033	1.941 ±0.18	0.1248 ±0.11	1.46 ±0.12	4.359 ±0.68
0.07	0.7526 ±0.024	1.13 ±0.033	1.949 ±0.18	0.1165 ±0.11	1.464 ±0.13	4.391 ±0.68
0.08	0.7503 ±0.025	1.131 ±0.034	1.958 ±0.18	0.1083 ±0.11	1.469 ±0.13	4.422 ±0.69
0.09	0.748 ±0.025	1.132 ±0.034	1.967 ±0.18	0.1 ±0.11	1.473 ±0.13	4.454 ±0.7

Table 3.3: Photon Fano factor estimates for different values of η with $\beta = 0.07$

	Photon Fano factor (F_N)		
(η)	SrI_2:Eu	YAP	CsI:Na
0.2	-0.2369 ±0.18	1.65 ±0.18	5.747 ±1
0.22	-0.1244 ±0.16	1.591 ±0.16	5.316 ±0.9
0.24	-0.03073 ±0.14	1.542 ±0.15	4.956 ±0.81
0.26	0.04855 ±0.12	1.5 ±0.14	4.652 ±0.74
0.28	0.1165 ±0.11	1.464 ±0.13	4.391 ±0.68
0.3	0.1754 ±0.1	1.433 ±0.12	4.165 ±0.63
0.32	0.227 ±0.093	1.406 ±0.11	3.967 ±0.59
0.34	0.2724 ±0.086	1.382 ±0.1	3.792 ±0.55
0.36	0.3128 ±0.08	1.361 ±0.096	3.637 ±0.52

3.6 Conclusion

The Fano factors of scintillation photons and photoelectrons were estimated using the correlation of signals from two optical detectors viewing the same scintillation event. We found the detector outputs from CsI:Na to be positively correlated, while the detector outputs of SrI_2:Eu to be negatively correlated. The detector outputs from YAP:Ce were very close to uncorrelated.

We modeled the process of generation, detection and amplification of scintillation photons and derived an expression for the Fano factor as a function of the correlation coefficient of the two detector outputs. We found that CsI:Na is super-Poisson, SrI_2:Eu is sub-Poisson and YAP:Ce is close to Poisson.

CHAPTER 4

Time Statistics in Scintillation Crystals

4.1 Introduction

Counting statistics and the Fano factor are defined on the total number of photons emitted or detected. In the previous chapter, we used two detectors simultaneously looking at the same scintillation pulse. We estimated the total number of detected photons (or photoelectrons) by integrating the detector signal for the duration of the scintillation pulse, and then using the correlation coefficient of the integrated signal to estimate the Fano factor of the photoelectrons and the photons. In this chapter, we investigate if we can use a similar geometry as before and estimate the Fano factor of scintillation photons from time correlations between the two detector outputs.

Previous literature to estimate the Fano factor from time correlations primarily focused on stationary processes. Our attempts to derive similar analytical results for non-stationary process were not successful, so we made a statistical model of the emission and detection of scintillation light as a function of Fano factor.

The emission of scintillation photons is a point process, and the inter-event time of the scintillation point process was modeled as a gamma distribution. We found an analytical relationship between the gamma distribution parameters and the Fano factor for a renewal process (see Sec. 4.2.6). A renewal process, by definition is stationary. As the mean rate of the scintillation process changes with time, a scintillation process is not stationary. However, results from Monte-Carlo simulations in Sec. 4.2.7 indicated that the results from renewal theory relating the parameters of the gamma-distribution and the Fano factor are valid for the non-stationary scintillation process too.

The detection, random amplification, and time-response characteristics of PMTs were also modeled to generate simulated detector outputs for different values of gamma-distribution parameters, and find a relationship between the detector outputs and the gamma-distribution parameters.

Therefore, there are two parts in the statistical model to estimate the Fano factor – 1) A model for the relationship between the detector outputs and the gamma-distribution parameters, and 2) a model for the relationship between the gamma-distribution parameters and the Fano factor.

4.2 Theory

The classical or wave theory of light treats light as a complex signal $V(\vec{r}, t)$, whose squared absolute value $I(\vec{r}, t) = |V(\vec{r}, t)|^2$ is the irradiance (Born and Wolf, 1999). The classical theory restricts the Fano factor to values greater than one. The quantum theory of light recognizes the wave-particle duality of light and allows for Fano factors less than one. Therefore, light with Fano factor less than one is often referred to as "non-classical" light.

In the next sub-sections we will define point processes, renewal processes, gamma distributions, and make a statistical model using all these concepts. We will also relate the covariance, correlation and coherence to these models.

4.2.1 Point process

A point process is defined as a random process for which a realization consists of a set of isolated points in some space. Thus, a realization of a point process can be described as a set of delta functions in the dimensions of that space. A point process in time has one-dimensional delta functions and is called a temporal point process. A point process in space and time has delta functions in four dimensions (x, y, z, t) and is called a spatiotemporal point process (Barrett and Myers, 2004).

The scintillation process is a stochastic point process in time, producing a random number (N) of scintillation photons at random times $t_1, t_2 \ldots t_N$. In this chapter, we study, model and measure the time correlations in the scintillation light from different scintillator materials.

4.2.2 Renewal process

A renewal process is a continuous-time Markov process on positive integers in which the inter-event times are independent and identically distributed. Therefore, a renewal process is by definition, a stationary process (Parzen, 1962).

4.2.3 Classification of point processes

Based on the time spacing between successive points, a temporal point process can be classified as bunched, Poisson, or anti-bunched (Teich et al., 1988).

In a Poisson Point Process (PPP), the occurrence of an event does not increase or decrease the probability of the occurrence of next event. All the events are independent of each other and completely random. In a bunched point process, the events are less uniformly spaced as compared to the PPP, while in an anti-bunched point process, the events are more uniformly spaced than a PPP (See Fig. 4.1).

4.2.4 Inter-event time for a Poisson point process

The Poisson distribution is used to describe the probability of counting N events in between times 0 and t. If the underlying Poisson point process has a mean arrival rate of λ counts per unit time then the mean number of events will be $\overline{N} = \lambda t$ and the probability of N events occurring between times 0 and t is given by

$$Pr(N|\lambda t) = (\lambda t)^N \frac{e^{-\lambda t}}{N!}. \tag{4.1}$$

The probability distribution function (PDF) of the time between two successive events ($pr(\Delta t|\lambda)$) for a PPP with a mean rate of λ events per second is derived below. The cumulative distribution function (CDF) of the inter-event time, $F(\Delta t|\lambda)$, can be written in terms of the probability of detecting zero events from 0 to Δt

$$F_{\Delta t}(t|\lambda) = pr(\Delta t \leq t|\lambda) = 1 - pr(\Delta t > t|\lambda) = 1 - Pr(N = 0|\lambda t). \tag{4.2}$$

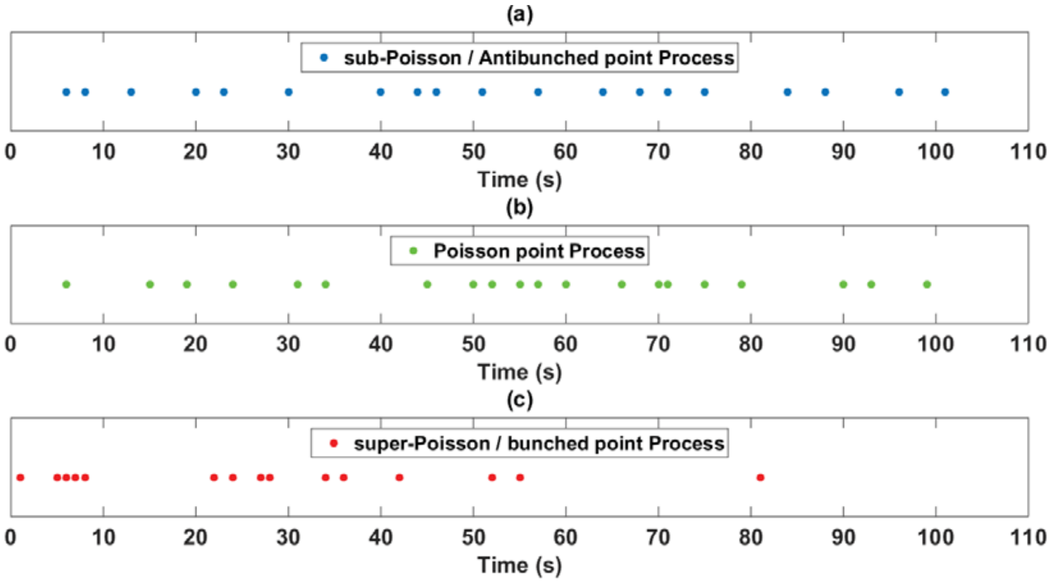

Figure 4.1: The realization of a Poisson point process in (b) has randomly spaced points. The realization of an anti-bunched point process in (a) is more evenly spaced as compared to the Poisson point process. The realization of the bunched point process (c) is less evenly spaced as compared to the Poisson point process.

Here, $Pr(N = 0|\lambda t)$ is the probability of no events occurring between 0 and t. Writing the expression for the Poisson distribution with $N = 0$ gives us

$$F_{\Delta t}(t|\lambda) = 1 - (\lambda t)^0 \frac{e^{-\lambda t}}{0!} = 1 - e^{-\lambda t}. \tag{4.3}$$

We take the derivative of the CDF $F_{\Delta t}(t|\lambda)$ to get the PDF $pr(\Delta t|\lambda)$ as shown below

$$pr(\Delta t|\lambda) = \lambda e^{-\lambda \Delta t}. \tag{4.4}$$

The inter-event time of a Poisson point process is exponentially distributed (Teich et al., 1988). The complete PDF of an exponentially distributed inter-event time with mean λ is given as

$$pr(\Delta t|\lambda) = \begin{cases} \lambda e^{-\lambda \Delta t}, & \Delta t \geq 0 \\ 0, & \Delta t < 0. \end{cases} \tag{4.5}$$

4.2.5 Modeling the inter-event time as a gamma distribution

The inter-event time of a generic point process is often modeled as a gamma distribution (Parzen, 1962). The gamma distribution is a two-parameter continuous distribution and can be used to model bunched, Poisson and anti-bunched events. The exponential distribution used to model the inter-event time in the PPP is a special case of the gamma distribution. The gamma distribution given by

$$pr(\Delta t|k,\theta) = \begin{cases} \frac{1}{\Gamma(k)\theta^k}(\Delta t)^{k-1}e^{(-\Delta t/\theta)}, & \Delta t \geq 0 \\ 0, & \Delta t < 0. \end{cases} \tag{4.6}$$

Here, k is the shape factor, θ is the scale factor, $\Gamma(k)$ is the gamma function evaluated at k. The mean and variance of the gamma distribution are given by $\overline{\Delta t} = k\theta$ and $\sigma^2_{\Delta t} = k\theta^2$ respectively. The coefficient of variation c, a quantity analogous the Fano factor, is defined as the ratio of the standard deviation of the inter-event time to the mean inter-event time.

$$c = \frac{\sigma_{\Delta t}}{\overline{\Delta t}} = \frac{1}{\sqrt{k}}. \tag{4.7}$$

For a Poisson point process with exponentially distributed inter-event times, the standard deviation of the inter-event times is equal to the mean inter-event time ($\sigma_{\Delta t} = \overline{\Delta t}$), giving us $k = c = 1$. When $c > 1$, then $k < 1$ and the standard deviation of the inter-event times is greater than the standard deviation of a PPP with the same mean. This implies that the events are more "bunched" than in the PPP. For $c < 1, k > 1$, the standard deviation of the inter-event time is less than the standard deviation of a PPP with the same mean. This implies that the events are more uniformly spaced than the PPP. Such events are also called anti-bunched events (Teich et al., 1988; Saleh, 1977).

The PDF of gamma distributions for the same mean but different values of shape factor are given in Fig. 4.2 . Figure 4.3 shows the zoomed-in tail section of Fig. 4.2 to show that the PDF of the bunched and anti-bunched events again cross the PDF of the exponential curve for large values of inter-event time.

The anti-bunched inter-event PDF rises from zero, and crosses the exponential PDF for the PPP, and then in the tail region drops again to a value below the exponential PDF for the PPP. This indicates that compared to Poisson events, anti-bunched events are more likely to occur in the middle range of the inter-event times and less likely to occur at the smaller and the larger inter-event times. Therefore, anti-bunched events are more uniformly spaced than Poisson events. The bunched events have the opposite behavior, they have a higher probability than the PPP events at small inter-event times and at large inter-event times, but have a lower probability of occurring in the middle ranges of the inter-event times. Therefore, bunched events are less uniformly spaced than the Poisson events.

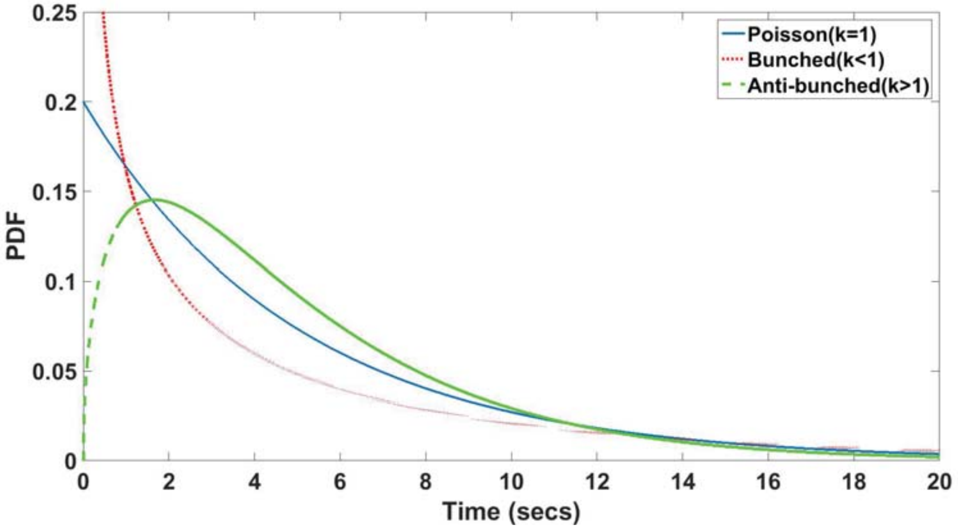

Figure 4.2: The PDF for bunched events is greater than the Poisson distribution PDF for small and large inter-event times. So the events are more likely to bunch together. Anti-bunched events follow the opposite trend to bunched events and are more regularly spaced than Poisson events.

4.2.6 Relationship between shape factor and Fano factor for a stationary point process

The shape factor of the gamma distribution is defined on the statistics of the inter-event time, while the Fano factor is defined on the statistics of the number of events

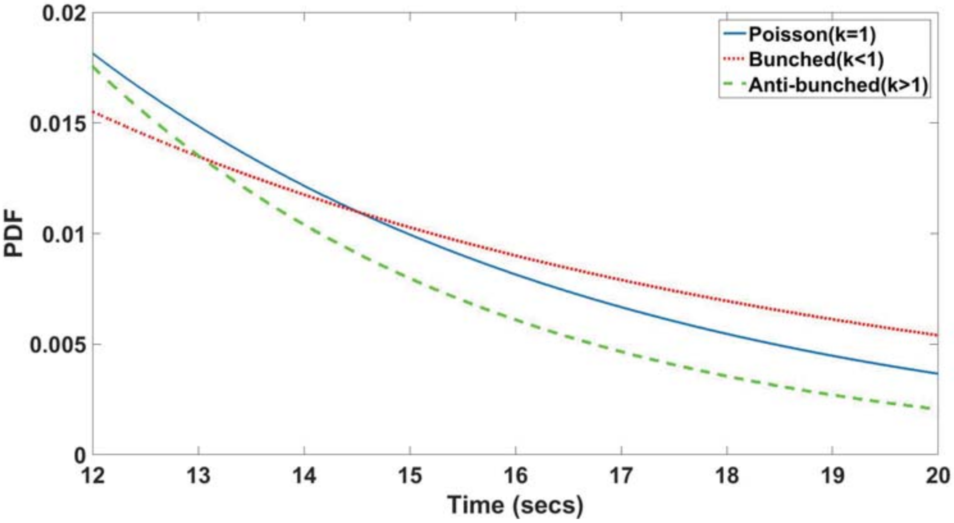

Figure 4.3: The tail portion of the PDF for bunched, Poisson and anti-bunched events shown in Fig. 4.2 is shown above. The PDF of the bunched, and anti-bunched events cross the Poisson PDF in this region from opposite sides.

in a given time. The properties of the renewal process were used to derive the relationship between the shape factor and the Fano factor (Parzen, 1962; Taylor and Karlin, 1998)

$$F = \frac{1}{k}. \tag{4.8}$$

We modeled the inter-event times $(\Delta t_1, \Delta t_2, \cdots \Delta t_N)$ between successive points of our point process as a gamma distribution. Thus, our point process is a renewal process with gamma-distributed inter-event times. As the mean emission rate of photons is not constant in a scintillation pulse, the scintillation process is by definition, non-stationary. In Sec. 4.2.7, we investigate whether the relationship between the Fano factor and the shape factor for a renewal process (by definition a stationary process) given by Eq. 4.8 is also valid for scintillation light.

4.2.7 Relationship between shape factor and Fano factor for a non-stationary point process

The inter-event arrival time in a scintillation process was modeled as a gamma distribution with a constant shape factor k, and a scale factor θ that varies as the pulse decays. We performed a Monte-Carlo simulation to find the relationship between the Fano factor and the shape factor for a non-stationary process.

We simulated 5000 scintillation pulses with gamma-distributed inter-event times with a constant shape factor and varying scale factor. The total number of events (N_{sim}) recorded during the acquisition time were used to estimate the Fano factor of the events generated with a given shape factor.

$$\hat{F}_{sim} = \frac{var(N_{sim})}{\overline{N_{sim}}}. \tag{4.9}$$

The estimates of the Fano factor from the simulation of scintillation light and the Fano factor calculated from the shape factor using the renewal theory equation in Eq. 4.8 were found to be consistent with each other (see Fig. 4.5). Therefore, the shape factor can be used to estimate the Fano factor of the scintillation light.

4.2.8 Correlation, covariance and coherence

The correlation function of the optical fields for two space-time points $(\vec{r}_1, t_1)$ and $(\vec{r}_2, t_2)$ is given as

$$G^{(1)}(\vec{r}_1, t_1, \vec{r}_2, t_2) = \Big\langle V^*(\vec{r}_1, t_1) V(\vec{r}_2.t_2) \Big\rangle. \tag{4.10}$$

Here, $V(\vec{r}_1, t_1)$ is the complex field at position $\vec{r}_1$ and time t_1. The angle brackets indicate an ensemble average. Detectors cannot directly measure the field V, but respond to the irradiance which is the square modulus of the field, often referred to as intensity ($I = |V|^2$). The second-order correlation function, also known as the intensity correlation is given by

$$G^{(2)}(\vec{r}_1, t_1, \vec{r}_2, t_2) = \Big\langle I(\vec{r}_1, t_1) I(\vec{r}_2.t_2) \Big\rangle. \tag{4.11}$$

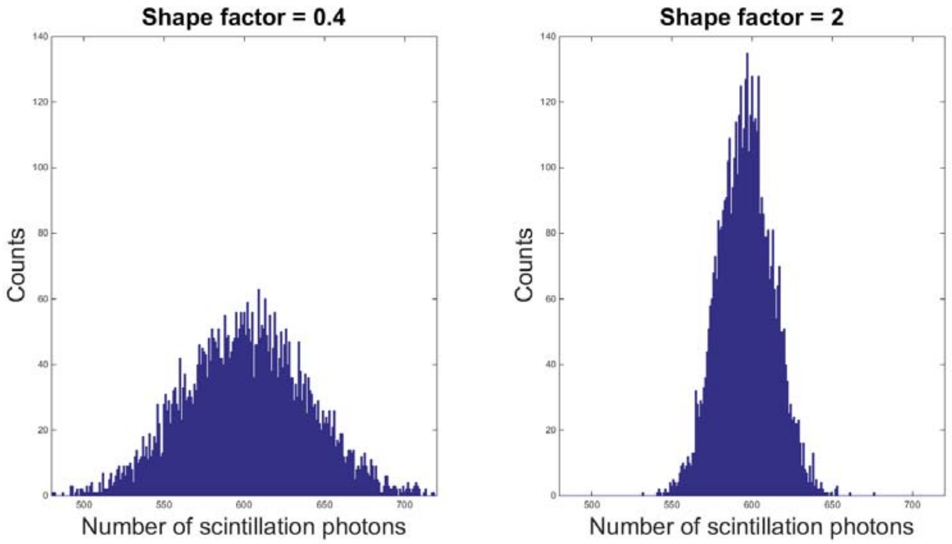

Figure 4.4: Five thousand gamma-ray interactions were simulated using Monte-Carlo simulations of a point process with gamma-distributed inter-event times, a constant shape factor, and changing scale factor. The histograms of the number of scintillation photons for the simulated pulses for shape factors of 0.4 and 2 are shown above.

Temporal covariance compares the detector signals to their means. The intensity cross-covariance $cov\big(\vec{r}_1, t_1, \vec{r}_2.t_2\big)$ is calculated by subtracting by the average intensity and then averaging over the ensemble as given below

$$cov\big(\vec{r}_1, t_1, \vec{r}_2, t_2\big) = \Big\langle \big[I(\vec{r}_1, t_1) - \overline{I}(\vec{r}_1, t_1)\big]\big[I(\vec{r}_2.t_2) - \overline{I}(\vec{r}_2.t_2)\big] \Big\rangle. \tag{4.12}$$

The relationship between bunching or anti-bunching of events and their cross-covariance can be visualized with the following example. We measure the intensity of the field using two detectors at positions, $\vec{r_1}$ and $\vec{r_2}$ at time, $t_1 = t_2 = t$. At a given time t, if both the two detector signals are more likely to be either above or below their mean values, then their cross-covariance curve is positive. Similarly, if the two detector signals are more likely to be on opposite sides of their mean values, then the cross-correlation will be negative. If the two signals are independent of each other, then the cross-covariance curve will be zero.

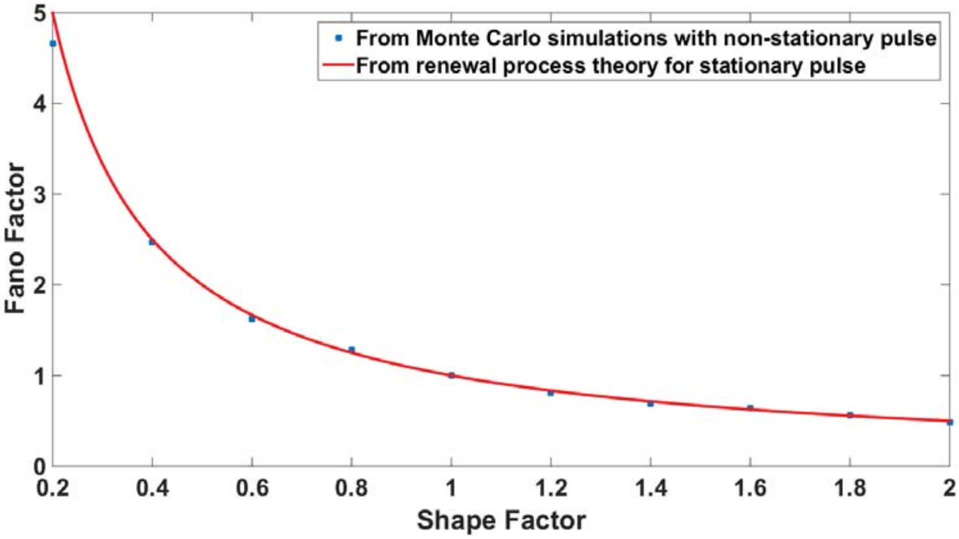

Figure 4.5: Estimate of the Fano factor from Monte-Carlo simulations of a point process with gamma-distributed inter-event times with a constant shape factor, and changing scale factor. The Fano factor estimated using renewal theory (see Eq. 4.8) and the Fano factor estimated from the Monte-Carlo simulation are in agreement with each other.

The uncertainty or randomness in the emission and detection of scintillation photons is averaged out in the mean signal. Therefore, the mean signal is a smooth function in time and independent of the coefficient of variation defined in Eq. 4.7. Consider a bunched point process; when a bunch of events is emitted, both detectors record signals that are likely to be larger than their mean. Similarly, in the time between two bunches, when a few or no events arrive, both the detectors record a signal that is likely to be smaller than their means. Therefore, a bunched process will yield a positive cross-covariance curve. Conversely, an anti-bunched point process will yield a negative cross-covariance curve and a Poisson point process will yield zero cross-covariance curve. Therefore, the cross-covariance curve is expected to be negative for Fano factors less than one, positive for Fano factors greater than one and zero for a Fano factor of one.

The normalized correlation function, also known as second order coherence, is given by normalizing the correlation function with the mean intensities as given below

$$g^{(2)}(\vec{r}_1, t_1, \vec{r}_2, t_2) = \frac{G^{(2)}(\vec{r}_1, t_1, \vec{r}_2, t_2)}{\Big\langle I(\vec{r}_1, t_1)\Big\rangle\Big\langle I(\vec{r}_2.t_2)\Big\rangle} = \frac{\Big\langle I(\vec{r}_1, t_1)I(\vec{r}_2.t_2)\Big\rangle}{\Big\langle I(\vec{r}_1, t_1)\Big\rangle\Big\langle I(\vec{r}_2.t_2)\Big\rangle}. \tag{4.13}$$

The normalized cross-covariance function, is given by

$$\sigma(\vec{r}_1, t_1, \vec{r}_2, t_2) = \frac{cov\big(\vec{r}_1, t_1, \vec{r}_2, t_2\big)}{\Big\langle I(\vec{r}_1, t_1)\Big\rangle\Big\langle I(\vec{r}_2.t_2)\Big\rangle} = \frac{\Big\langle \big[I(\vec{r}_1, t_1) - \overline{I}(\vec{r}_1, t_1)\big]\big[I(\vec{r}_2.t_2) - \overline{I}(\vec{r}_2.t_2)\big]\Big\rangle}{\Big\langle I(\vec{r}_1, t_1)\Big\rangle\Big\langle I(\vec{r}_2.t_2)\Big\rangle}. \tag{4.14}$$

Straightforward mathematics gives us the relationship between normalized cross-covariance $\sigma\big(\vec{r}_1, t_1, \vec{r}_2, t_2\big)$ and second-order coherence $g^{(2)}(\vec{r}_1, t_1, \vec{r}_2, t_2)$ as

$$\sigma(\vec{r}_1, t_1, \vec{r}_2, t_2) = g^{(2)}(\vec{r}_1, t_1, \vec{r}_2, t_2) - 1. \tag{4.15}$$

The second-order coherence function defined in Eq. 4.13 was historically used with light with stationary statistics. As scintillation light is not stationary (the mean intensity varies as a function of time), we cannot directly use the second-order coherence function for scintillation light. In addition, as the scintillation pulse decays with time, the mean signals become very small making the denominator of the normalized cross-covariance function close to zero. To avoid dividing by small numbers, we integrate the numerator and the denominators of Eq. 4.14 for the duration of pulse and calculate the Normalized Area Under the Cross-Covariance Curve (AUCCC). In the equation below, we have substituted $t_1 = t, t_2 = t + \tau$. Unless explicitly specified, in the next sections we have used the normalized AUCCC with $\tau = 0$.

$$\text{Norm AUCCC} == \frac{\int\limits_{t=0}^{T} \Big\langle \big[I(\vec{r}_1, t) - \overline{I}(\vec{r}_1, t)\big]\big[I(\vec{r}_2, t+\tau) - \overline{I}(\vec{r}_2, t+\tau)\big]\Big\rangle dt}{\int\limits_{t=0}^{T} \Big\langle I(\vec{r}_1, t)\Big\rangle\Big\langle I(\vec{r}_2, t+\tau)\Big\rangle dt}. \tag{4.16}$$

4.3 Implementation

4.3.1 Simulation

We performed Monte-Carlo simulations with the model described below to find an empirical relationship between the Fano factor of the scintillation photons and the normalized AUCCC of the PMT signals. .

4.3.1.1 Model

We modeled the emission and detection of scintillation photons and the process of generation of the detector signals.

The mean emission rate of the scintillation photons is calculated from the mean number of emitted photons, the time constant of the scintillation pulse and the sampling time. The shape factor is assumed to be constant for the duration of the scintillation pulse, depending only on the scintillator material and the deposited gamma-ray energy. The scale factor $\theta(t)$ is calculated from the emission rate of the scintillation photons and the shape factor.

The emitted photon can have three possible outcomes – it can be detected by detector 1, or by detector 2 or not be detected. The collection efficiency of a detector is the fraction of total emitted light collected. It is a product of the quantum efficiency and the geometrical efficiency. In the Monte-Carlo simulation, we assume that the collection efficiencies of the detectors are independent of the position and angle of incidence of the scintillation photons. We use a uniform random variable to simulate the probability of detection of a scintillation photon.

The time it takes the scintillation photon to travel from the point of emission to the detector is much smaller (in the low picosecond range) than the detector response time (in the nanosecond range). Therefore, we neglect the propagation time of the scintillation photons from the point of emission to the detector. A scintillation photon emitted at time t_i is assumed to be instantaneously detected at the detectors (Choong, 2009; Kerisit et al., 2014).

The Normalized Detector Response Function (NDRF) is the normalized detector response in volts as a function of time. The normalization ensures that the area under the NDRF is equal to the product of the charge of an electron (q) and the input resistance of the oscilloscope (R).

$$\int_{0}^{\infty} \mathrm{NDRF}(t)dt = q \times R \tag{4.17}$$

The response of the detector in volts to a scintillation photon is given by multiplying the NDRF with the gain. We assume that the gain variances are normally distributed with mean gains of $\overline{G}_1, \overline{G}_2$, and variances of $\sigma^2_{G_1} = \beta_1\overline{G}^2_1$, $\sigma^2_{G_2} = \beta_2\overline{G}^2_2$ respectively. Here, β_1 and β_2 are the gain-noise factors for detector 1 and detector 2, respectively, defined as the ratio of the variance of their gain and the square of their mean gain. The NDRF was modeled as a Gaussian function of time with an experimentally observed Full-Width at Half Maximum (FWHM) of 1 ns.

The flowchart in Fig. 4.6 indicates the steps involved in creating the simulated detector outputs (s_{s1}, s_{s2}) from a scintillation pulse with known shape factor. The inputs to the algorithm are the scintillation photon properties like the shape factor (k), the mean number of scintillation photons emitted ($\overline{N}$) and the decay constant of the scintillator (τ); the characteristics of the two detectors such as their collection efficiencies (η_1, η_2), mean gains ($\overline{G}_1, \overline{G}_2$), and gain variance factors are defined as ($\beta_1 = \frac{\sigma^2_{G_1}}{\overline{G}^2_1}, \beta_2 = \frac{\sigma^2_{G_2}}{\overline{G}^2_2}$) respectively.

We used the algorithm in Fig. 4.6 to generate the simulated scintillation pulse shown in Fig. 4.7. Uncorrelated noise was added to the simulated pulse. The simulated signal outputs closely resemble the experimentally detected scintillation pulses in Fig. 4.19.

4.3.1.2 Assumptions made in the simulations

We have made the following assumptions in this simulation:

- The shape factor (k) of the scintillation pulse does not change for the duration of the pulse. This assumption might not be true for scintillators with after-

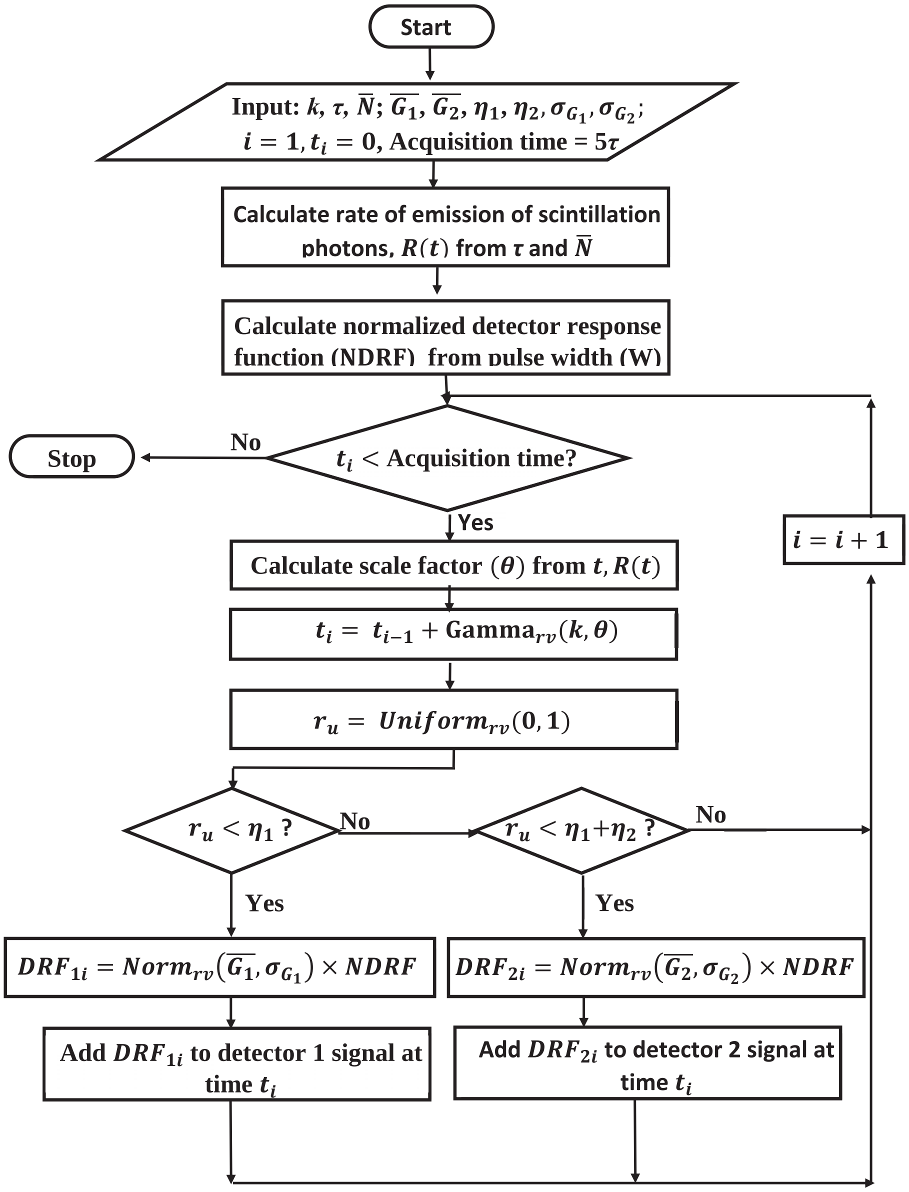

Figure 4.6: Flowchart to simulate detector pulses produced from scintillation light with known shape factor.

glow or multiple decay-time constants indicating the dominance of different underlying physical processes at different times of the scintillation pulse.

- The mean number of photons emitted by the scintillator per photoelectric

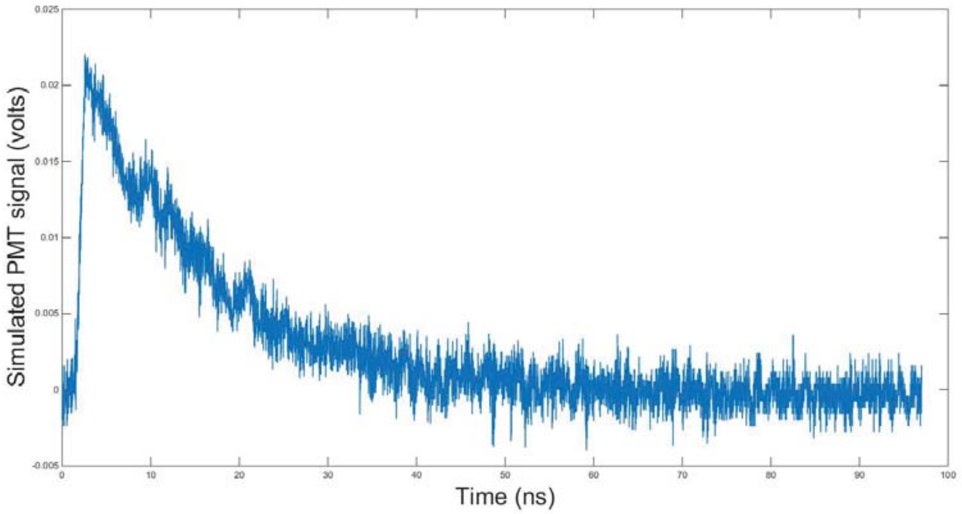

Figure 4.7: Simulated PMT signal with uncorrelated normally distributed noise from a 662 keV photopeak scintillation interaction in a $LaBr_3$:Ce scintillator. Performance parameters of the R9880U-210 PMT were used for this simulation.

gamma-ray interaction is known.

- The detector is operating in its linear region, and each photoelectron is amplified independently.
- Different PMT gains change the amplitude and the area under the NDRF waveform, but not the shape of the NDRF.
- The quantum efficiency of the detectors is assumed to be independent of the position of interaction.

The results for the simulations with these assumptions are highly dependent on one more crucial factor – the ratio of the decay time of the scintillator to the width of the single photoelectron response. If the detector response is orders of magnitude faster than the time constant of the scintillator, then the events captured are likely to be a set of separated photoelectrons. Because of the rarity condition of the Poisson postulates, the measured statistics of this point process will be close to Poisson (Barrett and Myers, 2004). Therefore, we have limited this study to fast scintillators YAP:Ce with a decay time of 30 ns and $LaBr_3$:Ce with a decay time of

15.4 ns.

4.3.1.3 Free Input parameters on the estimation of Fano factor

The free parameters in the simulation are the collection efficiencies (η_1, η_2), the mean gains and gain variances of the PMTs $(\overline{G}_1,\ \overline{G}_2,\ \beta_1,\ \beta_2)$, and the mean number of photons emitted $(\overline{N})$. Equation 4.18 is used to introduce a constraint and reduce the number of free parameters that we need to choose.

$$\int_0^T s_j(t)dt = \eta_j \overline{G}_j \overline{N}, \quad j = 1, 2. \tag{4.18}$$

If we assume values of $\overline{N}$ and $\eta_j,\ (j = 1, 2)$, then the values of $\overline{G}_j$ are constrained. Therefore, we only treat $\overline{N},\ \overline{\eta_1},\ \overline{\eta_2},\ \beta_1,\ \beta_2$ as free parameters. We performed five sets of Monte-Carlo simulations to test impact of each of these parameters. The simulations were performed for shape factors of 0.1 and 10 and therefore, Fano factors of 10 and 0.1, respectively.

In the first simulation, we varied the value of $\overline{N}$ from 20,000 to 60,000 scintillation photons with $\eta_1 = \eta_2 = 0.28$, $\beta_1 = \beta_2 = 0.25$. To satisfy Eq. 4.18, for different values of $\overline{N}$, we varied the mean gains $\overline{G}_1$ and $\overline{G}_2$ to keep the mean signal constant. We see in Fig. 4.8, that the normalized AUCCC asymptotically tends towards zero with higher values of $\overline{N}$ for Fano factor = 0.1 and Fano factor = 10. Therefore, an uncertainty in the estimate of $\overline{N}$ will be result in uncertainty in the estimate of the Fano factor.

In the second simulation, we varied the value of η_1 from 0.1 to 0.5 with $\overline{N} = 43692$, $\eta_2 = 0.28$, $\beta_1 = \beta_2 = 0.25$. To satisfy Eq. 4.18 for different values of η_1, we varied the mean gain $\overline{G}_1$ to keep the mean signal constant. We see in Fig. 4.9 that the normalized AUCCC is independent of the value of η_1 for Fano factor = 0.1 and Fano factor = 10.

In the third simulation, we simultaneously varied the values of collection efficiencies of both PMTs, $\eta_1 = \eta_2$ from 0.1 to 0.5 with $\overline{N} = 43692, \eta_2 = 0.28$, $\beta_1 = \beta_2 = 0.25$. To satisfy Eq. 4.18 for different values of η_1 and η_2, we varied the

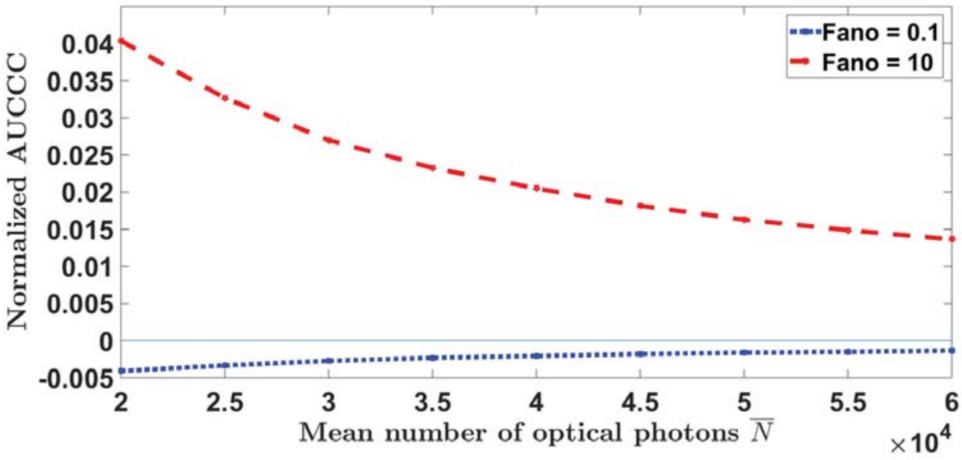

Figure 4.8: The normalized AUCCCs for different values of $\overline{N}$. As the values of normalized AUCCC increased, the value of mean gains had to be lowered to ensure that the equation of the mean signals is satisfied. Simulated datasets with Fano factors of 0.1 and 10 are plotted above; the normalized AUCCC tends towards zero with increasing value of $\overline{N}$. The solid line drawn at zero normalized AUCCC serves as a visual reference.

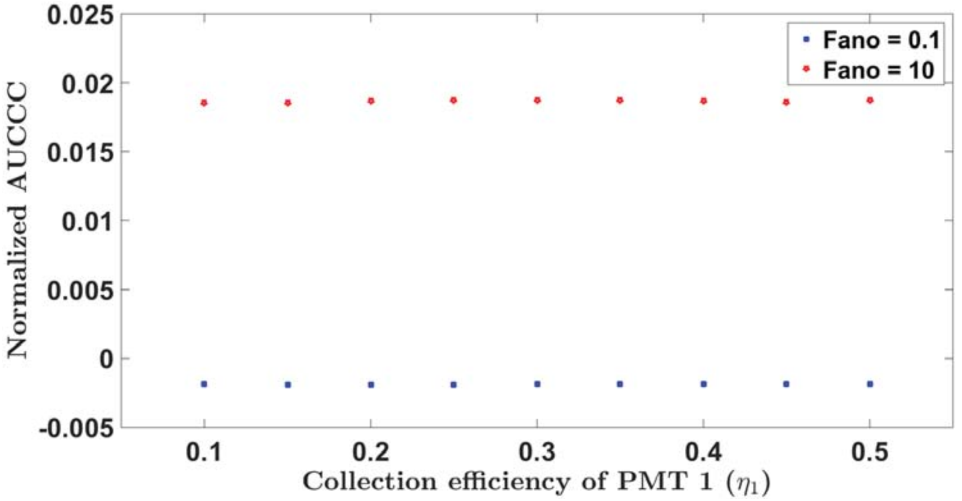

Figure 4.9: The normalized AUCCCs for different values of η_1, for Fano factor values of 0.1 and 10. The normalized AUCCC appears to be independent of the collection efficiency of the detectors.

mean gain $\overline{G}_1$ and $\overline{G}_1$ to keep the mean signal constant. We see in Fig. 4.10 that the normalized AUCCC is independent of the value of η_1 for Fano factor $= 0.1$ and Fano factor $= 10$.

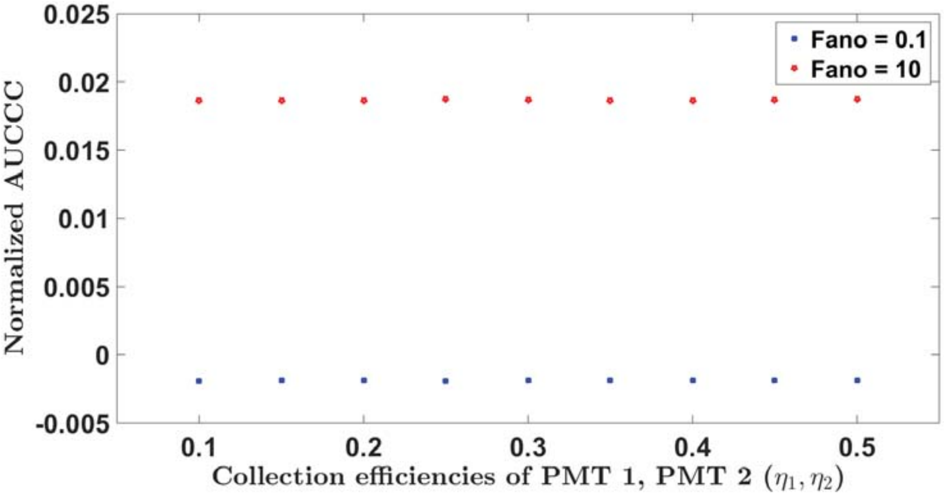

Figure 4.10: The normalized AUCCCs for different values of η_1, for Fano factor values of 0.1 and 10. The normalized AUCCC appears to be independent of the collection efficiency of the detectors.

In the fourth simulation, we varied the value of the gain variance parameter β_1 from 0.1 to 0.8, with $\overline{N} = 43692$, $\eta_1 = \eta_2 = 0.28$, $\beta_2 = 0.25$. We see in Fig. 4.11 that the normalized AUCCC is independent of the value of β_1 for Fano factor $= 0.1$ and Fano factor $= 10$.

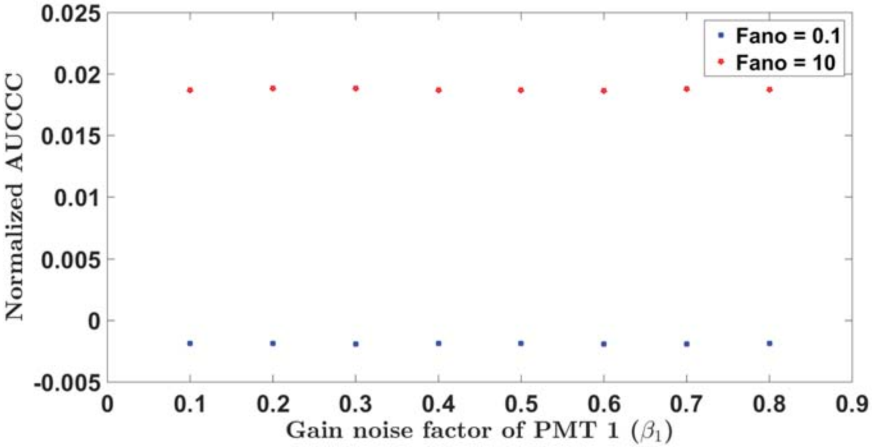

Figure 4.11: The normalized AUCCCs for different values of β_1, for Fano factor values of 0.1 and 10. The normalized AUCCC appears to be independent of the gain-variance factors of the detectors.

In the fifth simulation, we simultaneously varied the value of the gain variance parameters of both PMTs ($\beta_1 = \beta_2$) from 0.1 to 0.8, with $\overline{N} = 43692$, $\eta_1 = \eta_2 = 0.28$. We see in Fig. 4.12 that the normalized AUCCC is independent of the value of β_1 for Fano factor = 0.1 and Fano factor = 10.

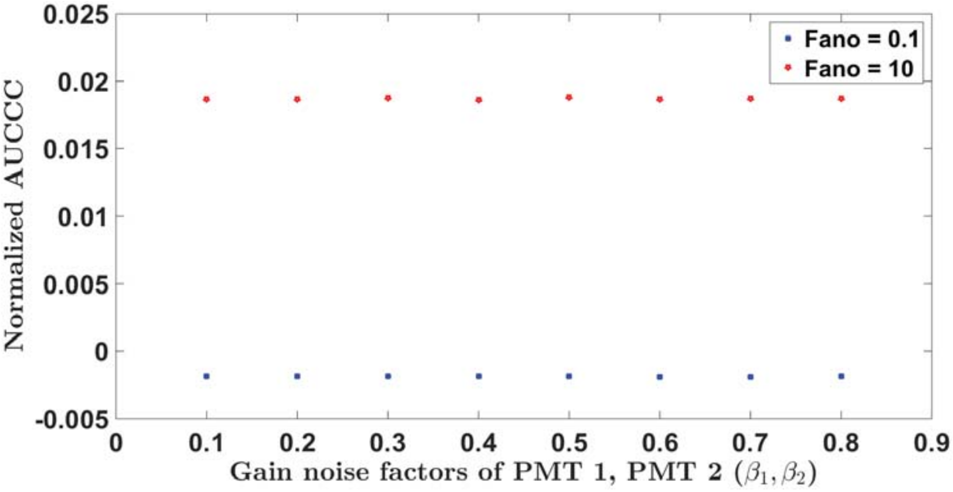

Figure 4.12: The normalized AUCCCs for different values of β_1, for Fano factor values of 0.1 and 10. The normalized AUCCC appears to be independent of the gain-variance factors of the detectors.

4.3.1.4 Invariance of the area under the covariance curve for thin energy windows of data

Our model assumes that the gamma-ray energy deposited in the scintillator is a constant. This is achieved in an experiment by windowing the photopeak region (which corresponds to photoelectric gamma-ray interactions) of the energy spectrum to separate it from the Compton region. In this section we investigate the impact of the size and location of the photopeak window on the normalized AUCCC.

To test the impact of the location and size of the energy window on the cross-covariance curves, we conducted a simulation study and generated a simulated data set with the following parameters : $\overline{N} = 43692$, $\eta_1 = \eta_2 = 0.28$, $\beta_1 = \beta_2 = 0.25$, $\overline{G}_1 = 6133$, $\overline{G}_2 = 5771$. We calculated the cross-covariance curves using Eq. 4.19 and used four different energy windows to generate the results shown in Fig. 4.13.

$$\mathrm{cov}(\mathrm{s}_1(\mathrm{t}), \mathrm{s}_2(\mathrm{t}) = (s_1(t) - \overline{s}_1(t))(s_2(t) - \overline{s}_2(t)). \tag{4.19}$$

The sub-figure (a) is the histogram of all 2000 photopeak events. The cross-covariance curve of the complete photopeak is plotted in (b). Only the left half (c), the right half (e) and the central region (g) of the energy spectrum were used to calculate the cross-covariance curve shown in (d), (f) and (h) respectively. Although the mean signals of the partial datasets in (a), (c), (e) and (g) are different, the cross-covariance curves, and therefore the normalized AUCCC of the two detector signals are similar and independent of the energy window selected.

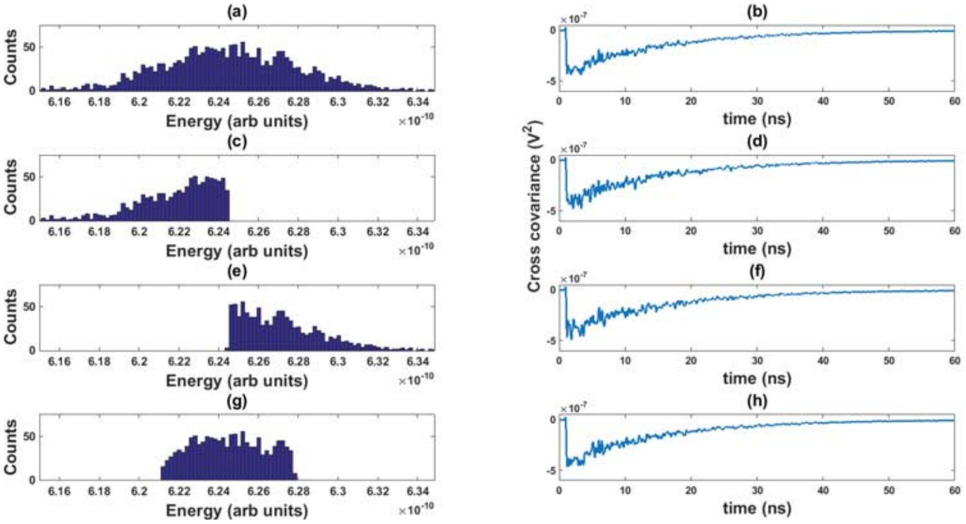

Figure 4.13: The cross-covariance curve for different energy windows of the same simulated dataset. The simulated dataset was generated with a shape factor of 10, and therefore, a Fano factor of 0.1. The plots in the left half of the figure show the parts of the photopeak histogram that were used to calculate the cross-covariance in the right half of the figure. The normalized AUCCC for the simulated data does not appear to be sensitive to the energy window of the histogram used to calculate it.

We also investigated if dividing the photopeak into a different number of energy windows will have an impact on the average normalized AUCCCs. Figure 4.14 shows that the average normalized AUCCC does not depend on the size or the number of the energy windows.

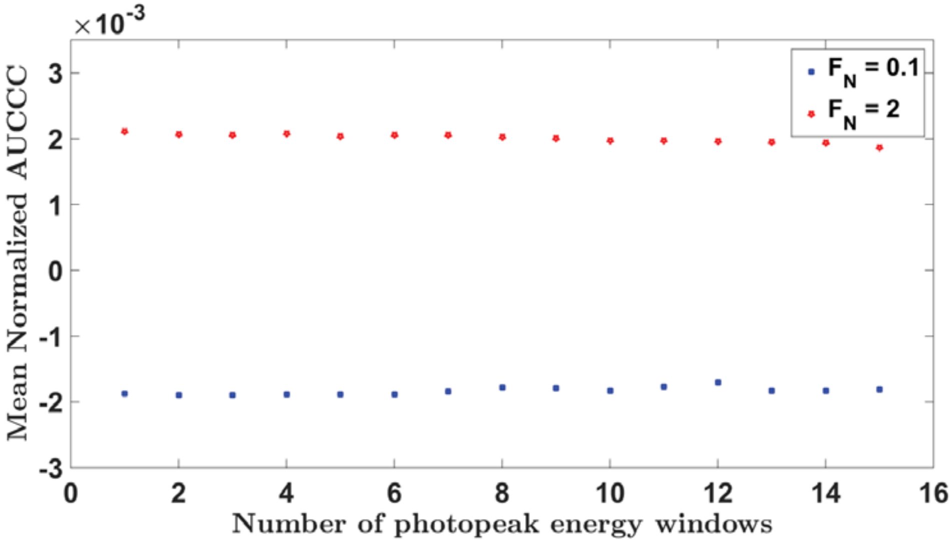

Figure 4.14: Average normalized AUCCC for simulated dataset as a function of number of energy windows the photopeak was divided into.

We have now numerically studied the impact of different parameters on our model. By fixing our mean detector outputs $(\int_0^T s_j(t)dt,\ (j = 1, 2))$ to the experimentally measured value, the normalized AUCCC is independent of the collection efficiency, gain variance and size of the energy window used for analysis. The estimate of the mean number of scintillation photons per photoelectric gamma-ray interaction $\overline{N}$ does impact the normalized AUCCC and an error in the value of $\overline{N}$ will be propagated to the final estimates of the Fano factor. We now have the tools and the model to compare against experimental data.

4.3.2 Experiment

A thin crystal of thickness 0.5 mm was sandwiched between two modified Hamamatsu R9880U-210 PMTs (see Fig. 4.15). The scintillator crystal was coupled to the PMTs with mineral oil. Hygroscopic crystals were polished on a 1500 grit emery paper before each measurement. The scintillator crystals were immersed in mineral oil for the duration of the experiment to prevent moisture damage and ensure good optical coupling between the scintillator and the PMTs. This was done with the help of a 3D printed custom part assembly shown in Fig. 4.16 . An O-ring sealed in place with a silicone sealant was used to keep the mineral oil from leaking out. The tube also provided mechanical support to the whole assembly and prevented movement of the PMTs and the crystal during the experiment. The assembly was wrapped tightly with black electrical tape to keep out ambient light.

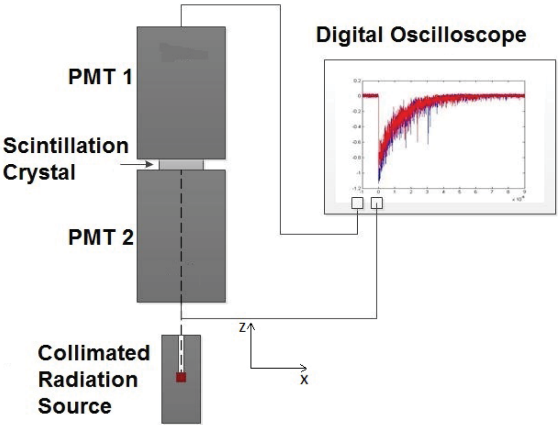

Figure 4.15: Experimental setup to measure the Fano factor of scintillation light using the correlation between the signals from two PMTs.

The R9880U-210 PMTs have a cover which prevented us from directly coupling two PMTs to a thin scintillator (see Fig. 4.17). On our request, custom R9880U-210 PMTs were manufactured without the outer covers as shown in Fig. 4.18. This modification does not affect the PMT's optical or electrical properties.

Scintillator crystal and PMT non-uniformities as well as variation in the geometrical efficiency for different points of interaction make the measurement sensitive to the position of interaction. These factors increase the variance and could impact the measurement of Fano factor. As shown in Fig. 4.15, we used a collimated Cs-137 (662 KeV) source of 1 mm diameter incident at the center of the scintillator to localize the position of interaction in the x-y plane (plane parallel to the detector faces), and a thin scintillation crystal to minimize variation along the z-axis.

To record data, we used a Tektronix DPO72004B oscilloscope at 20 GHz bandwidth at a sampling period of 20 ps for our measurements. A negative-edge AND trigger was used to trigger the oscilloscope. The recorded pulses corresponding to

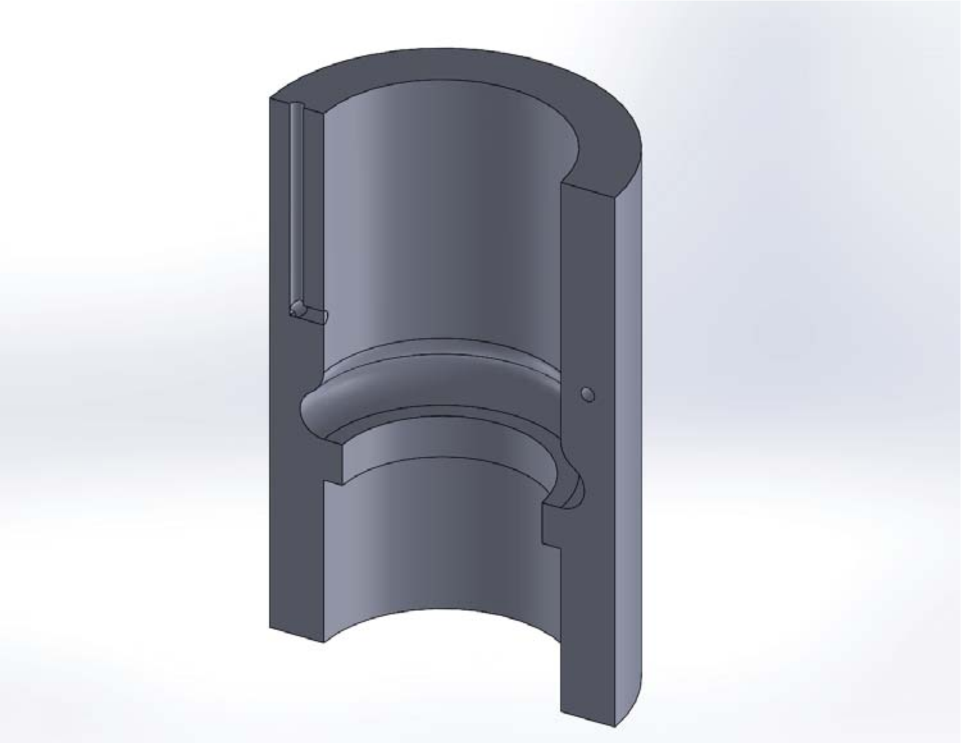

Figure 4.16: A rendering of the cross section of the 3D printed assembly used to seal the PMTs and scintillator in mineral oil. An O ring is secured with a sealant in groove in the lower half of the part to create an oil-tight seal.

Figure 4.17: Unmodified R9880U-210 PMT.

Figure 4.18: Modified R9880U-210 PMT.

the photopeak were selected and corrected for uncertainty in triggering. The oscilloscope also adds quantization and electronic noise to the detector signals. The noise in the two oscilloscope outputs was characterized by studying them without any signal. For a scintillation event, the noise between the two oscilloscope outputs was found to be uncorrelated; therefore, it does not affect the area under the cross-covariance curves. The drifts in the baseline signals were measured by averaging the oscilloscope outputs from the initial part of the scintillation pulses before the start of the scintillation event. The drifts in the oscilloscope outputs were subtracted from the respective detector signals to remove the offsets.

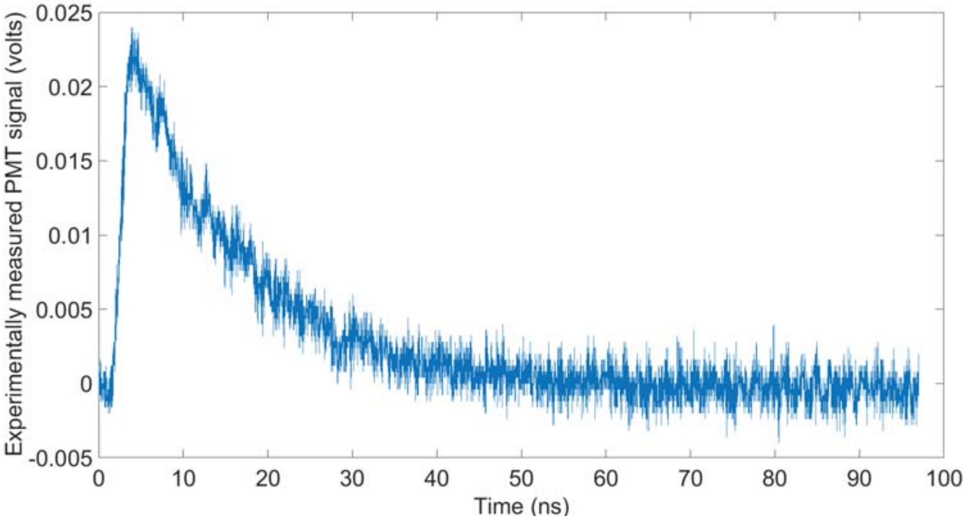

Figure 4.19: PMT Signal from a R9880U-210 PMT detecting a photopeak event in a $LaBr_3$:Ce scintillation crystal.

The experimental setup described in Sec. 4.3.2 was used to make covariance measurements on different scintillators. Pulses from two PMTs collecting light from the same event were detected with a fast PMT and a fast oscilloscope. The output of the detector was recorded using a DPO72004B at 20 GHz bandwidth and a sampling period of 20 ps per sample. The scintillation pulses were integrated in time and added together to make an energy spectrum. The photopeak events were selected by windowing this energy spectrum. The selected photopeak region was further divided into smaller energy windows for analysis.

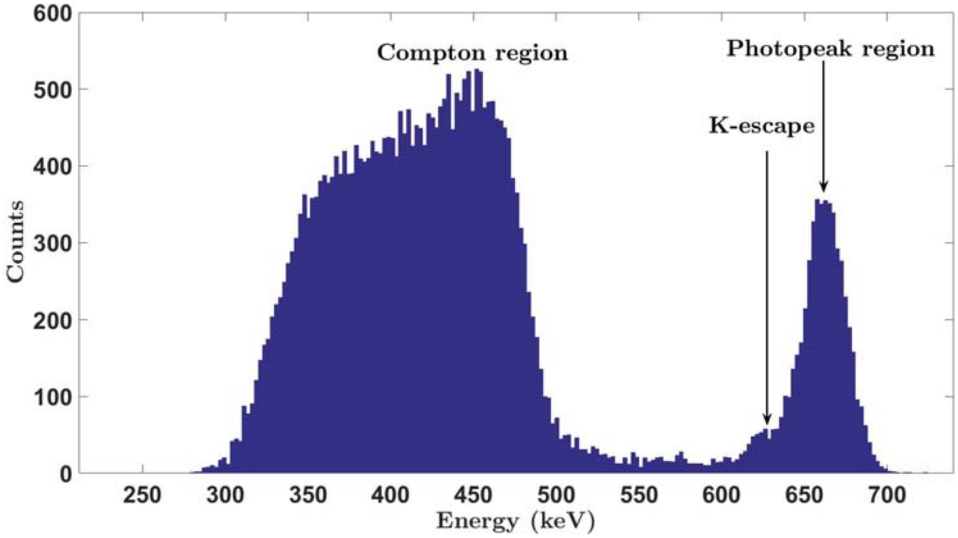

Figure 4.20: The energy spectrum of $LaBr_3$:Ce with R9880U-100-02 PMTS is shown above. The photopeak, K-escape and the Compton region are shown in the graph. Only the photopeak region of the energy spectrum was used for analysis.

Loss mechanisms like x-ray escape or low-angle Compton scattering can result in energy depositions which are lower than for the original gamma-ray interaction. These lossy gamma-ray events can be hard to distinguish from events in which all the original gamma-ray energy was deposited into the crystal. Inconsistent optical contact between scintillator and the crystal, can also result in broadening of the photopeak. Thus, the normalized AUCCC from the experimentally measured photopeak events will be biased towards positive cross-covariance.

If we choose a large energy window consisting of multiple gamma-ray energies deposited, then the mean pulses will correspond to the average of all the gamma-ray energy deposited. Events with higher-than-average gamma-ray energy deposited are more likely to produce pulses with amplitudes larger than the mean pulse, and events with lower than average gamma-ray energy deposited are more likely to produce pulses with amplitudes smaller than the mean pulse. Therefore, a large window corresponding to multiple gamma-ray energies will always result in a positive cross correlation curve.

The simulations in Sec. 4.3.1.4 indicate that if we choose a small energy window, which has only part of the spectrum of a single gamma-ray energy, then we should get more accurate and less biased values for normalized AUCCC.

4.4 Results

4.4.1 Simulation results

4.4.1.1 Relationship between Fano factor, shape factor and normalized AUCCC

We used the method described in Sec. 4.3.1.1 to simulate 2000 scintillation events with photoelectric interaction for the parameters of $\mathrm{LaBr_3}$:Ce and YAP:Ce for different values of Fano factor. The normalized AUCCC between the two sets simulated pulses s_1 and s_2 was calculated using equation Eq. 4.16. We used the proportional model below to model the relationship between the normalized AUCCC and the Fano factor.

$$\hat{F}_N = c + \frac{\mathrm{A}}{m}. \tag{4.20}$$

Here $\hat{F}_N$ is the estimated Fano factor of the scintillation photons, A is the measured normalized AUCCC, c is the x-intercept, and m is the slope of the model. As expected, if the Fano factor of the scintillation photons is one, then the two signals are expected to be uncorrelated and the normalized AUCCC is zero. As the Fano factor increases beyond one, the photons are bunched and the normalized AUCCC is positive. For Fano factors less than one, the photons are anti-bunched and the normalized AUCCC is negative. If the Fano factor is one, the normalized AUCCC must be zero (A= 0), and $c = 1$. Therefore, we need only to estimate the inverse of the slope for our model, and our model reduces to

$$\hat{F}_N = 1 + \frac{\mathrm{A}}{m}. \tag{4.21}$$

4.4.1.2 Model for LaBr$_3$:Ce

The simulation was setup to match the experiment. The LaBr$_3$:Ce scintillator was assumed to produce 0.662 MeV $\times$ 66,000 (photons per MeV) = 43692 scintillation photons. The collection efficiencies of both PMT's were assumed to be 0.28, and experimentally observed mean values of photopeaks of the two PMTs were set as $\left\langle \int_0^T s_1(t)dt \right\rangle_{PP} = 3.22 \times 10^{-10}$ volt-seconds, and $\left\langle \int_0^T s_2(t)dt \right\rangle_{PP} = 3.03 \times 10^{-10}$ volt-seconds. The rise time of the scintillation pulse was assumed to be zero, and the decay time was estimated from the measurements as 15.4 ns. The mean gains were calculated from Eq. 4.18, and the mean gain variance factors were set to $\beta_1 = \beta_2 = 0.25$.

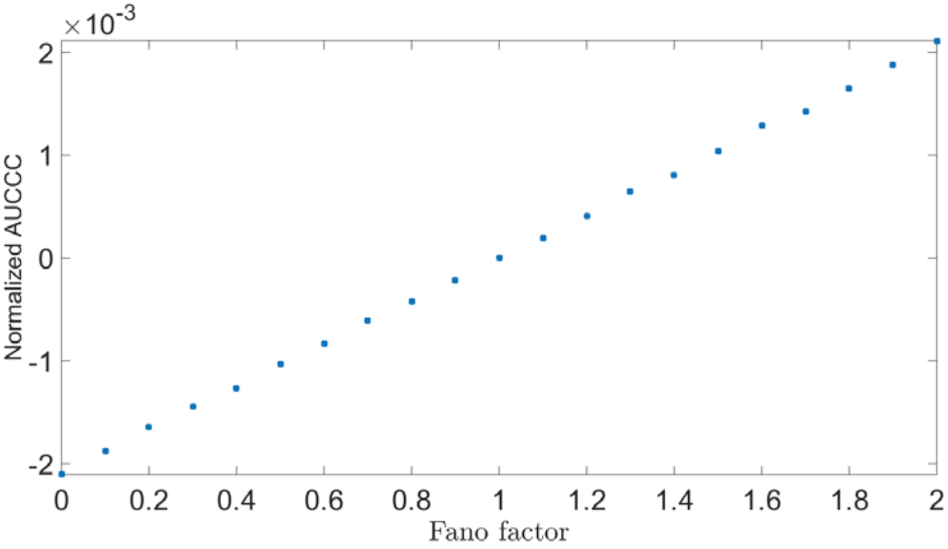

Figure 4.21: Model for the relationship between the normalized AUCCC and the Fano factor for LaBr$_3$:Ce. The normalized AUCCC has a proportional relationship with the Fano factor.

The model for the relationship between the normalized AUCCC (Normalized AUCCC$_{\text{LaBr}_3\text{:Ce}}$) and the Fano factor for LaBR$_3$:Ce is

$$F_{N_{\text{LaBr}_3\text{:Ce}}} = 1 + 473.9847 \times (\text{Normalized AUCCC})_{\text{LaBr}_3\text{:Ce}}. \tag{4.22}$$

4.4.1.3 Model for YAP:Ce

The YAP:Ce scintillator was assumed to produce 0.662 MeV $\times 15,000$ photons per MeV $= 9930$ scintillation photons. The collection efficiencies of each of the PMT's was assumed to be 0.28, and the experimentally observed mean values of the photopeaks of the two PMTs were set as $\left\langle \int_0^T s_1(t)dt \right\rangle_{PP} = 4.52 \times 10^{-9}$ volt-seconds, $\left\langle \int_0^T s_2(t)dt \right\rangle_{PP} = 4.68 \times 10^{-9}$ volt-seconds were used as the detector means. The rise time of the scintillation pulse was assumed to be zero, and the decay time was estimated from the measurements as 30 ns. The mean gains were calculated from Eq. 4.18 and the mean gain variance factors were set to $\beta_1 = \beta_2 = 0.25$.

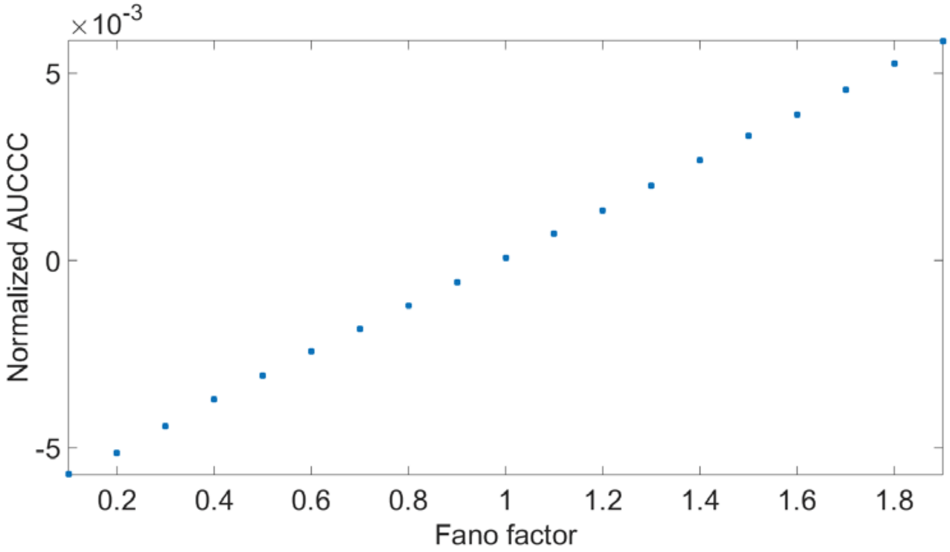

Figure 4.22: Model for the relationship between the normalized AUCCC and the Fano factor for YAP:Ce. The normalized AUCCC has a proportional relationship with the Fano factor.

The model for the relationship between the normalized AUCCC (Normalized AUCCC$_{\text{YAP:Ce}}$) and the Fano factor for YAP:Ce is

The model of our experiment for YAP:Ce is

$$F_{N_{\text{YAP:Ce}}} = 1 + 55.1314 \times (\text{Normalized AUCCC})_{\text{YAP:Ce}}. \tag{4.23}$$

4.4.2 Experimental results

The experimental setup described in Sec. 4.3.2 was used to make measurements on YAP:Ce and $LaBr_3$:Ce scintillators. Pulses from two PMTs collecting light from the same event were recorded with a fast detector and a fast oscilloscope and their cross-covariance curve computed. The normalized AUCCC was then computed and stored. The measurements for $LaBr_3$:Ce were conducted with PMT voltages of 500 V, while the measurements for YAP:Ce were conducted with PMT voltages of 700 V. Lower $LaBr_3$:Ce PMT voltages were used to ensure that the higher rate of photon emission in $LaBr_3$:Ce does not saturate the PMTs. The cross-covariance for the complete photopeak from a $LaBr_3$:Ce scintillation crystal is shown in Fig. 4.23.

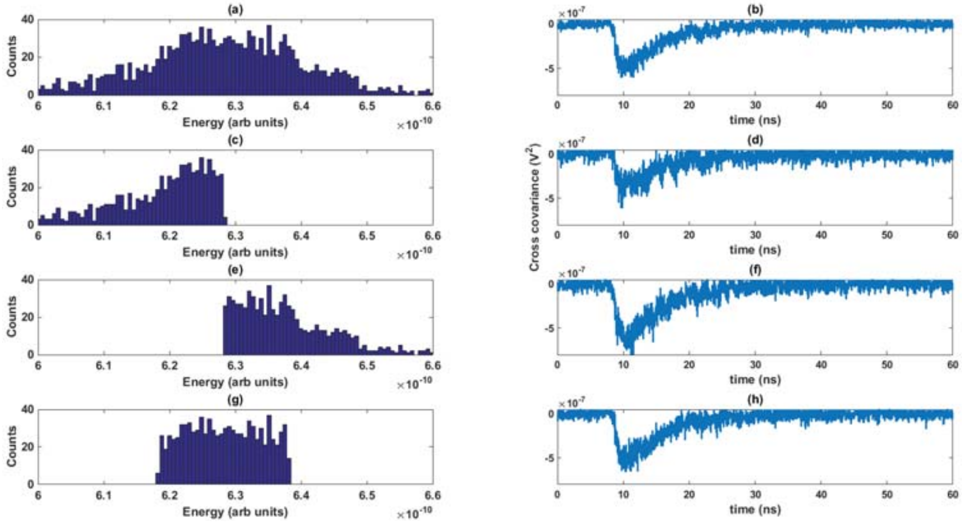

Figure 4.23: The temporal for different energy windows of the photopeak of an experimental measurement on $LaBr_3$:Ce. The plots in the left half of the figure show the parts of the photopeak histogram that were used to calculate the cross-covariance in the right half of the figure. The cross-covariance curve of the measured data does not appear to be sensitive to the energy window of the photopeak used to calculate it.

We have to threshold the experimental data to isolate photopeak events from Compton events. Unlike the simulated data, the experimental data cannot be assumed to originate from one gamma-ray energy. In Fig. 4.23 we see that the cross-covariance curves do not change substantially for different energy windows of the photopeak histogram.

We can also see from Fig. 4.24 and Fig. 4.25 that the average normalized AUCCC became more negative when we divided the photopeak into five or more equal energy windows as compared to using the complete photopeak (One large energy window). Dividing the photopeak into five, ten or fifteen energy windows does not significantly change the normalized AUCCC. This behavior could be because a smaller energy window contains interactions from fewer gamma-ray energies. The measurements with the worst energy resolutions (measurement 3 and 6 in Fig. 4.23) also recorded the biggest drops between the normalized AUCCCs for one photopeak energy window and the five photopeak energy windows.

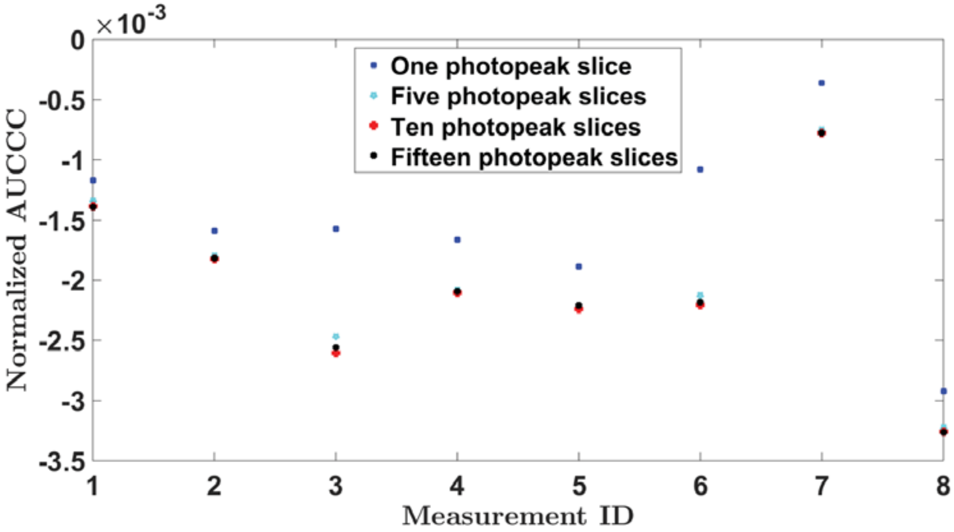

Figure 4.24: The average normalized AUCCC for different number of energy windows of the photopeak of an experimental measurement on $LaBr_3$:Ce. The normalized AUCCCs for the measured data does not appear to be sensitive to the size of the energy window of the photopeak used to calculate it.

As we have shown in Sec. 4.3.1.4, if we only have data from only one gamma-ray energy, the normalized AUCCC is independent of the size of the energy window, we must choose a smaller energy window to minimize the presence of other gamma-ray energies. Although, we expect the photopeak region to yield better results, windowing the energy into small windows also gives us an option to use the Compton region of the energy spectrum.

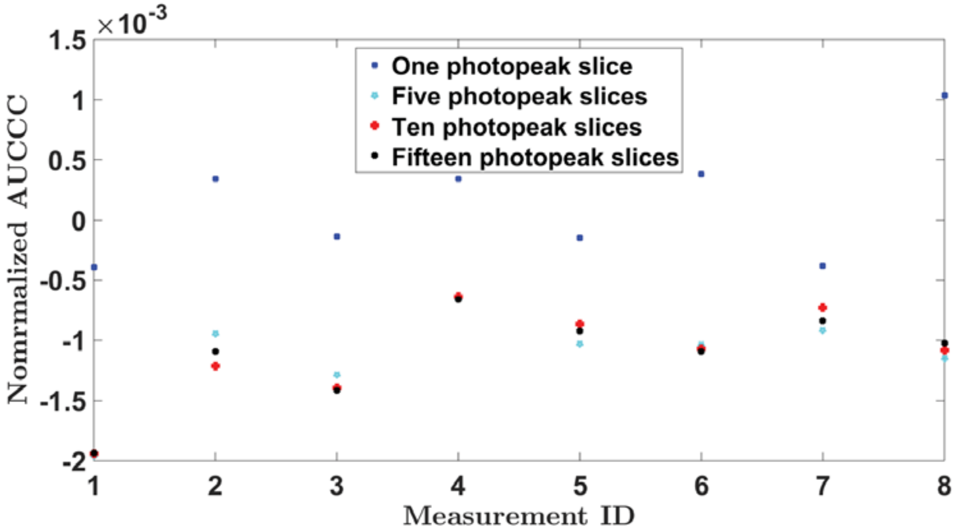

Figure 4.25: The average normalized AUCCC for different number of energy windows of the photopeak of an experimental measurement on YAP:Ce. The normalized AUCCCs for the measured data does not appear to be sensitive to the width energy windows of the energy spectrum used to calculate it.

4.4.3 Cross-covariance for different values of relative time shift

We also used Eq. 4.24 to calculate the cross-covariance for different values of the relative time shift τ.

$$\sigma(t,\tau) = \Big\langle \big[s_1(t) - \langle s_1(t)\rangle\big]\big[s_2(t+\tau) - \langle s_2(t+\tau)\rangle\big] \Big\rangle. \tag{4.24}$$

The resulting matrix is shown in Fig. 4.26 with time t varying along the x-axis and the time shift τ along the y axis. The region above the diagonal ($t = \tau$ line) is zero because there is no overlap between the non-zero regions of the two pulses. A small time region before the start of the scintillation signal was also recorded, this causes an offset in the most negative region of the image, and results in the shift of that region from the diagonal.

While most of the Fig. 4.26 is either zero or negative, there is a small region at $\tau = 0$, $t \approx 7.5$ ns that is positive. This is an experimental artifact caused by the uncertainty in the triggering mechanism of our system. The mean detector signals are calculated from an ensemble from all the photopeak detector signals, they start rising from zero at $t \approx 7$ ns. If a scintillation pulse arrives a little before the time when mean detector signals start to rise, for a small amount of time after the scintillation pulse arrives, the detector signals are positive, but the mean signals are still zero. Therefore, both differences between the amplitudes of the signals and their respective mean signals will be positive, giving us a positive cross-covariance. Similarly, if the detector pulses arrive a little earlier, the cross-covariance will again be positive.

As the scintillation pulse decays, due to the rarity, the statistics tend towards Poisson statistics. Therefore, for larger values of t the cross-covariance tends toward zero. As τ increases beyond 30 ns, the cross-correlations decrease and tend towards zero Barrett and Myers (2004).

4.4.4 Estimate of the Fano factor

The normalized AUCCC for YAP:Ce and LaBr$_3$:Ce was estimated by using the experimental data with 10 energy windows. The Fano factors for YAP:Ce and LaBr$_3$:Ce were estimated using Eq. 4.23 and Eq. 4.22, respectively.

Table 4.1: Fano factor estimates from Normalized AUCCC

	Normalized AUCCC	Photon Fano factor (F_N)
YAP:Ce	$-1.1\times10^{-3}\pm5.2\times10^{-5}$	0.9385 ± 0.0107
LaBr$_3$:Ce	$-2.0\times10^{-3}\pm9.3\times10^{-5}$	0.0292 ± 0.1565

4.5 Comparison of Fano factor estimates from temporal and integral correlations

The estimates of Fano factor from the time correlations for both the scintillators are smaller than the estimates from the integral correlations in the previous chapter. This could be a result of a bias towards lower Fano factor values in the time-correlation estimates, or a bias towards higher Fano factor values in the integral-correlation estimates or both.

The different loss mechanisms like x-ray escape and low angle Compton scattering will bias the Fano factor estimates from integral correlations biased towards

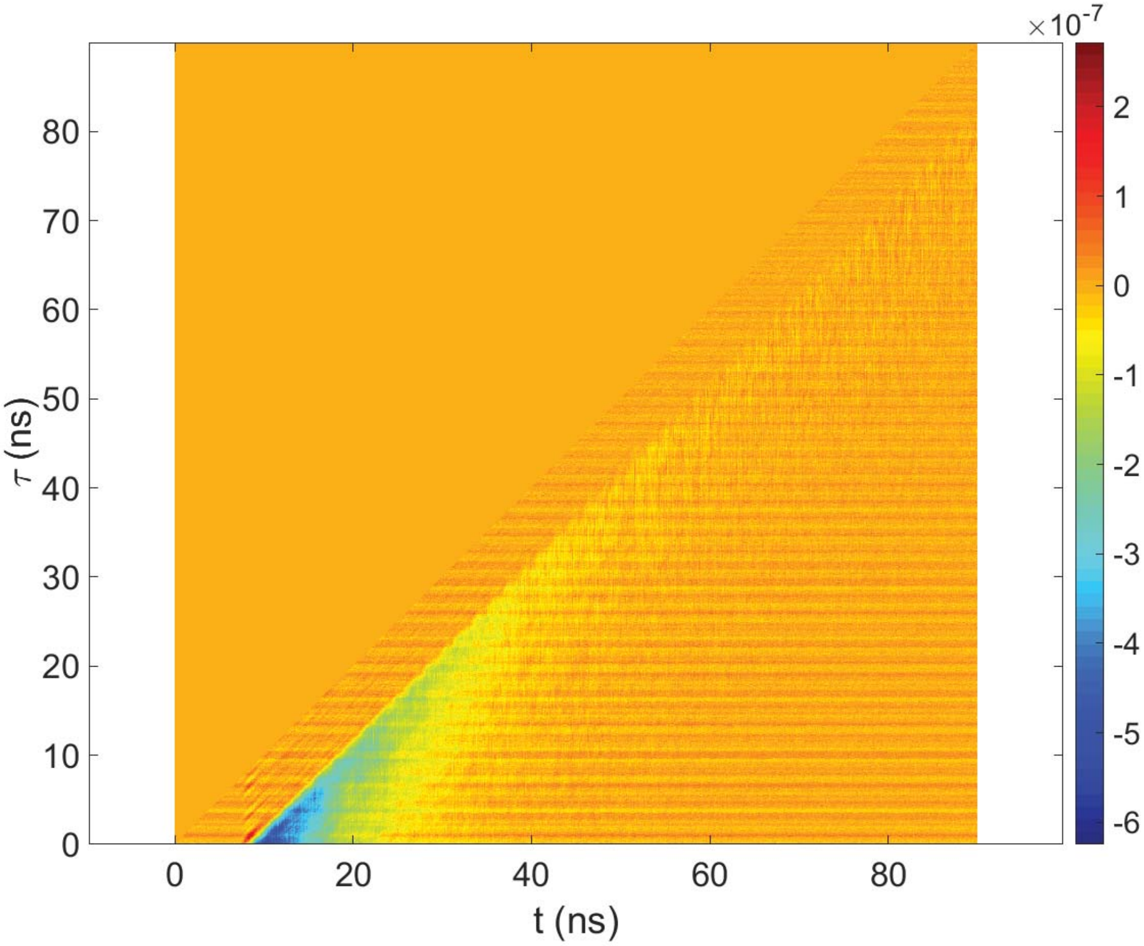

Figure 4.26: Cross-covariance as a function of the detector signal as a funtion of time t and shift τ.

higher Fano factors. The photon Fano factor estimates of LaBr$_3$:Ce from both the methods are within each others error bars. We are not aware of a bias in our measurements from the temporal correlations.

The estimate of the correlation coefficient of YAP:Ce is close to zero ($\hat{r}_{12_{YAP:Ce}} = 0.10$), as a result the estimate of the photoelectron Fano factor was close to one ($\hat{F}_{n_{YAP:Ce}} = 1.13$). The estimates of the photon Fano factor are sensitive to the value of η. The value of η amplifies the deviation of the correlation coefficient from zero. As a result the small deviation from zero in the estimate of the correlation coefficient is amplified and the estimate of the photon Fano factor for YAP is $F_{N_{YAP:Ce}} = 1.46$.

For example, a value of $\hat{r}_{12} = -0.1$ will yield a photon Fano factor of $(F_N = 0.6526)$. The value of the correlation coefficient of $\hat{r}_{12} = -0.0165$ will yields the Fano factor estimate from the temporal correlation.

CHAPTER 5

Impact of Fano Factor on Position and Energy Estimation in Scintillation Cameras

Large parts of this chapter have been published in (Bora et al., 2015).

5.1 Introduction

A gamma-ray scintillation camera has two main components – a scintillation crystal and an array of optical detectors. When a scintillation crystal is excited by gamma-rays, it emits optical photons. These optical photons are then detected by an array of optical detectors whose outputs are used to estimate the position of interaction (x, y, z) and the energy deposited (E).

The difference between gamma-ray spectroscopy and gamma-ray imaging camera is that gamma-ray spectroscopy detectors estimate only the energy of gamma-rays. Therefore, they are designed to make the scintillation light collection independent of the position of interaction. However, in a gamma-ray scintillation camera, both the energy and position of interaction of the gamma-rays are estimated. In a gamma-ray scintillation camera, the estimates of position and energy influence each other and the position of interaction (x, y, z) is used to compensate for any position dependence of the light collection.

In a gamma-ray scintillation camera, the various parameters that describe the interaction of the gamma-ray photon with the detector, such as the position of interaction and energy deposited by a detected gamma-ray photon, are estimated using the detector outputs. Since a reduction in the Fano factor results in a smaller variance in the number of emitted optical photons and consequently a smaller variance in the detector outputs, we would expect that this should also lead to reduction in variance of the parameters estimated from the low-variance detector outputs. Thus, a variation in Fano factor could potentially affect the energy and spatial resolution of a gamma-ray imaging system.

We used two approaches to study the impact of Fano factor on the spatial and energy resolution – calculating the Cramér-Rao Bound (CRB) and estimating the variance of a maximum likelihood (ML) estimator (Cramer, 1946; Rao, 1945). CRB is the theoretical lower bound on the variance of an unbiased estimator.

An unbiased estimator is efficient if it achieves the CRB (Barrett and Myers, 2004). If an efficient estimator exists, the ML estimator will be efficient. We do not directly prove the existence of an efficient estimator for our problem. However, if the estimates of the variance of the ML estimator are unbiased and approach the CRB – then the results are consistent with the hypothesis that an efficient estimator exists and our ML estimator is efficient. We can then quantitatively validate both of our approaches.

The use of ML estimation methods for position estimation in scintillation gamma-ray detectors was first proposed by Gray and Macovski (Gray and Macovski, 1974), and then demonstrated on modular gamma-cameras (Milster et al., 1984, 1985; Clinthorne et al., 1987; Milster et al., 1990; Aarsvold et al., 1995). The use of ML position estimation in SPECT imaging systems was demonstrated by Rowe *et al.* (Rowe et al., 1993). Availability of faster computing, advances in calibration and faster algorithms have made ML position estimation very fast and inexpensive to implement (Chen et al., 2005; Hesterman et al., 2010). The ML estimators have significant advantages over the traditional Anger arithmetic – no bias, lower mean-squared error and the ability to achieve the CRB (Barrett et al., 2010).

The ability of the ML position estimators to approach the CRB in scintillation gamma-ray detectors has made the CRB a very useful tool. The CRB has been widely used for evaluating the performance of gamma-ray detectors (Li et al., 2012; Moore, 2011). The CRB has also been used to optimize gamma-camera design (Korevaar et al., 2013; van der Laan et al., 2006), evaluate different readout strategies (Salcin et al., 2011) and calculate the theoretical bound on timing resolution (Seifert et al., 2012).

This chapter is organized in the following sections: In Sec. 5.2.1, we briefly introduce the likelihood function, Fisher information matrix and Cramér-Rao bound. In Sec. 5.3 we discuss our model of production and transport of scintillation light. We discuss the various implementation details including assumptions and simulation parameters. We introduce two geometries in Sec. 5.4 – with 3×1 and 3×3 optical detector elements. For the 3×1 geometry, we analytically calculate the CRB for two special values of Fano factor ($F_N = 0$ and $F_N = 1$), and we use a more general model to numerically calculate the CRB for Fano factors other than zero. We use Monte-Carlo simulations to estimate the variance of the ML estimator for the 3×1 and the 3×3 geometries. The results of the analytical and the numerical calculations of the CRB, and the variance of the ML estimator for the 3×1 geometry and the 3×3 geometries are discussed in Sec. 5.5.

5.2 Theory

5.2.1 Likelihood function

If we intend to estimate a parameter vector ($\vec{\theta}$) from acquired data ($\vec{g}$), we can define the likelihood function as

$$l(\vec{\theta}|\vec{g}) = Pr(\vec{g}|\vec{\theta}). \tag{5.1}$$

Here $Pr(\vec{g}|\vec{\theta})$ is the probability of the parameters ($\vec{\theta}$) resulting in data outputs ($\vec{g}$). In a gamma-ray scintillation camera, $\vec{g}$ is a vector of detector outputs for a gamma-ray interaction, and as we are estimating the position of interaction and gamma-ray energy, $\vec{\theta} = (x, y, z, E)$. The likelihood function $l(\vec{\theta}|\vec{g})$ gives us the likelihood of measuring $\vec{g}$ given a gamma-ray photon that deposits energy E at location (x, y, z) in the scintillation crystal (Barrett and Myers, 2004).

5.2.2 Score, Fisher information matrix and Cramér-Rao bound

The sensitivity of the likelihood function to changes in the parameter vector $\vec{\theta}$ is given by the score ($\vec{s}$). The score is defined as the gradient of the logarithm of the likelihood function (log-likelihood) of the acquired data:

$$s_i(\vec{g}|\theta) = \frac{\frac{\partial}{\partial\theta_i} Pr(\vec{g}|\vec{\theta})}{Pr(\vec{g}|\vec{\theta})} = \frac{\partial}{\partial\theta_i}\log(Pr(\vec{g}|\vec{\theta}). \tag{5.2}$$

The Fisher information matrix (I) is the covariance matrix of the score. The mean value of the score is given by

$$\langle s\rangle_{\vec{g}|\theta} \;=\; \int_{-\infty}^{\infty} d^M g \quad \mathrm{pr}(\vec{g}|\theta)\frac{\frac{\partial}{\partial\vec{\theta}}\mathrm{pr}(\vec{g}|\vec{\theta})}{\mathrm{pr}(\vec{g}|\vec{\theta})} \;=\; \frac{\partial}{\partial\vec{\theta}}\int_{-\infty}^{\infty}\mathrm{pr}(\vec{g}|\vec{\theta}) \;=\; \frac{\partial}{\partial\theta}(1) \;=\; 0. \tag{5.3}$$

As the mean value of score is zero (Barrett and Myers, 2004), the $(i,k)^{\text{th}}$ element of the Fisher information matrix are given by

$$I_{ik} = \langle s_i s_k\rangle_{\vec{g}|\vec{\theta}}\,. \tag{5.4}$$

The angle brackets here indicate the expectation value, which involves multiplying $s_i s_k$ by the probability $Pr(\vec{g}|\vec{\theta})$ and integrating over all the detector outputs $\vec{g}$ for a given value of $\vec{\theta} = (x, y, z, E)$. The diagonal elements of the inverse of the Fisher information matrix give us the CRB,

$$\mathrm{CRB}_i = (I^{-1})_{ii}. \tag{5.5}$$

Here the CRB_i denotes the Cramér-Rao bound for the i^{th} parameter. If we use an unbiased estimator to estimate a parameter $\hat{\theta}_i$, then the variance of $\hat{\theta}_i$ ($Var(\hat{\theta}_{i_{UB}})$) cannot be lower than the CRB of the i^{th} parameter

$$Var(\hat{\theta}_{i_{UB}}) \geq CRB_i. \tag{5.6}$$

In a typical gamma-ray scintillation camera, four parameters (x, y, z, E) are estimated. Therefore, the complete Fisher information matrix is a 4 × 4 matrix. However, when we know the value of some of these parameters, then the Fisher information dimensionality reduces. For example, if we place a thin lead slit perpendicular to the y-axis above the scintillator crystal. The slit localizes the y interactions position and we can treat y as a known parameter and only estimate

(x, z, E), reducing the Fisher information to a 3×3 matrix. In this scenario, as we assume that the exact value of y is known, the uncertainty in the $\hat{y}$ estimates does not add uncertainty to the $\hat{x}$, $\hat{z}$, $\hat{E}$ estimates. In fact, it can be mathematically shown that for any estimation model, the CRB on the i^{th} parameter calculated from a Fisher information matrix of dimensions $a \times a$ denoted by $\text{CRB}_{(a)_i}$ will always be greater than or equal to the CRB calculated from a smaller square sub-matrix of the $a \times a$ Fisher information matrix (See A).

$$\text{CRB}_{(a)_i} \geq \text{CRB}_{(a-1)_i}. \tag{5.7}$$

5.2.3 Variance of maximum likelihood estimator

The variance of an unbiased estimator is a good metric for the resolution of a system. For an unbiased estimator, a smaller variance enables a system to resolve closer values of the parameters, giving the system better resolution.

The ML estimator maximizes the likelihood function to yield the most likely parameter vector $\vec{\theta}$ that would result in output data $\vec{g}$. In our study, detector outputs ($\vec{g}$) were generated for a position of interaction (x, y, z) and gamma-ray energy deposited (E). The ML estimator was applied on these set of detector outputs to estimate $\hat{x}$, $\hat{y}$, $\hat{z}$ and $\hat{E}$. The operator $\text{argmax}_{\vec{\theta}}$ returns the values of the arguments of the likelihood function at its maximum value

$$\hat{\vec{\theta}} = \underset{\vec{\theta}}{\text{argmax}}(l(\vec{\theta}|\vec{g})). \tag{5.8}$$

The variance of the ML estimator is estimated by computing the variance of the estimates.

5.3 Model

5.3.1 Modeling the scintillation process

When excited by gamma-rays, a scintillator crystal deexcites through a complicated cascade process and emits optical photons (Knoll, 2010; Rodnyi, 1997). In this study all the scintillation light is assumed to be emitted from the point of interaction. This is an approximation as the energy deposited by the gamma-ray photon produces a high-energy electron, which travels at a high velocity depositing energy and creating electrons=hole pairs along its path. Some of these electron-hole pairs recombine radiatively to emit optical scintillation photons not just at the point of interaction, but along the path of the high-energy electron.

The excitons that de-excite to emit the optical photons have no memory of the direction of the incident gamma-ray or the high-energy electron. Hence, it is reasonable to assume that the scintillation photons are emitted isotropically from the point of interaction.

Consider a gamma-ray interaction that deposits energy E in the scintillator. The scintillator de-excites by producing a random number of optical scintillation photons (N). The mean number of optical photons emitted is given by

$$\overline{N} = Q \cdot E. \tag{5.9}$$

Here, Q is the average number of optical photons emitted per-unit-energy deposited. Scintillator non-proportionality can result in a non-linear relationship between E and $\overline{N}$ which makes Q a function of deposited energy (Moses et al., 2012). If the Fano factor of the scintillator is denoted by F_N, the variance in the number of optical photons is given by

$$\sigma_N^2 = F_N \cdot \overline{N}. \tag{5.10}$$

The probability of producing N optical scintillation photons given energy E deposited is modeled as a discrete normal distribution with mean $\overline{N}$ and variance $F_N \cdot \overline{N}$. In the simulations, as the mean and variance of this discrete normal distribution are relatively large, the probability of N is approximated by a sampled continuous normal distribution (Szablowski, 2001) given by

$$Pr(N|F_N, E) = \frac{1}{\sqrt{(2\pi F_N Q E)}} \exp\left(-\frac{(N-QE)^2}{2F_N Q E}\right). \tag{5.11}$$

Even if Q is a function of the deposited gamma-ray energy, the relationship between the deposited gamma-ray energy and average number of scintillation photons emitted is a monotonically increasing function – as we increase the energy of the gamma-ray photons, on average, a larger number of scintillation photons are emitted. Therefore, instead of estimating the position of interaction and the deposited gamma-ray photon energy (x, y, z, E), we can estimate the position of interaction and the mean number of scintillation photons emitted $(x, y, z, \overline{N})$. The statistical model given in (5.11) can be alternatively written as

$$Pr(N|F_N, \overline{N}) = \frac{1}{\sqrt{2\pi F_N \overline{N}}} \exp\left(-\frac{(N-\overline{N})^2}{2F_N\overline{N}}\right). \tag{5.12}$$

5.3.2 Modeling the optical photon transport

If N optical scintillation photons are produced from a gamma-ray interaction at (x, y, z), the number of detected optical photons on a J-element optical detector follows a multinomial distribution with $J+1$ outcomes. J of the outcomes are due to the optical photons detected at detector-elements $j = 1, 2 \cdots J$, with probability of detection at the j^{th} element, α_j. In our model α_j is given by

$$\alpha_j(x, y, z) = \eta \frac{\Omega_j(x, y, z)}{4\pi}. \tag{5.13}$$

Here η, the quantum efficiency of the optical detector-elements, is assumed to be independent of the angle of incidence, and Ω_j is the effective solid angle subtended by the j^{th} detector-element from the point of interaction (x, y, z). Specular or Lambertian reflectors can be used to increase the effective solid angle. We have also ignored all scattering processes – only optical photons directly impinging on the detector are considered. Thus, α_j is equal to the product of quantum efficiency and geometrical efficiency of the j^{th} detector element. The $(J+1)^{\text{th}}$ outcome contains all the optical photons not detected by any of the J detector elements. The probability of an optical photon not being detected is $(1 - \sum_{j=1}^{J} \alpha_j)$ (Barrett and Myers, 2004).

The detector array is assumed to be photon counting and noiseless. These two assumptions ensure that the data outputs are integer-valued and reduce the Fisher information matrix calculation from an integral to a summation. For each gamma-ray event, the detector-array outputs $\vec{g}$ is a J-dimensional integer vector whose j^{th} element is the number of optical photons detected on the j^{th} detector-element. The probability of measuring $\vec{g}$ for a gamma-ray interaction which produces N optical photons at (x, y, z) is given by the multinomial distribution.

$$Pr(\vec{g}|x, y, z, N) = N! \left(\prod_{j=1}^{J} \frac{\alpha_j^{g_j}}{g_j!}\right) \quad \frac{\left(1 - \sum_{j=1}^{J} \alpha_j\right)^{\left(N - \sum_{j=1}^{J} g_j\right)}}{\left(N - \sum_{j=1}^{J} g_j\right)!}. \tag{5.14}$$

The complete probability of $\vec{g}$ for an interaction at position (x, y, z), Fano factor F_N and deposited energy E producing on average $\overline{N}$ optical scintillation photons is given by marginalizing (5.14) over N

$$Pr(\vec{g}|x, y, z, F_N, \overline{N}) = \sum_{N=1}^{\infty} Pr(\vec{g}|x, y, z, N) \times Pr(N|F_N, \overline{N}). \tag{5.15}$$

We substitute (5.15) in (5.1) to get an expression for the likelihood function $l(x, y, z, \overline{N}|\vec{g})$ of a gamma-ray interaction at x, y, z with mean number of photons emitted $\overline{N}$, resulting in detector output vector $\vec{g}$.

$$l(x, y, z, \overline{N}|F_N, \vec{g}) = Pr(\vec{g}|x, y, z, F_N, \overline{N}) = \sum_{N=1}^{\infty} Pr(\vec{g}|x, y, z, N) \times Pr(N|F_N, \overline{N}). \tag{5.16}$$

5.4 Implementation

5.4.1 Assumptions for maximizing the impact of Fano factor

All practical detectors convert a fraction of the incident optical photons to photoelectrons, which then are amplified and recorded. The Fano factor of the photoelectrons on the j^{th} detector-element (F_{nj}) is given by (Bousselham et al., 2010)

$$F_{nj} = 1 + \alpha_j(F_N - 1). \tag{5.17}$$

Here, α_j is the fraction of emitted optical photons detected at the j^{th} detector-element. In the optical photon transport model described in Sec. 5.3.2, α_j is the product of the quantum and geometrical efficiencies of the j^{th} detector-element. If each detector element captures a very small fraction of scintillation light (small α_j), then irrespective of the Fano factor of the scintillator, all the detectors elements will have Poisson statistics and a Fano factor of one(See (5.17)). Our initial studies conducted with practical geometries and quantum efficiency of 40% found no impact of Fano factor on the spatial resolution. To ensure that our simulation results are not an artifact due to low optical photon collection efficiency, we maximized the impact of the Fano factor on the detector outputs by maximize the geometrical and quantum efficiencies of the detector-elements.

The geometrical efficiency was maximized by using a large-area optical detector divided into a small number of detector-elements. Using a 100% reflecting retroreflector, the scintillation light emitted in a direction away from the detector is reflected back onto the detector. The retroreflector effectively doubles the geometrical efficiency of the detector. The quantum efficiency of the detector is set to one, thus all optical photons incident on the detector-array are detected and counted. Sources of noise which will add variance are assumed to be zero – the photodetector is assumed to be noiseless and the scintillator crystal is assumed not to scatter or absorb the scintillation light.

5.4.2 Computation limitations for calculating the Cramér-Rao bound

To calculate the CRB, we first need to compute the score and its covariance matrix. The computation required to calculate the score can be clearly seen by using (5.15) to expand the angle brackets in (5.4)

$$I_{ik} = \sum_{N=1}^{\infty} \sum_{\vec{g}} (s_i s_k) Pr(\vec{g}|x, y, z, N) Pr(N|F_N, \overline{N}). \tag{5.18}$$

For an optical detector with J detector elements, calculating one matrix element of the Fisher information matrix for one set of $\vec{\theta} = (x, y, z, \overline{N})$ requires J+2 dimensional summations. Equation (5.18) requires J+1 dimensional summations; J-dimensional summations over all the detector outputs and a summation over N. In addition, the expression for $Pr(\vec{g}|x, y, z, \overline{N})$ from (5.15) has a summation over N. Due to the large computation time required to calculate the Fisher Information matrix, we computed the Fisher information matrix only for a geometry with a 3 × 1 array of detector elements.

5.4.3 Geometry of 3 × 1 detector

In one of our studies, the scintillator crystal is a single crystal with dimensions of 20 cm × 20 cm × 2 cm. The scintillator crystal is sandwiched between a 20 cm × 20 cm × 1 cm light guide of the same refractive index as the scintillator and a retroreflector on the opposite face (see Fig. 5.1). Light from the scintillator crystal goes through the light guide onto the optical detector. Reflectivities at the interfaces between the crystal, light guide and optical detector are assumed to be zero, and the interface between the crystal and the retroreflector is assumed to be 100% reflecting. The four other faces of the crystal are blackened and assumed to be 100% absorptive. The 3 × 1 detector geometry has three 5 cm × 15 cm optical detector-elements.

In this 3 × 1 geometry, we lose nearly all information about y, thus, we only estimate x, z and $\overline{N}$. To minimize computation, y is treated as a known parameter. We used the symmetry of the system and computed the Fisher information matrix for only one side of the detector as shown in Fig. 5.1.

The mean detector response function (MDRF) is the average detector response for a given position of interaction and gamma-ray energy (x, y, z, E). The quantum efficiency is assumed to be one ($\eta = 1$), and the 100 % reflecting retroreflector doubles the effective solid angle subtended by each detector-element. The expression of the normalized MDRF of j^{th} detector-elements is

$$\mathrm{MDRF}_j(x, y, z) = 2 \times \frac{\Omega_j(x, y, z)}{4\pi}. \tag{5.19}$$

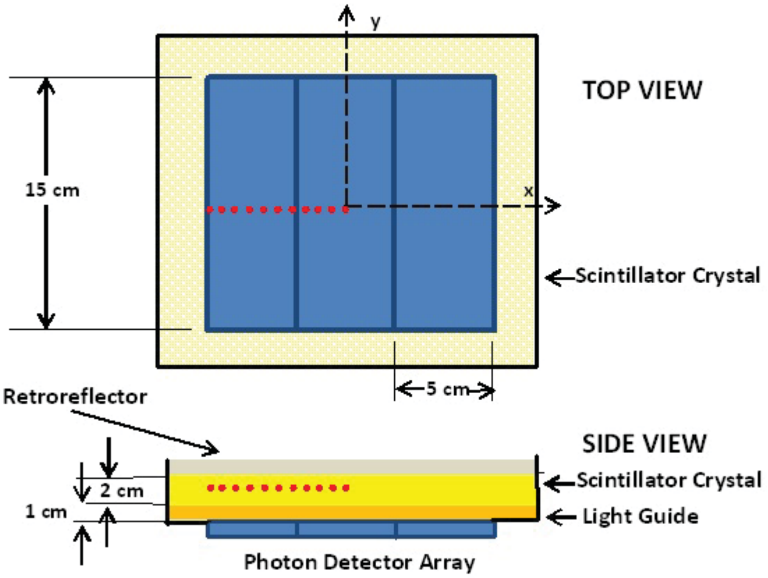

Figure 5.1: Geometry used in the 3×1 detector simulations. The 3 × 1 detector array has 3 detector-elements of 5 cm × 15 cm each to ensure high collection efficiency of optical photons. The red dots indicate the points of interaction in the crystal at which the CRB and variance of maximum likelihood estimator were estimated. The top view is shown without the retroreflector.

The MDRF calculated from (5.19) is plotted as a function of x in Fig. 5.2 and as a function of z in Fig. 5.3. The value of the MDRF and its derivative are very important for the calculation of the Fisher information matrix as well as for ML estimations. At ($x = 0$ cm, $y = 0$ cm, $z = 2$ cm), on average 76% of the total emitted scintillation light is collected. As the point of interaction moves towards the edge of the detector at ($x = 5$ cm, $y = 0$ cm, $z = 2$ cm), the total average light collection drops marginally to 67%. At the edge of the photodetector ($x = 7.5$ cm, $y = 0$ cm, $z = 2$ cm), the total light collection drops to 40%.

5.4.4 Geometry of 3 × 3 detector

To ensure that the results from our analysis do not suffer from artifacts due to the one-dimensional geometry of our 3 × 1 detector or from treating y as a known parameter, the effect of the Fano factor in a 3 × 3 detector is investigated. As seen

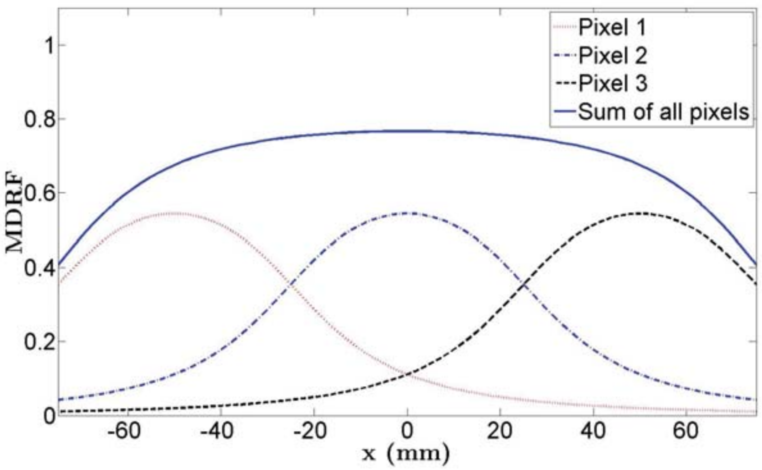

Figure 5.2: Mean detector response function (MDRF) of the 3×1 detector geometry is plotted as a function of x at $y = 0$ cm and $z = 2$ cm.

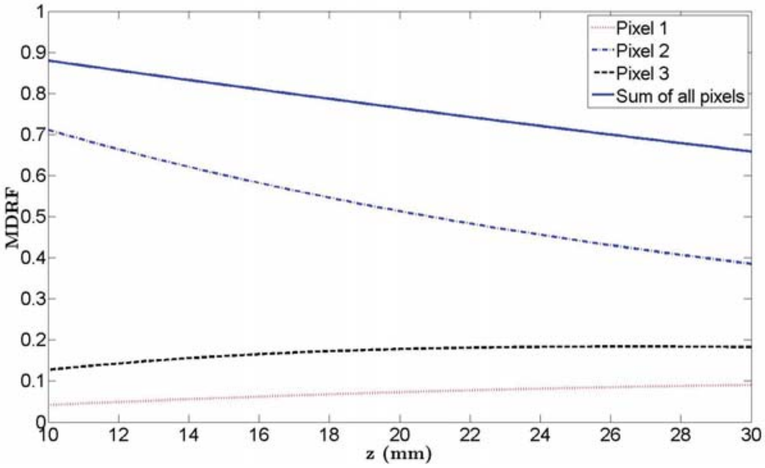

Figure 5.3: Mean detector response function (MDRF) of the 3×1 detector geometry is plotted as a function of z at $x = 1$ cm and $y = 0$ cm.

in Fig. 5.4, the geometry of the scintillator crystal and the retroreflector is identical to the geometry described in Sec. 5.4.3. The photodetector is divided into nine 5 cm × 5 cm detector-elements in a 3 × 3 configuration for a total area of 15 cm × 15 cm.

Computational limitations described in Sec. 5.4.2 prevent us from computing the CRB for a detector with more than three detector elements. We instead perform a Monte-Carlo simulation to estimate the variance of the ML estimator.

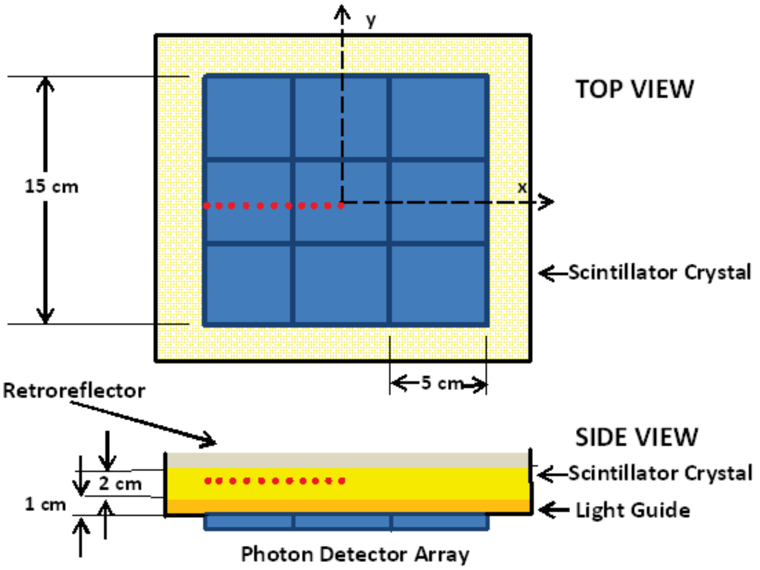

Figure 5.4: Detector geometry used in the 9 detector-element simulations. The 3 × 3 detector array has 9 detector-elements of dimensions 5 cm × 5 cm each. The total area of the optical detector is 15 cm × 15 cm. The red dots indicate the points of interaction in the crystal at which the variance of ML estimator was estimated. The top view is shown without the retroreflector.

5.4.5 Analytical solution

The expression for the score for x for the model described in Sec. 5.3 involves taking the logarithm of a sum of an expression which contains a number of factorials (see (5.20)). To calculate the elements of the Fisher information matrix, covariance of the score has to be averaged over all the values of $\vec{g}$ for the given value of $(x, y, z, \overline{N})$. As a result, a general analytical solution to (5.20) with an expression for the Fisher information as a function of Fano factor is extremely challenging if not impossible.

$$s_x(\vec{g}|x, y, z, F_N, \overline{N}) = \frac{\partial}{\partial x} \log \left(\sum_{N=1}^{\infty} Pr(\vec{g}|x, y, z, N) \times Pr(N|F_N, \overline{N}) \right). \tag{5.20}$$

However, we can analytically calculate the elements of the Fisher information matrix for two special cases: $F_N = 0$, and $F_N = 1$. Both calculations were done for the 3×1 geometry in Fig. 5.1. As we cannot estimate four independent parameters from three detector outputs, we treat y as a known parameter and calculate a 3×3 Fisher information matrix.

5.4.5.1 Multinomial case ($F_N = 0$)

When $F_N = 0$, there is no uncertainty in the value of N and $N = \bar{N}$ ($\bar{N}$ can only take integer values). Therefore, $Pr(\vec{g}|x, y, z, \overline{N})$ reduces to the multinomial distribution $Pr(\vec{g}|x, y, z, N)$ in (5.14). As $Pr(\vec{g}|x, y, z, \overline{N})$ varies with $\overline{N}$ in a discrete manner, its derivative with respect to $\overline{N}$ is either zero or undefined. Therefore, the score for $\overline{N}$ is either zero or not defined. This limits us to calculating a 2×2 Fisher information matrix with x and z as unknown parameters and y and $\overline{N}$ as known parameters.

Using the mean, variance and covariance of the multinomial distribution, the definition of α_j from (5.13) and some arithmetic, we derived the expressions for the elements of the Fisher information matrix for the $F_N = 0$, $I_{(xx)}^{(mn)}$, $I_{xz}^{(mn)}$ and $I_{zz}^{(mn)}$ case as

$$
\begin{aligned}
I_{xx}^{(mn)} = \frac{N}{(1-\alpha_1-\alpha_2-\alpha_3)} \times \Bigg\{ & \left(\frac{\partial \alpha_1}{\partial x}\right)^2 \left(\frac{1-\alpha_2-\alpha_3}{\alpha_1}\right) + \left(\frac{\partial \alpha_2}{\partial x}\right)^2 \left(\frac{1-\alpha_1-\alpha_3}{\alpha_2}\right) \\
& + \left(\frac{\partial \alpha_3}{\partial x}\right)^2 \left(\frac{1-\alpha_1-\alpha_2}{\alpha_3}\right) + 2\frac{\partial \alpha_1}{\partial x}\frac{\partial \alpha_2}{\partial x} + 2\frac{\partial \alpha_2}{\partial x}\frac{\partial \alpha_3}{\partial x} + 2\frac{\partial \alpha_1}{\partial x}\frac{\partial \alpha_3}{\partial x} \Bigg\},
\end{aligned}
\tag{5.21}
$$

$$
\begin{aligned}
I_{zz}^{(mn)} = \frac{N}{(1-\alpha_1-\alpha_2-\alpha_3)} \times \Bigg\{ & \left(\frac{\partial \alpha_1}{\partial z}\right)^2 \left(\frac{1-\alpha_2-\alpha_3}{\alpha_1}\right) + \left(\frac{\partial \alpha_2}{\partial z}\right)^2 \left(\frac{1-\alpha_1-\alpha_3}{\alpha_2}\right) \\
& + \left(\frac{\partial \alpha_3}{\partial z}\right)^2 \left(\frac{1-\alpha_1-\alpha_2}{\alpha_3}\right) + 2\frac{\partial \alpha_1}{\partial z}\frac{\partial \alpha_2}{\partial z} + 2\frac{\partial \alpha_2}{\partial z}\frac{\partial \alpha_3}{\partial z} + 2\frac{\partial \alpha_1}{\partial z}\frac{\partial \alpha_3}{\partial z} \Bigg\},
\end{aligned}
\tag{5.22}
$$

$$
\begin{aligned}
I_{xz}^{(mn)} = I_{zx}^{(mn)} = \frac{N}{(1-\alpha_1-\alpha_2-\alpha_3)} \times \Bigg\{ &\left(\frac{\partial\alpha_1}{\partial x}\frac{\partial\alpha_1}{\partial z}\right)\left(\frac{1-\alpha_2-\alpha_3}{\alpha_1}\right) \\
+\left(\frac{\partial\alpha_2}{\partial x}\frac{\partial\alpha_2}{\partial z}\right)\left(\frac{1-\alpha_1-\alpha_3}{\alpha_2}\right) &+ \left(\frac{\partial\alpha_3}{\partial x}\frac{\partial\alpha_3}{\partial z}\right)\left(\frac{1-\alpha_1-\alpha_2}{\alpha_3}\right) \\
+\frac{\partial\alpha_1}{\partial x}\frac{\partial\alpha_2}{\partial z} + \frac{\partial\alpha_1}{\partial z}\frac{\partial\alpha_2}{\partial x} + \frac{\partial\alpha_2}{\partial x}\frac{\partial\alpha_3}{\partial z} &+ \frac{\partial\alpha_2}{\partial z}\frac{\partial\alpha_3}{\partial x} + \frac{\partial\alpha_1}{\partial x}\frac{\partial\alpha_3}{\partial z} + \frac{\partial\alpha_1}{\partial z}\frac{\partial\alpha_3}{\partial x}\Bigg\}.
\end{aligned}
\tag{5.23}
$$

We use (5.21, 5.23, 5.22) to construct the Fisher information matrix for the 3 × 1 geometry in Sec. 5.4.3 and calculate the Cramée-Rao bound for the multinomial case ($F_N = 0$).

5.4.5.2 Poisson Case ($F_N = 1$)

Let us consider the Poisson case ($F_N = 1$) applicable for any geometry with three detector elements. Here, $Pr(N|\overline{N})$ is a Poisson distribution with mean $\overline{N}$

$$Pr(N|\overline{N}) = \frac{\overline{N}^N e^{-\overline{N}}}{N!}. \tag{5.24}$$

For the Poisson-distributed scintillation photons detected with three detectors elements, we treated $x, z, \overline{N}$ as unknown parameters and calculated a 3 × 3 Fisher information matrix. To compare the analytical results from the $F_N = 0$ and $F_N = 1$ cases, we also calculated a reduced CRB from the 2 × 2 section of the Fisher information matrix which yields the CRB for the x and z estimates.

Multinomial sampling with three outcomes of the Poisson-distributed scintillation light, results in the three Poisson-distributed detector outputs, with means $\alpha_1\overline{N}, \alpha_2\overline{N}$ and $\alpha_3\overline{N}$ (Barrett and Myers, 2004).

$$Pr(\vec{g}|x, y, z, \overline{N}) = \prod_{i=1}^{3} \frac{(\alpha_i\overline{N})^{g_i} e^{(\alpha_i\overline{N})}}{g_i!}. \tag{5.25}$$

Using the expressions for the mean, variance, covariance of the Poisson distribution, the definition of α_j in (5.13) and a little arithmetic, we derived the expression for the $I_{xx}^{(poiss)}, I_{zz}^{(poiss)}, I_{\overline{N}\,\overline{N}}^{(poiss)}\ I_{xz}^{(poiss)}, I_{x\overline{N}}^{(poiss)}$ and $I_{z\overline{N}}^{(poiss)}$ elements of the Fisher information matrix for $F_N = 1$ case as

$$I_{xx}^{(poiss)} = \overline{N}\left\{\frac{1}{\alpha_1}\left(\frac{\partial\alpha_1}{\partial x}\right)^2 + \frac{1}{\alpha_2}\left(\frac{\partial\alpha_2}{\partial x}\right)^2 + \frac{1}{\alpha_3}\left(\frac{\partial\alpha_3}{\partial x}\right)^2\right\}, \tag{5.26}$$

$$I_{zz}^{(poiss)} = \overline{N}\left\{\frac{1}{\alpha_1}\left(\frac{\partial\alpha_1}{\partial z}\right)^2 + \frac{1}{\alpha_2}\left(\frac{\partial\alpha_2}{\partial z}\right)^2 + \frac{1}{\alpha_3}\left(\frac{\partial\alpha_3}{\partial z}\right)^2\right\}, \tag{5.27}$$

$$I_{\overline{N}\,\overline{N}}^{(poiss)} = \frac{\alpha_1 + \alpha_2 + \alpha_3}{\overline{N}}, \tag{5.28}$$

$$\begin{aligned} I_{xz}^{(poiss)} = I_{zx}^{(poiss)} = \overline{N}\Bigg\{ & \frac{1}{\alpha_1}\left(\frac{\partial\alpha_1}{\partial x}\right)\left(\frac{\partial\alpha_1}{\partial z}\right) + \frac{1}{\alpha_2}\left(\frac{\partial\alpha_2}{\partial x}\right)\left(\frac{\partial\alpha_2}{\partial z}\right) \\ & + \frac{1}{\alpha_3}\left(\frac{\partial\alpha_3}{\partial x}\right)\left(\frac{\partial\alpha_3}{\partial z}\right)\Bigg\}, \end{aligned} \tag{5.29}$$

$$I_{x\overline{N}}^{(poiss)} = I_{\overline{N}x}^{(poiss)} = \frac{1}{\overline{N}}\left\{\left(\frac{\partial\alpha_1}{\partial x}\right) + \frac{1}{\alpha_2}\left(\frac{\partial\alpha_2}{\partial x}\right) + \frac{1}{\alpha_3}\left(\frac{\partial\alpha_3}{\partial x}\right)\right\}. \tag{5.30}$$

$$I_{z\overline{N}}^{(poiss)} = I_{\overline{N}z}^{(poiss)} = \frac{1}{\overline{N}}\left\{\left(\frac{\partial\alpha_1}{\partial z}\right) + \frac{1}{\alpha_2}\left(\frac{\partial\alpha_2}{\partial z}\right) + \frac{1}{\alpha_3}\left(\frac{\partial\alpha_3}{\partial z}\right)\right\}. \tag{5.31}$$

We use (5.26, 5.27, 5.28, 5.29, 5.30, 5.31) to construct the Fisher information matrix for the 3 × 1 geometry in Sec. 5.4.3 and calculate the Cramée-Rao bound for the Poisson case ($F_N = 1$).

5.4.6 Calculation of the Fisher information matrix and the Cramér-Rao bound

All Cramér-Rao calculations were performed for the 3×1 geometry in Fig. 5.1. The analytically calculated CRB values are denoted by CRB_{bA}, while the numerically computed CRB values are denoted by CRB_{bC}. Here, b indicates that a $b \times b$ Fisher information matrix was used to compute the CRB.

5.4.6.1 Analytical Solution for $F_N = 0$ and $F_N = 1$

The expressions for the elements of Fisher information matrix in Sec. 5.4.5 for the multinomial ($F_N = 0$) and Poisson ($F_N = 1$) cases along with the derivatives of the MDRF curves in Fig. 5.2 and 5.3 are used to calculate the elements of the Fisher information matrix for various points of interaction (x, y, z) and mean number of optical photons emitted ($\overline{N}$).

For the multinomial ($F_N = 0$) case, we are limited to calculating a 2×2 Fisher information matrix, while for the Poisson ($F_N = 1$) case we calculated a 3×3 Fisher information matrix. The Fisher information matrices were numerically inverted to get the CRBs.

5.4.6.2 Numerical computation of Cramér-Rao bound

The numerical computation of the Fisher information matrix for Fano factors other than zero, at a given position of interaction (x, y, z) and mean number of scintillation photons emitted ($\overline{N}$), requires us to calculate the score for the different parameters which are being estimated. The score for x was calculated numerically using the following expression

$$\begin{aligned} s_x(\vec{g}) &= \frac{\partial}{\partial x} \log(\Pr(\vec{g}|x, y, z, F_N, \overline{N})) \\ &\approx \frac{\log(\Pr(\vec{g}|x + \Delta x, y, z, F_N, \overline{N})) - \log(\Pr(\vec{g}|x, y, z, F_N, \overline{N}))}{\Delta x}. \end{aligned} \tag{5.32}$$

The convergence of the numerical derivative was verified by using different values of Δx. Scores for z and $\overline{N}$, denoted by s_z, and $s_{\overline{N}}$ respectively, have similar expressions. For the 3×1 geometry described in Sec. 5.4.3, y is treated as a known parameter. Thus, we estimated only three parameters, x, z, and $\overline{N}$, and the Fisher information matrix is a 3×3 matrix.

The elements of Fisher information matrix for each set of $(x, y, z, \overline{N})$ were calculated by a 5-dimensional summation, summing $\pm\, 5\sigma$ about the respective mean values in each of the 5 dimensions. The Fisher information matrix was inverted and the diagonal elements of the inverse of the Fisher information matrix were the CRB of the respective estimators.

5.4.7 Estimating the variance of the maximum likelihood estimator

5.4.7.1 Generating data

To estimate the variance of the ML estimator, we used the forward model described in Sec. 5.3 to generate the detector output data for a given position of interaction and energy deposited. For a given value of the Fano factor of scintillation photons (F_N) and mean number of optical photons emitted ($\overline{N}$), the probability distribution in (5.12) was sampled to get the number of optical photons generated (N) from the scintillation process. Using the geometries of the scintillator and the detector array, the probabilities (α_j) of an optical photon emitted at the point of interaction (x, y, z) creating a photoelectron at the j^{th} detector-element were computed. The numbers of optical photons detected at each detector element were generated using the multinomial statistics in (5.14) with the total number of photons, N, and the probability of detection at j^{th} detector-element, α_j. Thus detector output vectors were generated for a gamma-ray with energy E which interacts with a scintillator having Fano factor F_N, producing on an average $\overline{N}$ photons at the point of interaction (x, y, z).

5.4.7.2 Maximizing the log-likelihood

As the logarithm is a monotonically increasing function, the logarithm of the likelihood function achieves its maximum value at the same points as the likelihood function itself. Instead of maximizing the likelihood function, it is often more convenient to maximize the log-likelihood.

In this study, for a given data vector $\vec{g}$, the negative of log-likelihood function given in (5.16) was minimized using the Nelder-Mead method to estimate the position of interaction $(\hat{x}, \hat{y}, \hat{z})$ and the energy deposited ($\hat{\overline{N}}$) (Nelder and Mead, 1965). This is equivalent to maximizing the log-likelihood of the observed data to get the

ML estimates

$$(\hat{x}, \hat{y}, \hat{z}, \hat{\overline{N}})_{ML} = \arg \max_{(\mathrm{x,y,z,\overline{N}})} \left(\log(l(x, y, z, \overline{N}|\vec{g})) \right). \tag{5.33}$$

5.5 Results

All the CRB calculations and ML estimations for both the 3×1 geometry in Fig. 5.1 and the 3×3 geometry in Fig. 5.4 were computed for different values of the x coordinate of the point of interaction at $y = 0$ cm and $z = 2$ cm. The gamma-ray energy was arbitrarily assumed to be 70 KeV. We assumed a scintillator yield of 50,000 optical photons per MeV to get on average 3500 optical photons per gamma-ray interaction.

The CRB calculations were only performed for the 3×1 detector geometry in Fig. 5.1. The analytically calculated CRB from the 2×2 and 3×3 Fisher information matrices are denoted by CRB_{2A} and CRB_{3A} respectively. The numerically computed CRB from the 3×3 Fisher information matrix is denoted by CRB_{3C}.

5.5.1 Resolution and variance of the estimator

The spatial resolution is often defined as the full width at half maximum (FWHM) of the distribution of a position estimator. If the position estimates are assumed to be normally distributed, then the relationship between the variance of the position estimator and FWHM is given by FWHM $= 2.35\sigma$. Therefore, the spatial resolution of the x ML estimates denoted by δ_{Ml_x} is given by

$$\delta_{ML_x} = 2.35\hat{\sigma}_{ML_x}. \tag{5.34}$$

As the CRB is a lower bound on the variance of the unbiased estimator, SR_{CRB} is the lower bound on the spatial resolution of an unbiased estimator

$$\delta_{CRB_x} = 2.35\sqrt{(\mathrm{CRB})_x}. \tag{5.35}$$

A gamma-ray interaction in which all the energy from the gamma-ray is deposited in the crystal is a photopeak event. Thousands of these photopeak events are collected to make a histogram. Energy resolution is defined as the ratio of the FWHM and the mean of the photopeak. It is usually expressed as a percentage.

$$\delta_E = \frac{\text{FWHM of Photopeak}}{\text{mean of Photopeak}} 100 \tag{5.36}$$

If we assume that the energy estimates are normally distributed, then the FWHM of the photopeak is given by FWHM $= 2.35\sigma_E$. Using the relationship between E and $\overline{N}$, $E = Q\overline{N}$, we get $\sigma_E = Q\sigma_{\overline{N}}$. Thus, the energy resolution computed using the ML estimates, denoted by δ_{ML}, is given by

$$\delta_{ML_E} = \frac{2.35 Q \sigma_{\hat{\overline{N}}}}{Q\overline{N}} 100 = \frac{2.35 \sigma_{\hat{\overline{N}}}}{\overline{N}} 100. \tag{5.37}$$

Similarly, the lower bound on the energy resolution from an unbiased estimator denoted by δ_{CRB_E} is given by

$$\delta_{CRB_E} = \frac{2.35\sqrt{\text{CRB}_E}}{\overline{N}} 100 \tag{5.38}$$

5.5.2 Results for the 3 × 1 detector geometry

5.5.2.1 Analytical solution for Cramér-Rao bound for 3 × 1 geometry for $F_N = 0$ and $F_N = 1$

As we could analytically calculate only a 2×2 Fisher information matrix for $F_N = 0$, we compared the bounds on x and z resolution with the resolution bound from the corresponding reduced Fisher information matrix for the $F_N = 1$ case. The CRB computed with the reduced 2×2 Fisher information matrix gives us the bounds for the x and z resolution. The resolution bounds are applicable for the x and z estimators when the true values of y and $\overline{N}$ are known. We also analytically calculated CRB_{3A} for the $F_N = 1$ case by using the 3×3 Fisher information matrices. In Fig. 5.5, we plot the x resolution bounds calculated from 2×2 and 3×3 Fisher information matrices. We observe that for $F_N = 1$, CRB_{3A} values are higher than

CRB_{2A} values because in addition to x and z, $\overline{N}$ is also an unknown parameter. The uncertainty in the estimate of $\hat{\overline{N}}$ and the interaction between the estimators results in increased CRB_{3A} and resolution bounds of the x and z estimators.

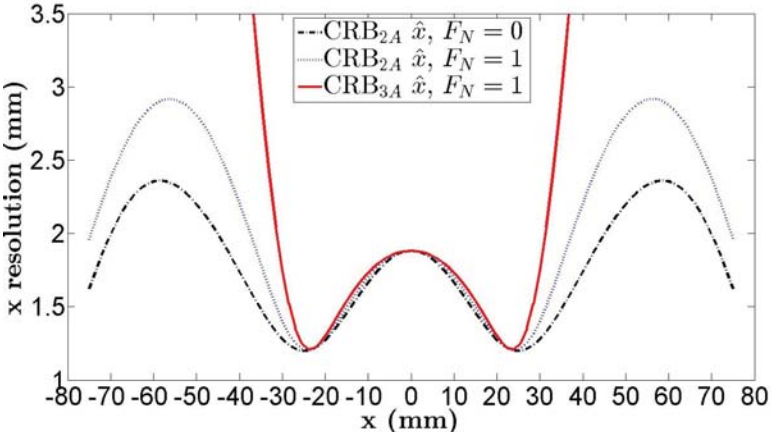

Figure 5.5: The x resolution bounds calculated from CRB_{2A} for the multinomial case ($\text{CRB}_{2A}\ \hat{x}$, $F_N = 0$), from CRB_{2A} for the Poisson case ($\text{CRB}_{2A}\ \hat{x}$, $F_N = 1$) and from CRB_{3A} for the Poisson case ($\text{CRB}_{3A}\ \hat{x}$, $F_N = 1$) are plotted as a function of x at $y = 0$ cm, $z = 2$ cm and $\overline{N} = 3500$. The CRB_{2A} bound was analytically calculated for the 3×1 detector geometry from a 2×2 Fisher information matrix which treated x and z as parameters to be estimated with y and $\overline{N}$ known. The CRB_{3A} bound was analytically calculated for the same 3×1 detector geometry from a 3×3 Fisher information matrix which treated x and z and $\overline{N}$ as parameters to be estimated and y as a known parameter.

The x resolution bounds calculated from the 2×2 Fisher information matrix in Fig. 5.5 indicates that if we only estimate x and z, and know the true values of y and $\overline{N}$, a scintillator with Fano factor of zero outperforms a scintillator with a Fano factor of one. The dip in all the x resolution bounds at $x \approx \pm 25mm$ corresponds to the boundary between two-detector elements. The resolution bounds for CRB_{2A} for $F_N = 0$, CRB_{2A} for $F_N = 1$ and CRB_{3A} for $F_N = 1$ are very close to each other at $x = 0$ and $x \approx \pm 25mm$. The x resolution bounds diverge substantially at higher values of x. Knowledge of the true value of $\overline{N}$ and lower total detector output (which could only have originated from an interaction near the edge of the detector), result in another dip in the x resolution bounds calculated using the 2×2 Fisher information matrix near the edge of the detector. The x resolution bound calculated from the 3×3 Fisher information matrix does not improve near the detector edge.

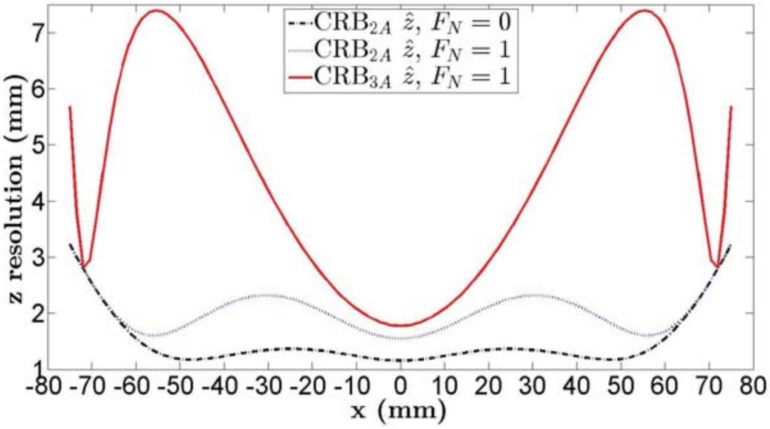

Figure 5.6: The z resolution bounds calculated from CRB$_{2A}$ for the multinomial case (CRB$_{2A}$ $\hat{x}$, $F_N = 0$), from CRB$_{2A}$ for the Poisson case (CRB$_{2A}$ $\hat{x}$, $F_N = 1$) and from CRB$_{3A}$ for the Poisson case (CRB$_{3A}$ $\hat{x}$, $F_N = 1$) are plotted as a function of x at $y = 0$ cm, $z = 2$ cm and $\overline{N} = 3500$. The CRB$_{2A}$ bound was analytically calculated for the 3×1 detector geometry from a 2×2 Fisher information matrix which treated x and z as parameters to be estimated with y and $\overline{N}$ known. The CRB$_{3A}$ bound was analytically calculated for the same 3×1 detector geometry from a 3×3 Fisher information matrix which treated x and z and $\overline{N}$ as parameters to be estimated and y as a known parameter.

The energy estimates and the z estimates are tightly coupled. This is because the number of detected optical photons varies strongly with the energy of the gamma-ray photon as well as with the depth of interaction. In comparison, the variation in the number of detected optical photons with the x or y position of interaction is not as significant. Hence in Fig. 5.6, CRB$_{2A}$, $\hat{z}$ bound for the low-noise multinomial model ($F_N = 0$) is substantially smaller than CRB$_{2A}$, $\hat{z}$ bound for the Poisson model ($F_N = 1$). When the interactions with the energy estimator are included to calculate the CRB$_{3A}$ for the Poisson model, the CRB$_{3A}$ increases significantly.

As the position of interaction moves closer to the edge, the z resolution bounds for $F_N = 0$ and $F_N = 1$ calculated from a 2×2 Fisher information matrix converge. This is because, near the edges, the lower light collection reduces the impact of Fano factor on the detector outputs (Eq. 5.17).

5.5.2.2 Numerical results of CRB for 3 × 1 geometry

The Fisher information matrix was numerically computed for the 3 × 1 detector-geometry described in Sec. 5.4.3 for Fano factors from 0.2 to 1.8 at 51 equally spaced values of x from 0 cm to 7.5 cm, at $y = 0$ cm, and $z = 2$ cm.

The bounds on the x, z and energy resolutions were numerically computed using a 3 × 3 Fisher information matrix for different Fano factors and plotted in Fig. 5.7. For comparison, the analytically calculated bounds on the x, z and energy resolutions using the 3 × 3 Fisher information matrix for the Poisson case (from equations 5.26 - 5.31) are also plotted in Fig. 5.7. The numerically computed and the analytically calculated resolution bounds for $F_N = 1$ case on x and z estimators are in agreement with each other. Despite the assumptions made in Sec. 5.4.1 to maximize the impact of Fano factor on detector outputs, CRB_{3A} and CRB_{3C} for the x as well as z estimators are observed to be independent of the Fano factor.

The estimators interact with each other through the off-diagonal elements of the Fisher information matrix. If we have zero, or very small off-diagonal elements, it implies that the estimators are independent of each other. A high value of the off-diagonal elements imply that the estimators interact strongly with each other. When the point of interaction is over the center of the detector ($x = 0$ cm, $y = 0$ cm, $z = 2$ cm), we observed that the x-z and x-$\overline{N}$ off-diagonal elements of the Fisher information matrix are very small. As the point of interaction is moved away from $x = 0$ cm, we observed that the off-diagonal elements increase by 4-5 orders of magnitude. This indicates that at the center, the x estimate is independent of z and $\overline{N}$ estimates but the same is not true when the point of interaction occurs off-center.

At the boundary between two detector elements, the relatively large MDRF slopes along x make the detector outputs relatively more sensitive to changes in x (see (5.26)). Therefore, the bound on the x resolution is the smallest over the boundary between two detector elements. As the point of interaction is moved

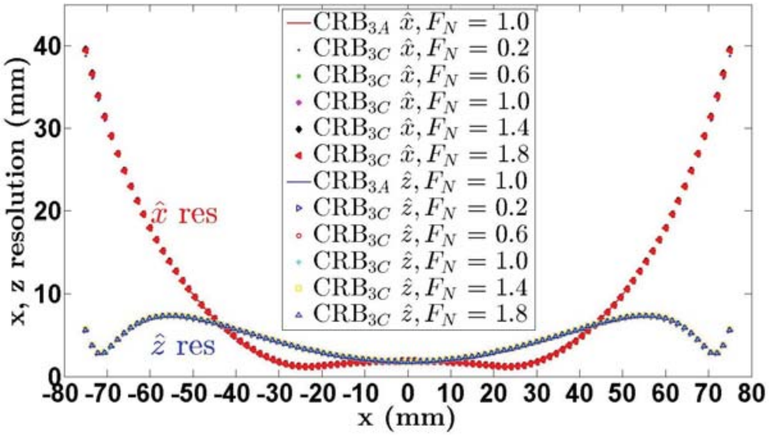

Figure 5.7: The numerically computed lower bounds on the x resolution ($\mathrm{CRB}_{3C}\ \hat{x}$) and the z resolution ($\mathrm{CRB}_{3C}\ \hat{z}$), computed from a 3×3 Fisher information matrix for different Fano factors and the analytically calculated lower bound on the x resolution ($\mathrm{CRB}_{3A}\ \hat{x}, F_N = 1$) and the z resolution ($\mathrm{CRB}_{3A}\ \hat{z}, F_N = 1$) calculated from a 3×3 Fisher information matrix are plotted as a function of x at $y = 0$ cm, $z = 2$ cm and $\overline{N} = 3500$. The CRB_{3A} and CRB_{3C} bounds were calculated for the 3×1 detector geometry and are applicable when x, z, and $\overline{N}$ are simultaneously estimated and y is a known parameter. For every value of x, the lower bounds of x and z resolutions for different Fano factors are almost equal, and therefore on top of each other.

further away from the center of the detector, a smaller fraction of the emitted optical photons are collected and the CRB_{3C} increases for both the x and z estimators.

The numerically computed energy resolution bounds for different Fano factors and the analytically calculated energy resolution bound for $F_N = 1$ are plotted as a function of x in Fig. 5.8. The large values of energy resolution near the edge of the detector in Fig. 5.8 make it difficult to distinguish between the different energy resolution bound curves close to the center. In Fig. 5.9, the energy resolution bounds are plotted for values of x from -50 cm to 50 cm. As the point of interaction moves away from the center of the detector, the geometrical efficiency of the optical detector reduces and as per (5.17), the effect of the Fano factor diminishes. Thus, as the point of interaction shifts away from the center, the spacing between the CRB_{3C} curves of the energy estimator for different Fano factors reduces. The numerically computed energy resolution bound for the $F_N = 1$ case is in agreement with the

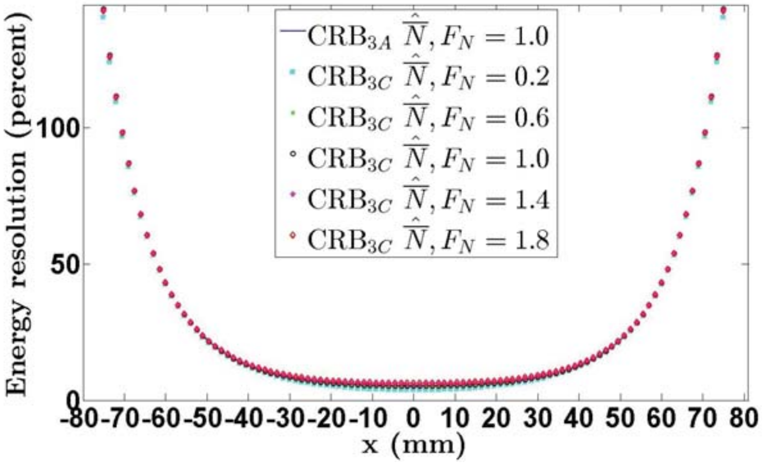

Figure 5.8: The numerically computed energy resolution bounds ($\mathrm{CRB}_{3C}\hat{\overline{N}}$) for different Fano factors and the analytically calculated energy resolution bound ($\mathrm{CRB}_{3A}\hat{\overline{N}}, F_N = 1$) for the Poisson case are plotted as a function of x at $y = 0$ cm, $z = 2$ cm and $\overline{N} = 3500$. The CRB_{3A} and CRB_{3C} bounds were calculated for the 3×1 detector geometry and are applicable when x, z, and $\overline{N}$ are simultaneously estimated and y is a known parameter. The energy resolution bound gets larger as the Fano factor increases. All the above energy bounds were calculated from a 3×3 Fisher information matrix.

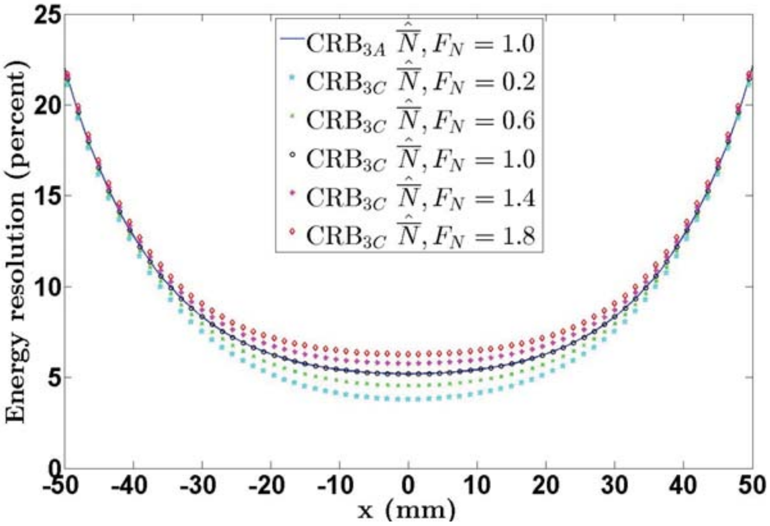

Figure 5.9: To show the details of the CRB curves for the position of interactions near the center of the detector, this figure truncates the Fig. 5.8 at $x = \pm 50$mm.

analytically calculated Poisson case.

5.5.2.3 Maximum likelihood estimator for the 3 × 1 detector geometry

Using the procedure described in Sec. 5.4.7.1 and the geometry in Fig. 5.1, five hundred gamma-ray photopeak events were simulated and detector outputs were generated for each point of interaction, energy deposited and scintillation Fano factor. To compare the variance of the ML estimator with the CRB_{3C}, we chose the same points of interaction, energy deposited, and Fano factors for which the CRB_{3C} was calculated in Sec. 5.5.2.2. The position of interaction (x, $y = 0$ cm, z) and energy deposited $\overline{N}$ were simultaneously estimated using an ML estimator. The mean and variance of the ML estimators were estimated for each value of x from the 500 simulated photopeak events.

The bias of the position estimate results in distortion of the image (see Barrett et al. (2010)). The mean of the ML estimates was used to estimate the bias of the ML estimators (see Fig. 5.10 and Fig. 5.11). The bias of the energy estimator was calculated in KeV using (5.9) from the bias in the estimate of the mean number of scintillation photons. The bias of the ML estimator increases significantly beyond $x = \pm 50$cm. We restrict the analysis of the ML estimator to ($-50\text{cm} \leq x \leq 50$ cm), the estimates of the biases of the x, z and E estimators are less than 2% of their true values. Using a larger number of gamma-ray interactions will yield better estimates of the resolution as well as the bias.

The estimates of the x and z resolutions of the ML x and z estimators are plotted in Fig. 5.12, and the estimate of the energy resolution is plotted in Fig. 5.13.

5.5.2.4 Comparison of Cramér-Rao bound and the variance of the maximum likelihood estimator

In this section, the CRB_{3C} and the variance of the ML estimator are compared. If the spatial and energy resolution bounds calculated from the CRB_{3C} and the estimates of spatial and energy resolutions from an unbiased ML estimator are very

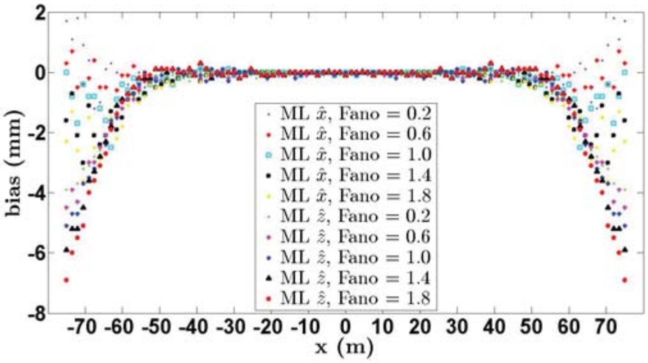

Figure 5.10: Estimates of the bias of the x estimator (ML $\hat{x}$) and the z estimator (ML $\hat{z}$) from the maximum likelihood estimator for Fano factors from 0.2 to 1.8 are plotted as a function of x at $y = 0$ cm, $z = 2$ cm and $\overline{N} = 3500$. The estimates of the bias of the x and z estimators for the 3×1 geometry were obtained by using the known value of $y = 0$ and simultaneously estimating x, z and $\overline{N}$.

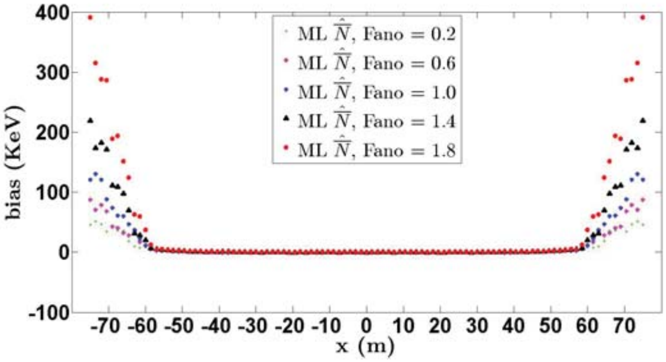

Figure 5.11: Estimates of the bias of the energy estimator (ML $\hat{\overline{N}}$) from the maximum likelihood estimator for Fano factors from 0.2 to 1.8 are plotted as a function of x at $y = 0$ cm, $z = 2$ cm and $\overline{N} = 3500$. The estimates of the bias of the energy estimators for the 3×1 geometry were obtained by using the known value of $y = 0$ and simultaneously estimating x, z and $\overline{N}$.

close, then it is consistent with the hypothesis that an efficient estimator exists and our ML estimator is efficient.

The spatial and energy resolution bounds calculated from the CRB_{3C} (Sec. 5.5.2.2) and the spatial and energy resolution estimates from the ML estimator (Sec. 5.5.2.3) were compared with each other. All the resolution bound curves for

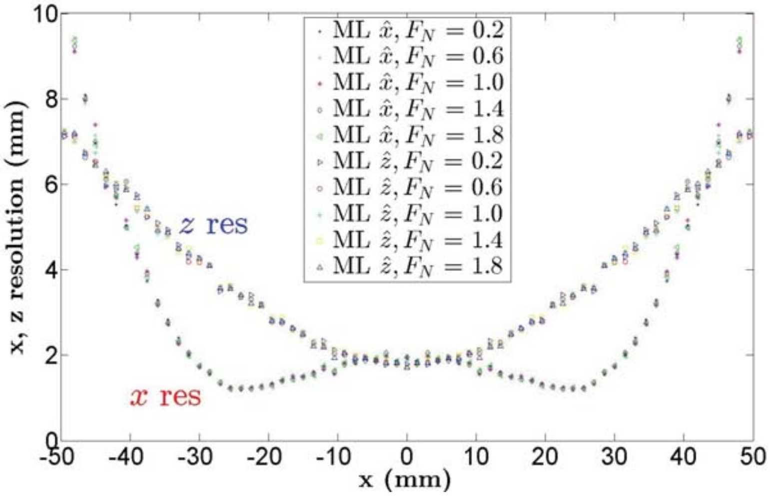

Figure 5.12: Estimates of the x resolution (ML $\hat{x}$) and z resolution (ML $\hat{z}$) from the maximum likelihood estimator for Fano factors from 0.2 to 1.8 are plotted as a function of x at $y = 0$ cm, $z = 2$ cm and $\overline{N} = 3500$. The estimates of the x and z resolutions for the 3×1 geometry were obtained by using the known value of $y = 0$ and simultaneously estimating x, z and $\overline{N}$.

CRB$_{3C}$ and resolution estimates from the ML estimators for all Fano factors considered were found to be in agreement with each other. However for clarity, only plots for the Fano factor of 0.2 are plotted in Fig. 5.14 and 5.15.

The estimate of the variances of the ML estimators becomes more accurate as more gamma-ray events are used for estimation task. The variance of the ML estimator was estimated from 5000 gamma-ray interactions and compared to the CRB. Computation time limited us to estimating the variance of the ML estimator at one point on the detector. The CRB$_{3C}$ and the variance of the ML estimator were compared at ($x = 0$ cm, $y = 0$ cm, $z = 2$ cm, $\overline{N} = 3500$).

We observe in Fig. 5.14 - 5.17 that the CRB$_{3C}$ calculations and the estimates of the variance of the ML estimators are in agreement with each other. These observations strongly support our hypothesis that an efficient estimator exists and our implementation of the ML estimator is efficient.

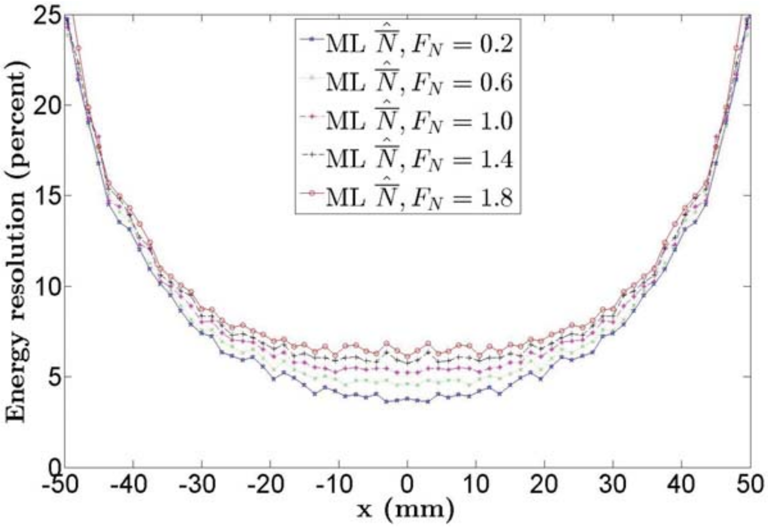

Figure 5.13: Estimates of the energy resolution from ML estimator (ML $\hat{\overline{N}}$) for Fano factors from 0.2 to 1.8 are plotted as a function of x at $y = 0$ cm, $z = 2$ cm and $\overline{N} = 3500$. The estimates of the energy resolution for the 3×1 geometry were obtained by using the known value of $y = 0$ and simultaneously estimating x, z and $\overline{N}$.

5.5.3 Results for the 3 × 3 detector geometry

Using the method described in Sec. 5.4.7.1 and the geometry in Fig. 5.4, five hundred gamma-ray photopeak events were simulated and detector outputs were generated for equally spaced values of x, $y = 0$ cm, $z = 2$ cm, $\overline{N} = 3500$, and different values of Fano factors. The position of interaction (x, y, z) and energy deposited $\overline{N}$ were simultaneously estimated using an ML estimator. The spatial and energy resolutions of the ML estimator were estimated from each of these 500 interactions. The estimates of the x resolution, and the z resolution of the ML estimator as a function of x are plotted in Fig. 5.18. The estimate of the y resolution as a function of x is plotted in Fig. 5.19 and the energy resolution of the ML estimator as a function of x is plotted in Fig. 5.20.

The ML estimates of the x, y and z resolutions are independent of the Fano factor (See Fig. 5.18 , 5.19). The estimates of the energy resolution for the 3 × 3 detector elements are plotted in Fig. 5.20.

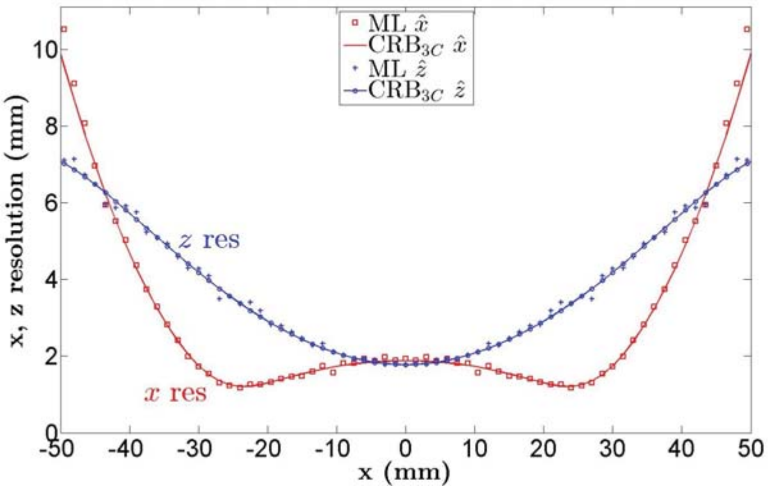

Figure 5.14: The numerically calculated x and z resolution bounds from a 3×3 Fisher information matrix (CRB$_{3C}$ $\hat{x}$, CRB$_{3C}$ $\hat{z}$ respectively) and the estimates of the x and z resolutions from the ML estimator (ML $\hat{x}$, ML $\hat{z}$ respectively) for the Fano factor of 0.2 are plotted as a function of x at y = 0 cm, z = 2 cm, and $\overline{N}$ = 3500. Both the CRB$_{3C}$ calculations and the ML estimation were performed for the 3×1 detector geometry and are applicable for the problem of estimating x, z and $\overline{N}$ with a known value of y. The x and z resolution bounds from the CRB$_{3C}$ calculations and the x and z resolution estimates from the ML estimators are in agreement with each other.

Another interesting observation from our simulation is that the variances of the ML estimators at the center of the detector x = 0 cm, y = 0 cm, z = 2 cm in the 3×3 geometry are marginally smaller than the variances of the ML estimator (and CRB) in the 3×1 geometry. However as we move away from the center of the detector, the variances of the ML estimator for the 3×3 detector geometry are much smaller than the variance of the ML estimator for the 3×1 detector. Thus the extra information from the 3×3 detector-elements not only enables us to estimate the y coordinate of the position of interaction, but also improves the estimates of x, z and $\overline{N}$. In the 3×1 geometry, we used a three-element data vector to estimate three unknown parameters. In the 3×3 case, we used a nine-element data vector to estimate four unknown parameters. The improved resolution in the 3×3 geometry is probably due to a better ratio of data elements to unknown parameters.

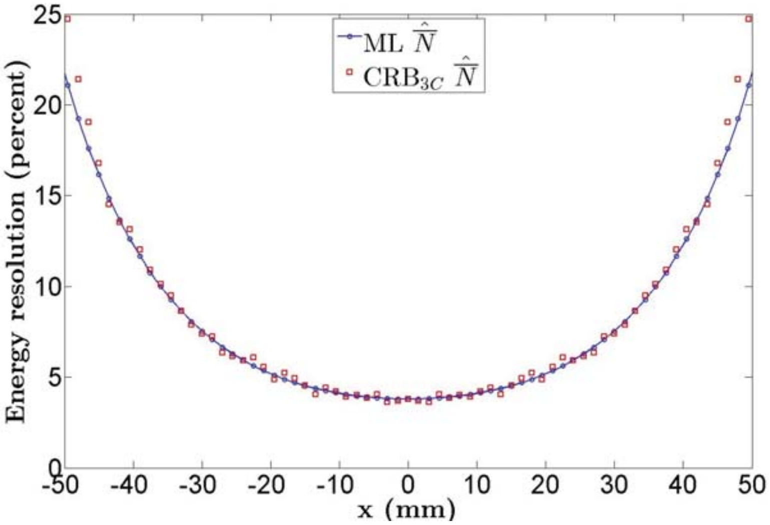

Figure 5.15: The energy resolution bound calculated from the CRB (CRB$_{3C}$ $\hat{\overline{N}}$) and the estimate of the energy resolution from the ML estimator (ML $\hat{\overline{N}}$) for Fano factor = 0.2 are plotted as a function of x at $y = 0$ cm, $z = 2$ cm, and $\overline{N} = 3500$. Both the CRB$_{3C}$ calculations and the ML estimation were performed for the 3×1 detector geometry and are applicable for the problem of estimating x, z and $\overline{N}$ with a known value of y. The bound on the energy estimator from the CRB calculations and the energy resolution estimate from the ML estimator are in agreement with each other.

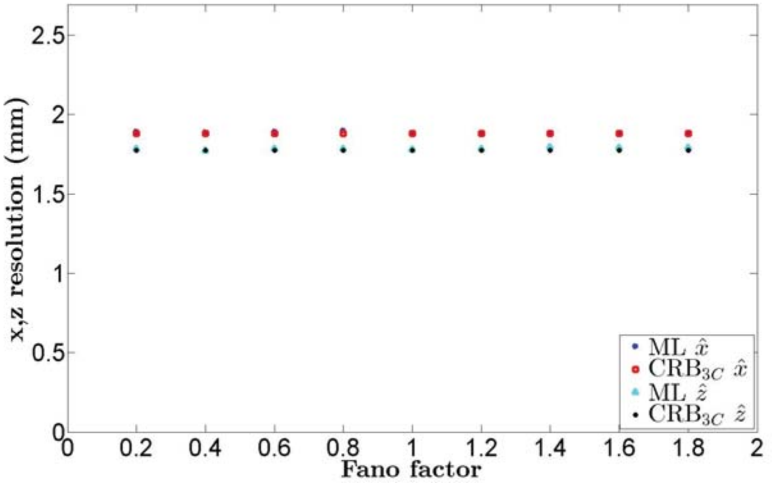

Figure 5.16: The bounds on the x and z resolutions (CRB_{3C} $\hat{x}$, CRB_{3C} $\hat{z}$ respectively) and the estimates of the x and z resolutions from the ML estimator (ML $\hat{x}$, ML $\hat{z}$ respectively) are plotted as a function of Fano factor at $x = 0$ cm, $y = 0$ cm, $z = 2$ cm, and $\overline{N} = 3500$. Both the CRB_{3C} calculations and the ML estimation were performed for the 3×1 detector geometry and are applicable for the problem of estimating x, z and $\overline{N}$ with a known value of y. The x and z resolution bounds from the CRB_{3C} calculations and the estimates of the x and z resolutions from ML estimator are in good agreement with each other and independent of the Fano factor.

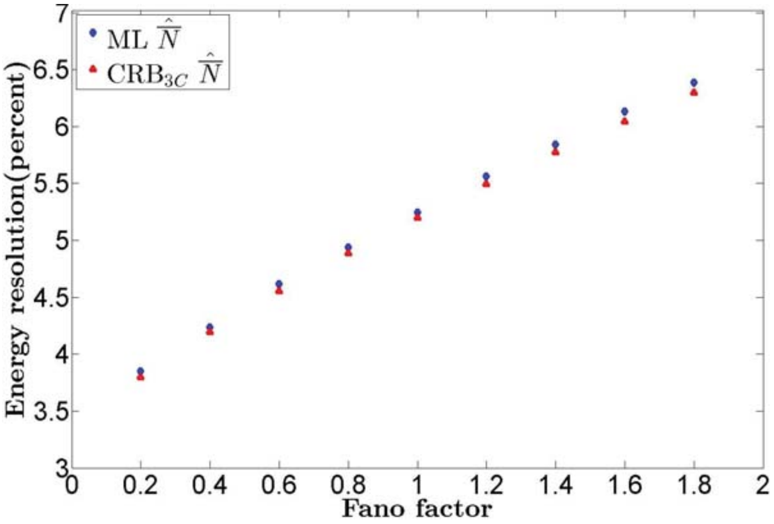

Figure 5.17: The bound on energy resolution (CRB$_{3C}$ $\hat{\overline{N}}$) and the estimate of energy resolution of the ML estimator (ML $\hat{\overline{N}}$) are plotted as a function of Fano factor at $x = 0$ cm, $y = 0$ cm, $z = 2$ cm, and $\overline{N} = 3500$. Both the CRB$_{3C}$ calculations and the ML estimation were performed for the 3×1 detector geometry and are applicable for the problem of estimating x, z and $\overline{N}$ with a known value of y. The bound of the energy resolution from the CRB calculations and the estimate of the energy resolution of the ML energy estimator are in good agreement with each other.

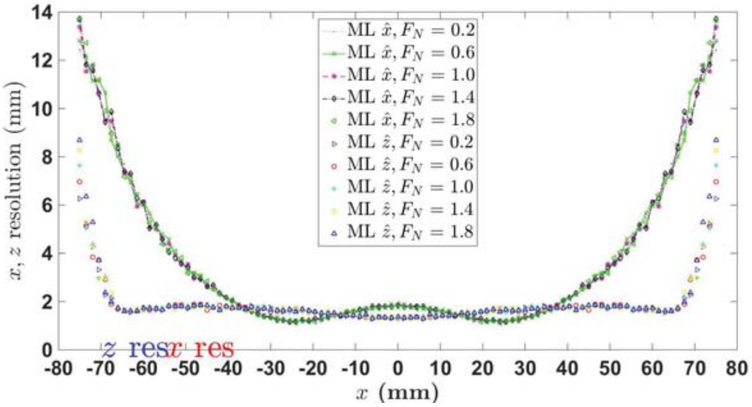

Figure 5.18: The estimates of the x and z resolutions (ML $\hat{x}$, ML $\hat{z}$ respectively) for the 3×3 geometry for different Fano factors are plotted as a function of x at $y = 0$ cm, $z = 2$ cm, and $\overline{N} = 3500$. The ML estimator simultaneously estimated x, y, z and $\overline{N}$. The estimates of the x, z resolutions of the ML estimator appear to be independent of the Fano factor.

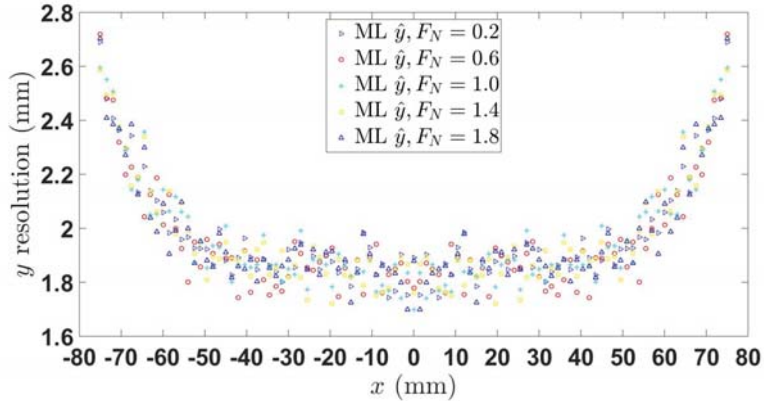

Figure 5.19: The estimates of the y resolution of the ML estimator for the 3×3 geometry for different Fano factors are plotted as a function of x at $y = 0$ cm, $z = 2$ cm, and $\overline{N} = 3500$. The ML estimator simultaneously estimated x, y, z and $\overline{N}$. The estimate of the y resolution of the ML estimator appears to be independent of the Fano factor as well as x.

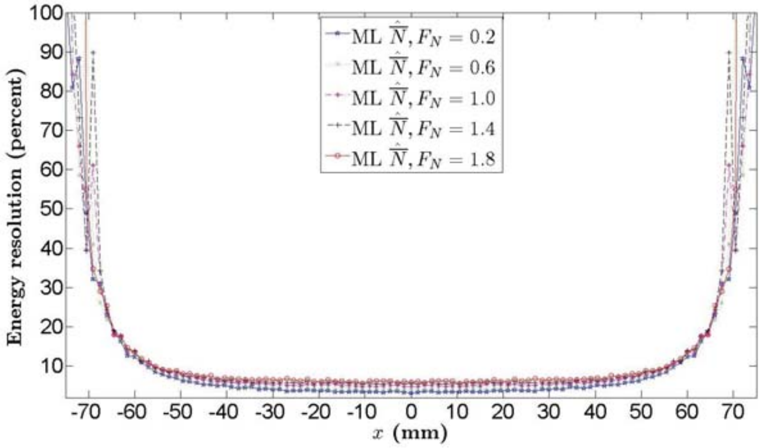

Figure 5.20: The energy resolutions of the ML estimator for the 3×3 geometry for different Fano factors are plotted as a function of x at $y = 0$ cm, $z = 2$ cm, and $\overline{N} = 3500$. The ML estimation were performed is applicable for the problem of estimating x, y, z and $\overline{N}$.

5.6 Analysis of results and conclusion

5.6.1 Spatial resolution and Fano factor

Analytical analysis of a reduced 2×2 Fisher information matrix for the 3×1 geometry, indicates that if the correct value of y and $\overline{N}$ is known, then the spatial resolution is better with $F_N = 0$ than with $F_N = 1$.

However, when x, z and $\overline{N}$ were estimated for the same geometry, the variance of the ML estimator was found to be in agreement with the CRB and independent of the Fano factor. The ML estimates of the spatial resolution from the 3×3 detector geometry (when we are simultaneously estimating the 3-D position of interaction and $\overline{N}$) also indicates that Fano factor does not have any impact on position estimation. Thus, we conclude that when estimating position and energy simultaneously, the Fano factor does not have any impact on the spatial resolution for the idealized detector configuration that we have considered.

The assumptions made in Sec. 5.4.1 namely, ideal detectors with 100% quantum efficiency of detectors, 100 % reflecting retro-reflectors, no gain or electronic noise in detectors, and large detector elements were made to maximize the impact of Fano factor on the detector outputs. Since the Fano factor has no impact on spatial resolution even in this idealized case, we can infer that for a practical detector with lower quantum and geometrical efficiency, the Fano factor will not impact the spatial resolution.

5.6.2 Energy resolution and Fano factor

Our results indicate that a smaller Fano factor results in a better energy resolution. Let us consider a practical detector with light detection efficiency η, gain G and gain noise $\beta = \frac{\sigma_G^2}{G^2}$. If we assume that the photopeak is normally distributed, then the relationship between the Fano factor and energy resolution is given by

$$\mathrm{ER} = 2.35\sqrt{\frac{1 + \beta + \eta(F_N - 1)}{\eta\overline{N}}}. \tag{5.39}$$

A better energy resolution results in a narrower photopeak making it easier to distinguish between different gamma-ray energies. The width of the photopeak can be calculated if we know the Fano factor and a few geometrical and detector parameters such as quantum efficiency and gain variance. The knowledge of the width of the photopeak can be used as a prior to constrain an estimation algorithm to further improve the energy resolution. However, exploiting the better energy resolution does not require prior knowledge of the underlying scintillator Fano factor. The photopeak width can be experimentally measured and used as a prior in the same way described above.

CHAPTER 6

Conclusion and Future Work

6.1 Conclusion

We have estimated the Fano factor of scintillation crystals using integral correlations and timing correlations. Within experimental error, the estimates of the Fano factor from both these methods were consistent with each other. Both the methods estimated the Fano factor of $LaBr_3$:Ce to a value close to 0.1 and the Fano factor of YAP:Ce was estimated to a value close to 1. The integral correlations concluded that SrI_2:Eu is sub-Poisson, while CsI:Na is super-Poisson.

The impact of Fano factor on spatial and energy resolution was also studied. A smaller Fano factor does give us better energy resolution, but does not improve spatial resolution.

6.2 Future Work

Scintillation crystals with Fano factors less than one have raised many questions and possibilities. We have investigated the impact of the Fano factor on spatial resolution in imaging detectors, but there are other interesting repercussions which are yet to be investigated

6.2.1 Effect of Fano factor on estimating the time of gamma-ray interaction

When a positron is emitted, it has a short lifetime, after which it annihilates with a high probability of emitting two gamma rays. If we neglect the position momentum, to conserve momentum the gamma-rays travel in the opposite directions. Positron Emission Tomography imaging technique uses two detectors to detect the two gamma rays and estimate the line along which they were emitted. If we estimate the difference in the time at which the gamma-rays interact at each detectors, we can localize the emission of the positron to a smaller segment of the estimated line. It has been shown that the signal-to-noise ratio in Positron Emission Tomography can be improved using the Time of Flight (ToF) measurements (Conti, 2006; Tomitani, 1981).

All simulation studies of ToF estimation with scintillators have modeled the scintillation light as Poisson (Derenzo et al., 2014; Choong, 2009; Seifert et al., 2012). We have shown that scintillation light can have Fano factors other than one. Scintillation light with a Fano factor less than one have anti-bunched photons. I expect scintillators with Fano factors less than one to perform better than scintillators with Fano factor greater than, or equal to one in the task of estimating the time of gamma-ray interaction.

6.2.2 Resolve the discrepancy between the correlation measurement of Fano factor and the energy resolution

Every energy-resolution measurement of all scintillators has always been above the energy resolution for a pure Poisson case. We measured the gain, gain variance, estimated the collection efficiencies and found the experimentally measured variance to be a lot larger than the variance predicted by our model.

We tried and rejected the following hypothesis to explain the discrepancy between bad energy resolutions and good Fano factors.

- Position of interaction: We used three different collimators. We found no noticeable difference in the variances and covariances of the two detector outputs looking at the same scintillation event when the of gamma-ray interaction was localized by a 1.3 mm diameter pinhole, or by a 0.25 mm diameter pinhole.

- The surface finish: We wanted to check if while polishing the crystals we created microscopic groves or features on its surface. Surface groves can increase variances by varying the optical properties at different parts of the crystal. To check this hypothesis, we used 1500, 5000 and 7000 grit emery papers to polish the hygroscopic crystals, but found no noticeable difference in the detector outputs.

- Sample size: We also measured samples of different thickness, but found the difference in the outputs to be much smaller than the difference in the model and experiment.
- Non-linear response: $LaBr_3$:Ce is a very fast crystal and it produces a very large signal for a very short amount of time. It can easily saturate the PMTs when they operate at the typical PMT voltage. Saturated detectors can yield smaller variances, so we also checked for linearity of our detector and scintillator by measuring the response to 662 KeV and 122 KeV gamma-ray energies and found the system to be linear at our operating voltage.
- Light loss: We made measurements with, and without Teflon reflectors on the sides. Although light collection and energy resolution improved with the Teflon reflectors, the small change in variance does not account for the excess variance in the experimental measurements.

However, we have not tried to test the following hypothesis

- Non-uniformity in the detector response at different parts of the detector can also cause a position dependent variance.

6.2.3 Measure Fano factor for other materials

We have only measured the Fano factor for a few materials. It will be very useful if Fano factor estimates were available for more materials.

6.2.4 Fano factor from individual pulses

If we use a low-energy gamma-ray source with a slow scintillator, we can resolve individual scintillation photons. The Fano factor can be estimated using the coefficient of variation

$$c = \frac{\sigma_{\Delta t}}{\overline{\Delta t}} = \frac{1}{\sqrt{k}}. \tag{6.1}$$

However, as we cannot distinguish between two gamma-rays who arrive within the resolution limit of our system, the measurement will be biased towards anti-bunching. However, the theory and results for a paralyzable detectors can be used to compensate for the detector resolution limit (Parzen, 1962). The anti-bunching, or bunching of photons can be estimated using the compensated coefficient of variation.

APPENDIX A

CRB from a Sub-matrix VS CRB from Complete Matrix

In this appendix, we prove that the diagonal elements of the inverse of a sub-matrix of the Fisher information matrix are less than or equal to the corresponding diagonal elements of the inverse of the complete Fisher information matrix.

Let us consider a Fisher information matrix M. By definition, M is square, symmetric and positive definite matrix. We write M as a block matrix consisting of four sub-matrices of dimensions given by their indices

$$M_{p\times p} = \begin{bmatrix} A_{m\times m} & B_{m\times n} \\ C_{n\times m} & D_{n\times n} \end{bmatrix}. \tag{A.1}$$

The inverse of the block matrix M is given by

$$M^{-1} = \begin{bmatrix} (A - BD^{-1}C)^{-1} & -A^{-1}B(D - CA^{-1}B)^{-1} \\ -D^{-1}C(A - BD^{-1}C) & (D - CA^{-1}B)^{-1} \end{bmatrix}. \tag{A.2}$$

As M is a symmetric matrix, sub-matrix C is a transpose of the sub-matrix B ($C = B^{\dagger}$). Thus we need to prove that for an arbitrary vector $\vec{V}$

$$\vec{V}^{\dagger}(A - BD^{-1}B^{\dagger})^{-1}\vec{V} \geq \vec{V}^{\dagger}A^{-1}\vec{V} \tag{A.3}$$

By definition, matrices A and D are also positive definite. As the inverse of a positive definite is also positive definite, D^{-1} is also positive definite. Therefore the inequality below is satisfied

$$\vec{V}^{\dagger}(A - BD^{-1}B^{\dagger})\vec{V} = \vec{V}^{\dagger}A\vec{V}. \tag{A.4}$$

For arbitrary, invertible matrices M_1, M_2, of the same dimensions if the inequality $\vec{V}^\dagger(M_1)\vec{V} \leq \vec{V}^\dagger M_2 \vec{V}$ is true then it can be shown that $\vec{V}^\dagger(M_1)^{-1}\vec{V} \geq \vec{V}^\dagger M_2^{-1}\vec{V}$ Horn and Johnson (1990). Applying this result to (A.4) gives us the inequality

$$\vec{V}^\dagger(A - BD^{-1}B^\dagger)^{-1}\vec{V} \geq \vec{V}^\dagger A^{-1}\vec{V} \tag{A.5}$$

proving that the CRB calculated from a sub-matrix of the Fisher information matrix is less than or equal to the CRB calculated from the complete Fisher information matrix.

APPENDIX B

Fano Factor and Anger Logic

Anger arithmetic is a widely used technique for estimating the position of interaction in gamma-ray detectors Anger (1958). Anger arithmetic is fast and easily implemented in hardware. But in cases with non-linear MDRF, the Anger arithmetic is biased, therefore Anger arithmetic is not an optimal method for position estimation. Any impact, or the absence of impact of the Fano factor on position estimation in Anger arithmetic will not be conclusive. This is because the results could be attributed to the nature of the estimator. However due to widespread use of Anger arithmetic, in this section we have studied the impact of Fano factor on Anger position estimation.

B.1 Geometry and model

Let us again consider the two detector-element Anger camera described in 5.6.1. For our analysis, we chose a geometry given in Fig. B.1. As the center of the two detector elements are at ± 3.75 cm from the center of the detector, the Anger estimate in mm is given by

$$\hat{X} = \frac{37.5 \times g_R + (-37.5) \times g_L}{g_R + g_L}. \tag{B.1}$$

The photon production and transport models described in Sec. 5.3 were used for the study. The x resolution of the Anger estimator was studied for Fano factors from 0.2 to 1.8 at 101 equally spaced values of x from -7.5 cm to 7.5 cm, at $y = 0$ cm, and $z = 2$ cm with $\overline{N} = 3500$.

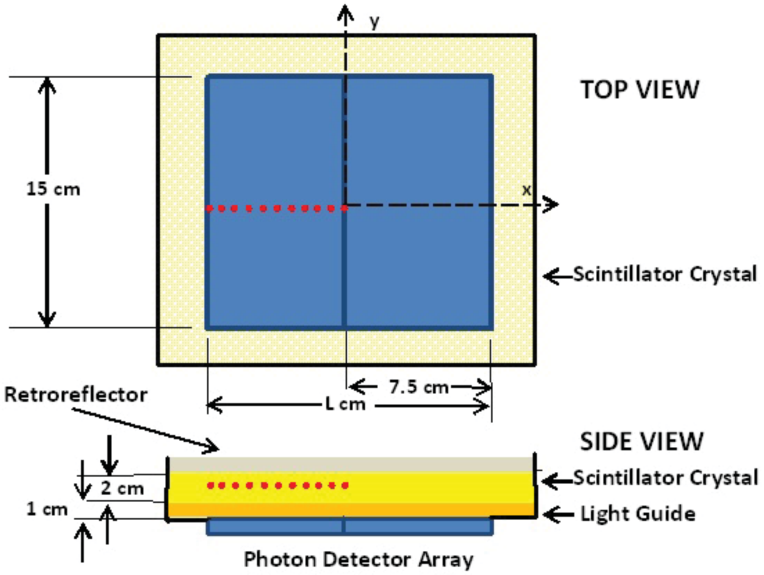

Figure B.1: Detector geometry used in 2 detector-element simulations. The 2 × 1 detector array, with each detector-element of dimensions 7.5 cm × 15 cm ensures high collection efficiency of optical photons. The red dots indicate the points of interaction in the crystal at which the Anger estimator was studied. The top view is shown without the retro reflector.

B.2 Analytical treatment of Anger arithmetic

Let us assume that $Pr(g_L|x,y,z,F_N,\overline{N})$ and $Pr(g_R|x,y,z,F_N,\overline{N})$ are normal distributions. This assumption is valid as long as the mean detector outputs are reasonable large. The means, the variances and covariance of the detector outputs g_L and g_R are given by Bora et al. (2011)

$$\overline{g_L} = \alpha_L \overline{N}, \tag{B.2a}$$

$$\overline{g_R} = \alpha_R \overline{N}, \tag{B.2b}$$

$$\sigma_L^2 = \overline{N}(\alpha_L + \alpha_L^2(F_N - 1)), \tag{B.2c}$$

$$\sigma_R^2 = \overline{N}(\alpha_R + \alpha_R^2(F_N - 1)), \tag{B.2d}$$

$$\rho_{(LR)} = \overline{N}\left(\frac{\alpha_R \alpha_L (F_N - 1)}{\sigma_L \sigma_R}\right). \tag{B.2e}$$

Here, α_L and α_R are the probability of a optical photon emitted at (x, y, z) being detected at the left and right detector respectively.

Let us define two new random variables, $P = 37.5(g_R - g_L)$ and $Q = g_R + g_L$. As P and Q are differences and sums of normally distributed random variables, they are also normally distributed with means, variances and covariance given by

$$\overline{P} = 37.5 \times (\overline{g_R - g_L}) = 37.5 \times (\overline{g_R} - \overline{g_L}), \tag{B.3a}$$

$$\overline{Q} = \overline{g_R + g_L} = \overline{g_R} + \overline{g_L}, \tag{B.3b}$$

$$\sigma_P = 37.5 \times \sigma_{gR-gL} = 37.5 \times \sqrt{\sigma_R^2 + \sigma_L^2 - 2\rho_{(LR)}\sigma_R\sigma_L}, \tag{B.3c}$$

$$\sigma_Q = \sigma_{gR+gL} = \sqrt{\sigma_R^2 + \sigma_L^2 + 2\rho_{(LR)}\sigma_R\sigma_L}, \tag{B.3d}$$

$$\rho_{(PQ)} = 37.5 \times \rho_{(gR-gL,gR+gL)} = 37.5 \times (\sigma_R^2 - \sigma_L^2). \tag{B.3e}$$

The Anger position estimate is a ratio of two normally distributed random variables. The probability density function of the ratio of two dependent, normally-distributed random variables with non-zero means is Cedilnik et al. (2004)

$$\begin{aligned} pr(\hat{X}) = & \frac{\sigma_P\sigma_Q\sqrt{1-\rho_{(PQ)}^2}}{\pi(\sigma_Q^2\hat{X}^2 - 2\rho_{(PQ)}\sigma_P\sigma_Q\hat{X} + \sigma_P^2)} \\ & \times \left[\exp(-\frac{1}{2}.\sup R^2) + \sqrt{2\pi}R.\Phi(R)\exp\big(-\frac{1}{2}(\sup R^2 - R^2)\big)\right]. \end{aligned} \tag{B.4}$$

Here, Φ is the error function and the expressions for $\sup R$ and R are

$$\begin{aligned} R(\hat{X}) = & \frac{1}{\sqrt{(1-\rho_{PQ}^2)}\sqrt{\hat{X}^2 - 2\rho_{(PQ)}\frac{\sigma_P}{\sigma_Q}\hat{X} + \left(\frac{\sigma_P}{\sigma_Q}\right)^2}} \\ & \times \left(\frac{\overline{P}}{\sigma_P} - \rho_{(PQ)}\frac{\overline{Q}}{\sigma_Q}\right)\hat{X} - \left(\rho_{(PQ)}\frac{\overline{P}}{\sigma_P} - \frac{\overline{Q}}{\sigma_Q}\right)\frac{\sigma_P}{\sigma_Q}, \end{aligned} \tag{B.5}$$

$$\sup R^2 = \frac{\left(\frac{\overline{P}}{\sigma_P}\right)^2 - 2\rho_{(PQ)}\frac{\overline{PQ}}{\sigma_P\sigma_Q} + \left(\frac{\overline{Q}}{\sigma_Q}\right)^2}{1-\rho_{(PQ)}^2}. \tag{B.6}$$

The variance of $pr(\hat{X})$ cannot be directly computed from (B.4). We numerically calculated the expected value of the mean and variance of the $\hat{X}$ estimator using the probability density function

$$\overline{\hat{X}} = \int\limits_{\hat{X}=-\inf}^{\inf} \hat{X} pr(\hat{X})\ d\hat{X}, \tag{B.7a}$$

$$\sigma^2_{\hat{X}} = \int\limits_{\hat{X}=-\inf}^{\inf} \hat{X}^2 pr(\hat{X})\ d\hat{X} - \overline{\hat{X}}^2. \tag{B.7b}$$

The bias of an estimator is given by

$$bias(x, \overline{\hat{X}}) = \overline{\hat{X}} - x. \tag{B.8}$$

As the Anger estimator is biased, the variance of the estimator is not a good figure of merit for a biased estimator. For example, an estimator which has a very high error, but is very consistent will have low variance. The root-mean-squared error (RMSE) is a better metric of estimator performance. The expression for the RMSE is

$$RMSE_{\hat{X}} = \sqrt{\frac{1}{n}\sum_{i=1}^{n}(\hat{X}_i - x)^2}. \tag{B.9}$$

Simplifying a little gives us an expression for RMSE as the sum of variance and bias of the estimator

$$RMSE_{\hat{X}} = \sqrt{\sigma^2_{\hat{X}} + (x - \overline{\hat{X}})^2} = \sqrt{\sigma^2_{\hat{X}} + bias(x, \overline{\hat{X}})^2}.. \tag{B.10}$$

B.3 Monte Carlo simulations of Anger arithmetic

The photon production and transport models described in Sec. 5.3 were used to generate ten thousand detector outputs (g_R, g_L) for Fano factors from 0.2 to 1.8 at 101 equally spaced values of x from -7.5 cm to 7.5 cm, at $y = 0$ cm and $z = 2$ cm with $\overline{N} = 3500$. For every point of interaction, the mean, variance, bias and mean square error of the x Anger estimator for different Fano factors were computed to evaluate the impact of Fano factor on our Anger camera.

B.4 Results

The expectation values of the x resolution of the Anger x estimator for the position of interactions, x between -7.5 cm and 7.5 cm, $y = 0$, $z = 2$ cm and mean number of optical photons, $\overline{N} = 3500$ for Fano factors from 0.2 to 1.8 are plotted in Fig. B.2. The bias of the Anger estimator as function of x is plotted in Fig. B.3. The bias of the Anger estimator does not appear to depend on the Fano factor of optical photons. The bias of the Anger estimator is many orders of magnitude larger than its variance. Hence, the RMSE is dominated by the bias of the Anger estimator. The bias goes to zero in the vicinity of $x = \pm 26$ mm and results in a dip in the RMSE curve.

To validate the analytical results, for each Fano factor, 10,000 detector outputs were generated and Anger x estimates were calculated for the same position of interactions and energy deposited as above. The sample mean and variance of these 10,000 estimates were used to calculate the x resolution, bias and RMSE. The results of the analytical calculations and the Monte Carlo simulations of the Anger arithmetic for the 2×1 geometry are in agreement with each other.

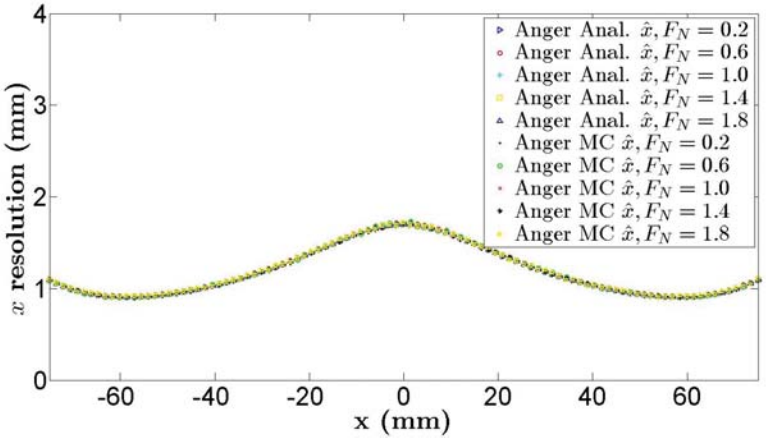

Figure B.2: The x resolutions of the Anger $\hat{x}$ estimators for various Fano factors calculated analytically (Anger Anal. $\hat{x}$)and estimated from the Monte Carlo simulations (Anger MC $\hat{x}$) are plotted as a function of x at $y = 0$ cm, $z = 2$ cm and $\overline{N}$ = 3500. For all the values of x, the Anger x resolutions for the different values of Fano factor appear to be very close to each other.

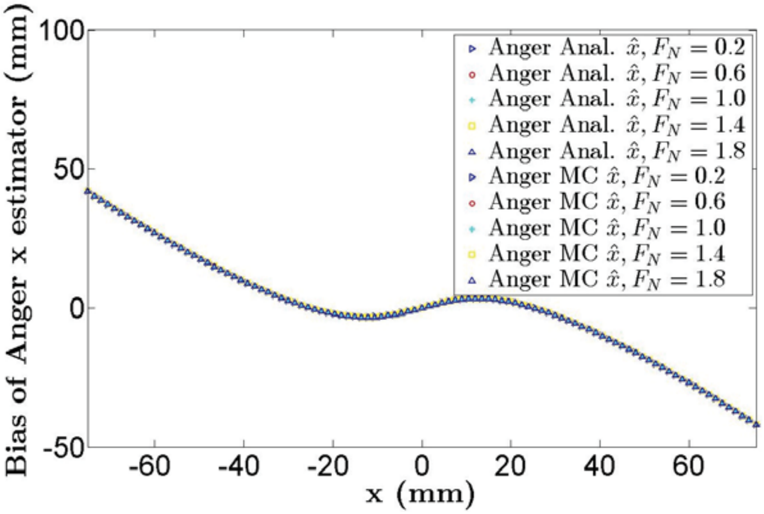

Figure B.3: The biases of the x Anger estimator from the analytical calculation (Anger Anal. $\hat{x}$)and estimated from the Monte Carlo simulations (Anger MC $\hat{x}$) for various Fano factors are plotted as a function of x at $y = 0$ cm, $z = 2$ cm and $\overline{N} =$ 3500. For all the values of x, the bias of the Anger estimates for the different values of Fano factor appear to be very close to each other.

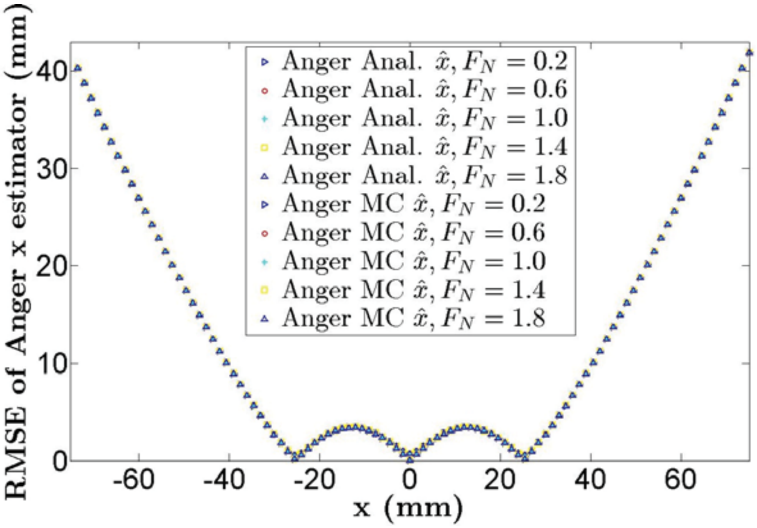

Figure B.4: The RMSE of the x Anger estimator from the analytical calculation (Anger Anal. $\hat{x}$)and estimated from the Monte Carlo simulations (Anger MC $\hat{x}$) for various Fano factors are plotted as a function of x at $y = 0$ cm, $z = 2$ cm and $\overline{N}$ = 3500. For all the values of x, the RMSE of the Anger estimates for the different values of Fano factor appear to be very close to each other.

REFERENCES

Aarsvold, J. N., R. A. Mintzer, K. L. Matthews, N. J. Yasillo, C. E. Ordonez, and C. T. Chen (1995). Implementations of Maximum-Likelihood Position Estimation in a Four-PMT Scintillation Detector. In *IEEE Nuclear Science Symposium and Medical Imaging Conference Record*, volume 3, p. 1811.

Alekhin, M. S., J. T. M. de Haas, I. V. Khodyuk, K. W. Krmer, P. R. Menge, V. Ouspenski, and P. Dorenbos (2013). Improvement of γ-ray energy resolution of $LaBr_3$:Ce^{3+} scintillation detectors by Sr^{2+} and Ca^{2+} co-doping. *Applied Physics Letters*, **102**(161915).

Anger, H. O. (1958). Scintillation Camera. *Review Of Scientific Intruments*, **29**, pp. 27–33.

Barrett, H. H., W. C. J. Hunter, B. W. Miller, S. K. Moore, Y. Chen, and L. R. Furenlid (2010). Maximum-Likelihood Methods for Processing Signals From Gamma-Ray Detectors. *IEEE Transactions on Nuclear Science*, **56**.

Barrett, H. H. and K. J. Myers (2004). *Foundations of Image Science*. John Wiley.

Barrett, H. H. and W. Swindell (1981). *Radiological Imaging*. Academic Press.

Berger, M., J. Hubbell, S. Seltzer, J. Chang, J. Coursey, R. Sukumar, D. Zucker, and K. B. UcerOlsen (2014). XCOM: Photon Cross Section Database (version 1.5). Online.

Bora, V., H. Barrett, and A. J. amd E. Clarkson (2015). Impact of Fano factor on position and energy estimation in Scintillation detectors. *IEEE Transactions on Nuclear Science*, **62**, pp. 42–56.

Bora, V., H. H. Barrett, K. S. Shah, and J. Glodo (2011). Estimation of Fano factors in Inorganic Scintillators. In *Nuclear Science Symposium and Medical Imaging Conference Record*, pp. 987,993. IEEE.

Born, M. and E. Wolf (1999). *Principles of Optics: Electromagnetic Theory of Propagation, Interference and Diffraction of Light*. Cambridge University Press, 7th edition.

Bousselham, A., H. H. Barrett, V. Bora, and K. Shah (2010). Photoelectron anticorrelations and sub-Poisson statistics in scintillation detectors. *Nuclear Instruments & Methods in Physics Research, Section A*, **620**, pp. 359–362.

Burgess, R. E. (1959). Homophase and heterophase fluctuations in semiconducting crystals. *Discuss. Faraday Soc.*, **28**, pp. 151–158.

Cedilnik, A., K. Kosmelj, and A. Blejec (2004). The Distribution of the Ratio of Jointly Normal Variables. *Metodoloki zvezki*, **1**, pp. 99–108.

Chen, Y. C., L. R. Furenlid, D. W. Wilson, and H. H. Barrett (2005). *Calibration of Scintillation Cameras and Pinhole SPECT Imaging Systems*, chapter 12, pp. 195–201. Springer.

Choong, W. S. (2009). The timing resolution of scintillation-detector systems: Monte Carlo analysis. *Physics in Medicine and Biology*, **54**(21), pp. 6495–6513.

Clarkson, E., D. W. Wilson, and H. H. Barrett (1999). Synthetic collimator for 2D and 3D imaging. *Proceeding of SPIE Medical Imaging*, **3659**, pp. 107–117.

Clinthorne, N. H., W. L. Rogers, L. Shao, and K. F. Koral (1987). A Hybrid Maximum Likelihood Position Computer for Scintillation Cameras. *IEEE Transactions on Nuclear Science*, **34**, pp. 97–101.

Conti, M. (2006). Effect of randoms on signal-to-noise ratio in TOF PET. *IEEE Transactions on Nuclear Science*, **53**, pp. 1188–93.

Cramer, H. (1946). *Mathematical Methods of Statistics*. Princeton University Press.

Derenzo, S., W. Choong, and W. Moses (2014). Fundamental limits of scintillation detector timing precision. *Physics in Medicine and Biology*, **59**(13), pp. 3261–86.

Derenzo, S. E. and M. J. Weber (1999). Prospects for First-Principle Calculations of Scintillator Properties. *Nuclear Instruments & Methods in Physics Research, Section A*, **442**, pp. 111–118.

Devanathan, R., L. R. Corrales, F. Gao, and W. J. Weber (2006). Signal variance in gamma-ray detectorsA review. *Nuclear Instruments & Methods in Physics Research, Section A*, **565**, pp. 637–649.

Falk, M., J. Husler, and R.-D. Reiss (2010). *Laws of Small Numbers: Extremes and Rare Events*. Birkhuser, 3 edition.

Fano, U. (1947). Ionization Yield of Radiations. II. The Fluctuations of the Number of Ions. *Physical Review Letters*, **72**, pp. 26–29.

Fiorini, C., A. Gola, M. Zanchi, A. Longoni, P. Lechner, H. Soltau, and L. Struder (2005). Gamma-ray spectroscopy with $LaBr_3$:Ce scintillator readout by a silicon drift detector. In *Nuclear Science Symposium and Medical Imaging Conference Record*, volume 1, pp. 230–234.

Gray, R. M. and A. Macovski (1974). Maximum a Posteriori Estimation of Position in Scintillation Cameras. *IEEE Transactions on Nuclear Science*, **23**, pp. 849–852.

Hesterman, J. Y., L. Caucci, M. A. Kupinski, H. H. Barrett, and L. R. Furenlid (2010). Maximum-Likelihood Estimation With a Contracting-Grid Search Algorithm. *IEEE Transactions on Nuclear Science*, **57**, pp. 1077–1084.

Horn, R. A. and C. R. Johnson (1990). *Matrix Analysis.* Cambridge University Press.

Kapusta, M., M. Balcerzyk, M. Moszynski, and J. Pawelke (1999). A high-energy resolution observed from a YAP: Ce scintillator. *Nuclear Instruments & Methods in Physics Research, Section A*, **421**, pp. 610–613.

Kerisit, S., Z. Wang, R. Williams, J. Grim, and F. Gao (2014). Kinetic Monte Carlo Simulations of Scintillation Processes in NaI(Tl). *IEEE Transactions on Nuclear Science*, **61**, pp. 860–869.

Knoll, G. F. (2010). *Radiation Detection and Measurement.* John Wiley.

Korevaar, M. A., M. C. Goorden, and F. J. Beekman (2013). Cramer-Rao lower bound optimization of an EM-CCD-based scintillation gamma camera. *Physics in Medicine and Biology*, **58**.

Kupinski, M. A. and H. H. Barrett (2005). *Small-Animal SPECT Imaging.* Springer Science+Business Media.

Li, Q., J. Q. Grim, R. Williams, G. Bizarri, and W. Moses (2011). The role of hole mobility in scintillator proportionality. *Nuclear Instruments & Methods in Physics Research, Section A*, **652**(1), pp. 288–291.

Li, Q., R. Williams, and D. Aberg (2013). First principles calculations and experiment predictions for iodine vacancy centers in SrI_2. *Physica status Solidi B*, **250**, pp. 233–243.

Li, X., W. C. J. Hunter, T. K. Lewellen, and R. S. Miyaoka (2012). Use of Cramer-Rao Lower Bound for Performance Evaluation of Different Monolithic Crystal PET Detector Designs. *IEEE Transactions on Nuclear Science*, **59**, pp. 3–12.

Milster, T. D., J. N. Aarsvold, H. H. Barrett, A. L. Landesman, L. S. Mar, D. D. Patton, T. J. Roney, R. K. Rowe, and R. H. Seacat III (1990). A Full-Field Modular Gamma Camera. *Journal of Nuclear Medicine*, **31**, pp. 632–639.

Milster, T. D., L. A. Selberg, H. Barrett, A. Landesman, and R. Seacat (1985). Digital Position Estimation for the Modular Scintillation Camera. *IEEE Transactions on Nuclear Science*, **32**, pp. 748–752.

Milster, T. D., L. A. Selberg, H. H. Barrett, R. L. Easton, G. R. Rossi, J. Arendt, and R. G. Simpson (1984). A Modular Scintillation Camera for Use in Nuclear Medicine. *IEEE Transactions on Nuclear Science*, **31**, pp. 578–580.

Moore, S. K. (2011). *ModPET: Novel Applications of Scintillation Cameras to Preclinical PET*. Ph.D. thesis, University of Arizona.

Moses, W. W. (2002). Current trends in scintillator detectors and materials. *Nuclear Instruments & Methods in Physics Research, Section A*, **A 487**, pp. 123–128.

Moses, W. W., G. A. Bizarri, R. T. Williams, S. A. Payne, A. N. Vasilev, J. Singh, J. Grim, and W. S. Choong (2012). The Origins of Scintillator Non-Proportionality. *IEEE Transactions on Nuclear Science*, **59**, pp. 2038–2044.

Nelder, J. A. and R. Mead (1965). A simplex method for function minimization. *The Computer Journal*, **7.4**, pp. 308–313.

Parzen, E. (1962). *Stochastic Processes*. Holden-Day.

Payne, S., N. Cherepy, G. Hull, J. Valentine, W. Moses, and W.-S. Choong (2009). Non-Proportionality of Scintillator Detectors: Theory and Experiment. *IEEE Transactions on Nuclear Science*, **56**.

Payne, S. A., W. W.Moses, S. Sheets, L. Ahle, N. Cherepy, B. Sturm, S. Dazeley, G. Bizarri, and W.-S. Choong (2011). Nonproportionality of Scintillator Detectors: Theory and Experiment. II. *IEEE Transactions on Nuclear Science*, **58**, pp. 3392 – 3402.

Rao, C. R. (1945). Information and the accuracy attainable in the estimation of statistical parameters. *Bull. Calcutta Math. Soc.*, **37**, pp. 81–91.

Rodnyi, P. A. (1997). *Physical Processes in Inorganic Scintillators*. The CRC press.

Rowe, R. K., J. N. Aarsvold, H. H. Barrett, J. C. Chen, W. P. Klein, B. A. Moore, I. W. Pang, D. D. Patton, and T. A. White (1993). A stationary hemispherical SPECT imager for three-dimensional brain imaging. *Journal of Nuclear Medicine*, **34**, pp. 474–480.

Sakai, E. (1987). Recent Measurements on Scintillator-Photodetector Systems. *IEEE Transactions on Nuclear Science*, **NS-34, No. 1**, pp. 418–422.

Salcin, E., H. B. Barber, and L. R. Furenlid (2011). Design considerations for the next-generation MAPMT-based monolithic scintillation camera. In Barber, H. B., H. Roehrig, and D. J. Wagenaar (eds.) *Proceedings of SPIE*, volume 8143. SPIE.

Saleh, B. E. A. (1977). *Photoelectron Statistics: With Applications to Spectroscopy and Optical Communications.* Springer-Verlag.

Seifert, S., H. T. van Dam, and D. R. Schaart (2012). The lower bound on the timing resolution of scintillation detectors. *Physics in Medicine and Biology*, **57**, pp. 1797–1814.

Syntfeld-Kazuch, A., P. Sibczynski, M. Moszynski, A. V. Gektin, M. Grodzicka, J. Iwanowska, M. Szawlowski, T. Szczesniak, and L. Swiderski. (2009). Performance of CsI (Na) scintillators in Gamma-Ray spectrometry. In *Nuclear Science Symposium and Medical Imaging Conference Record*, pp. 1474–1479. IEEE.

Szablowski, P. J. (2001). Discrete Normal distribution and its relationship with Jacobi Theta functions. *Statistics & Probability Letters*, **52**, pp. 289–299.

Taylor, H. M. and S. Karlin (1998). *An Introduction to Stochastic Modeling.* Academic Press.

Teich, M. C., B. E. A. Saleh, I. C. Khoo, and G. P. Agrawal (1988). *Progress in Optics, Vol. 26.* North Holland.

Tickner, J. and G. Roach (2007). PHOTON An optical Monte Carlo code for simulating scintillation detector responses. *Nuclear Instruments & Methods in Physics Research, Section B*, **263**, pp. 149–155.

Tomitani, T. (1981). Image reconstruction and noise evaluation in photon time-of-flight assisted positron emission tomography. *IEEE Transactions on Nuclear Science*, **28**, p. 458289.

van der Laan, D. J., M. C. Maas, D. R. Schaart, P. Bruyndonckx, S. Lonard, and C. W. E. van Eijk (2006). Using Cramer-Rao Theory Combined With Monte Carlo Simulations for the Optimization of Monolithic Scintillator PET Detectors. *IEEE Transactions on Nuclear Science*, **53**, pp. 1063–1070.

van Loef, E. V., C. M. Wilson, N. J. Cherepy, G. Hull, S. A. Payne, W. Choong, W. W. Moses, and K. Shah (June 2009). Crystal Growth and Scintillation Properties of Strontium Iodide Scintillator. *IEEE Transactions on Nuclear Science*, **56**, pp. 869–872.

Williams, R., J. Q. Grim, Q. Li, K. B. Ucer, and W. Moses (2011). Excitation density, diffusion-drift, and proportionality in scintillators. *Physica Status Solidi B*, **248**, pp. 426–438.